A Quartz Cherenkov Detector for Polarimetry at the ILC

Dissertation

zur Erlangung des Doktorgrades
des Fachbereichs Physik
der Universität Hamburg

vorgelegt von Annika Vauth
aus Preetz

Hamburg 2014

Gutachter der Dissertation:	Dr. Jenny List
	Prof. Dr. Peter Schleper
Gutachter der Disputation:	Dr. Jenny List
	Prof. Dr. Erika Garutti
Datum der Disputation:	22.08.2014
Vorsitzender des Prüfungsausschusses:	Dr. Georg Steinbrück
Vorsitzende des Promotionsausschusses:	Prof. Dr. Daniela Pfannkuche
Leiter des Fachbereichs Physik	Prof. Dr. Peter Hauschildt
Dekan der Fakultät für Mathematik Informatik und Naturwissenschaften:	Prof. Dr. Heinrich Graener

Abstract

At the proposed International Linear Collider (ILC), the use of polarised electron and positron beams is a key ingredient of the physics program. A measurement of the polarisation with a yet unprecedented precision of $\delta\mathcal{P}/\mathcal{P} = 0.25\,\%$ is required. To achieve this, Compton polarimeter measurements in front of and behind the collision point are foreseen.

In this thesis, a novel concept for a detector for ILC polarimetry is introduced to eliminate one of the dominating systematics limiting the previous best measurement of beam polarisation: a detector using quartz as Cherenkov medium could increase the tolerance against non-linear photodetector responses. The high refractive index of quartz results in a higher Cherenkov light yield compared to conventional Cherenkov gases. This could allow single-peak resolution in the Cherenkov photon spectra produced by the Compton electrons at the polarimeters.

The detailed simulation studies presented in this work imply that such single-peak resolution is possible. Considerations for the choice of a suitable detector geometry are discussed. A four-channel prototype has been constructed and successfully operated in a first testbeam campaign at the DESY testbeam, confirming simulation predictions. Although further studies have to be considered to quantify all aspects of the detector response, the findings of the analysis of the data from the first testbeam are promising with regards to reaching the desired light yield.

In the final part of this thesis, the application of a detector concept allowing single-peak resolution to the polarisation measurement at the ILC is examined. Two of the main sources of systematic uncertainties on the polarimeter measurements are detector non-linearities and misalignments. The performance of the suggested quartz detector concept in Monte Carlo studies promises a control of these systematics which meets the precision requirements for ILC polarimetry.

Zusammenfassung

Am geplanten International Linear Collider (ILC) ist der Einsatz von polarisierten Elektron- und Positron-Strahlen einer der zentralen Bestandteile, um die angestrebten Präzisionsmessungen zu verwirklichen. Dazu ist die Messung der Strahlpolarisation mit einer nie zuvor erreichten Genauigkeit von $\delta\mathcal{P}/\mathcal{P} = 0{,}25\,\%$ erforderlich. Zu diesem Zweck sind Messungen mit Compton-Polarimetern vor und nach dem Wechselwirkungspunkt beabsichtigt.

In dieser Arbeit wird ein neuartiges Konzept für einen Detektor für die ILC-Polarimetrie präsentiert, um eine Hauptquelle systematischer Unsicherheiten auszuschalten, die bei den besten Messungen in der Vergangenheit ein limitierender Faktor war: ein Detektor, bei dem Quarz als Čerenkov-Medium verwendet wird, könnte die Toleranz gegenüber Photodetektor-Nichtlinearitäten erhöhen. Der hohe Brechungsindex von Quarzglas führt zu einer größeren Ausbeute an Čerenkov-Licht im Vergleich zu konventionellen Čerenkov-Gasen. Das könnte erlauben, die Beiträge einzelner Compton-Elektronen zu den am Polarimeter gemessenen Photonspektren aufzulösen.

Die detaillierten Simulationsstudien, die in dieser Arbeit vorgestellt werden, lassen darauf schließen, dass so ein Auflösungsvermögen erreicht werden kann. Erwägungen bei der Auswahl einer geeigneten Detektor-Geometrie werden diskutiert. Ein Prototyp-Detektor mit vier Kanälen wurde konstruiert und erfolgreich in einer ersten Messkampagne im Teststrahl am DESY eingesetzt, wobei Vorhersagen der Simulation bestätigt werden konnten. Obwohl weitere Studien nötig sind, um alle Aspekte der Detektorantwort zu quantifizieren, sind die Ergebnisse der ersten Teststahl-Messungen vielversprechend im Hinblick auf das Erreichen der angestrebten Lichtausbeute.

Im letzten Teil dieser Arbeit wird der Einsatz eines Detektorsystems mit der angestrebten Auflösung einzelner Compton-Elektronen zur Polarisationsmessung am ILC untersucht. Zwei der Hauptquellen für systematische Unsicherheiten bei den Polarimeter-Messungen sind Detektor-Nichtlinearitäten und Ausrichtungsfehler. Die Leistung des vorgeschlagenen Quarzdetektor-Konzepts in Monte Carlo-Simulationen verspricht eine Kontrolle dieser Unsicherheiten, die die Ansprüche für die Genauigkeiten erfüllt.

Table of contents

1

Introduction

The Standard Model of particle physics describes our current knowledge of the fundamental particles and their interactions. It is currently regarded the best description of electromagnetic, weak and strong interactions up to the energies investigated during the last decades. In the decades since its formulation, several experimental evidences have been accumulated: The Standard Model predicted the existence of elementary particles to mediate the weak interaction and the strong force, as well as the existence of three quark generations, before the experimental discovery of the W and Z bosons, gluons, and the charm and top quarks. The latest success was the discovery of the Higgs boson by the ATLAS and CMS experiments [1, 2], announced July 4^{th}, 2012. This confirmed the theoretical mechanism proposed by P. Higgs, F. Englert and R. Brout to describe the mass generation of elementary particles, which was awarded with the Nobel Price in Physics in the year 2013.

Despite the long list of successes of the Standard Model, several unsolved questions still exits, and it is widely accepted that current formulation Standard Model is not the final theory to completely describe fundamental interactions. One hint at physics beyond the Standard Model are cosmological observations indicating that only about 4 % of the energy density in the universe consists of ordinary baryonic matter. For the other 96 %, the Standard Model offers no explanation. Another example is the CP-violation predicted from the Standard Model, which is by a factor of about 10^8 too small to cause the matter-antimatter asymmetry observed in the universe. Theories for new physics have been formulated to address the shortcomings of the Standard Model, for example by offering candidates for dark matter particles or introducing additional sources of CP-violation beyond Standard Model expectations.

The validity of such theories has to be settled via experiments. A lepton collider with polarised beams would be a powerful tool to extend precision of Standard Model knowledge and look for signatures of new physics. A proposed future e^+e^- collider is the International Linear Collider (ILC). The ILC is planned as a linear accelerator with centre-of-mass energies up to 500 GeV (with the possibility to upgrade to 1 TeV). The baseline design foresees a longitudinal polarisation of 80 % for the electron beam and 30 % for the positron beam (with the possibility to upgrade to 60 %).

The use of highly polarised beams has many benefits in Standard Model precision tests as well as in the search for new particles and the measurement of their interactions, provided that the beam polarisation can be determined precisely enough that systematics from the polarisation uncertainty are at a negligible level. One example for an application where beam polarisation is a key element this is the study of the effective weak mixing angle $\sin^2\theta_{eff}$, which can be accessed trough the left-right polarisation asymmetry A_{LR}. In past measurements of the left-right asymmetry in the production of Z bosons from e^+e^- at SLC, the systematic uncertainties were dominated by the polarisation measurement[3]. This emphasises the need for high precision polarimetry.

To directly measure the beam polarisation, the use of Compton polarimeters is foreseen. One of the limiting factors for the precision of the polarimeter measurements is the detector non-linearity. In this thesis, the development of a quartz Cherenkov detector concept that addresses this challenge is presented.

Overview of this thesis

In the first part, a short overview of the main components of the planned International Linear Collider and the physics case for polarised beams is given (chapter 2).
The concepts for polarisation measurement at the ILC are introduced in chapter 3.
The requirements for the detectors used at the ILC polarimeters will be introduced in chapter 4, along with an outline of an existing detector concept and the motivation for the development of an alternate concept using quartz Cherenkov detectors.
In chapter 5, simulations studies for the design of such a quartz detector are presented.
The construction of a prototype detector based on these studies and its operation at the DESY testbeam are described in chapter 6.
Chapter 7 evaluates how such a quartz detector would perform if it was applied at the ILC polarimeters.
The results of this thesis are summarised in the final chapter.

2

The International Linear Collider

The most powerful collider in high energy physics today is the Large Hadron Collider (LHC) at CERN, built to study proton-proton interactions with centre-of-mass energies up to 14 TeV, as well as heavy ion collisions. It reaches beyond the energy range accessible to former collider experiments. However, its precision capabilities are limited, since protons are composite particles, so that the exact type and energy of the interaction between two colliding photons is unknown. In addition, the reconstruction of many processes is affected by large hadronic backgrounds. Therefore, a lepton machine would be an ideal tool follow up potential discoveries at the LHC with precision measurements, and, independent of LHC findings, perform high precision studies of Standard Model particles and interactions.

The International Linear Collider (ILC) is an electron positron collider proposed for this purpose. The baseline design for the ILC foresees tunable centre-of-mass energy between 200 GeV and 500 GeV, with the possibility to extend the reach up to 1 TeV. In the first 4 years of running, an integrated luminosity of 500 fb^{-1} will be collected, followed by another 500 fb^{-1} every two years at 500 GeV. It is planned to use polarised beams with a beam polarisation of $|\mathcal{P}(e^-)| \geq 80\,\%$ for the electrons and $|\mathcal{P}(e^+)| \geq 30\,\%$ for the positrons.

The well known and clean initial state, in combination with the beam polarisation and the capacity for threshold scans, offers a promising approach for precision measurements. The 125 GeV Higgs boson discovered at the LHC lies well within energy range of the ILC, allowing to determine its properties precisely at the ILC, and to determine if they match a Standard Model Higgs boson or point to new physics beyond the Standard

Model. If the LHC discovers new particles in the future, the ILC will likely by an excellent tool to determine their properties as well.

Even if no phenomena beyond the Standard Model are discovered at the LHC at higher energies, discoveries are still possible at the ILC, despite the lower energy. The measurement precision may allow for extrapolation to much higher mass scales, e.g. in the context of supersymmetric spectra with small mass gaps between the two lightest supersymmetric particle precision masses. Such scenarios are for example motivated by dark matter co-annihilation, but the small mass differences would make them difficult to detect at the LHC.

Recently, Japan has voiced a strong interest to host the ILC. In June 2013 a Technical Design Report was published[4–8]. It's five volumes contains realistic technical design and implementation plans, including acceleration technologies, detector concepts and engineering studies.

2.1 The ILC accelerator

The entire ILC accelerator complex will be ∼31 km long. A sketch of the accelerator and its major components is shown in figure 2.1. Details on the accelerator technology can be found in [6, 7].

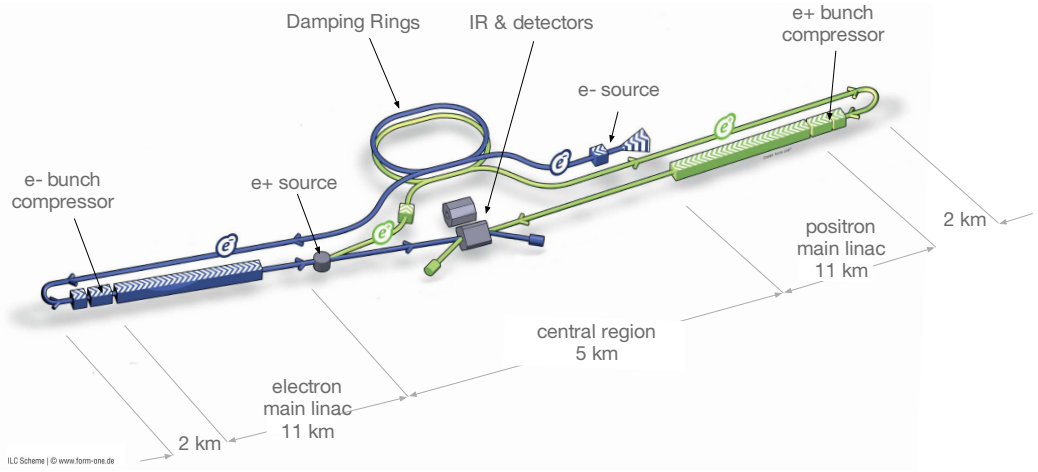

Figure 2.1: Schematic view of all major subsystems of the ILC[4].

At the beginning of the acceleration process, polarised electrons are produced in a source based on a photocathode DC gun. A strained GaAs target is illuminated by a laser matching the band gap. The emitted electrons are naturally polarised to a level of ≈85 %.

The production of polarised positrons is less straightforward. The positron source system is sketched in figure 2.2. The positrons are created by passing the high-energy main electron beam through an undulator in order to produce high-energy photons. By using an undulator with helical windings, circular polarisation of the photons is obtained. When these photons are shot on a target, they create pairs of longitudinally polarised electrons and positrons. The positrons are selected my a magnetic chicane and accelerated.

After their creation the electron and positron beams have large transverse and longitudinal emittances. To reach the low emittance required for high luminosities, both beams enter damping rings after an initial acceleration to an energy of 5 GeV. To preserve the longitudinal polarisation, spin rotators in front of the damping rings rotate the polarisation vector into the vertical beam axis. After the damping inside the 3.2 km long electron and positron damping rings is accomplished, the beams are extracted and transported through the 15 km long Ring to Main Linac systems, still at 5 GeV. During this transport, spin rotators orient the beam polarisation to the desired direction. Other subsystems along the transport line to achieve the desired beam quality are collimation systems and a set of bunch compressors, in which the beams are compressed to the length of a few hundred microns and simultaneously accelerated to 15 GeV.

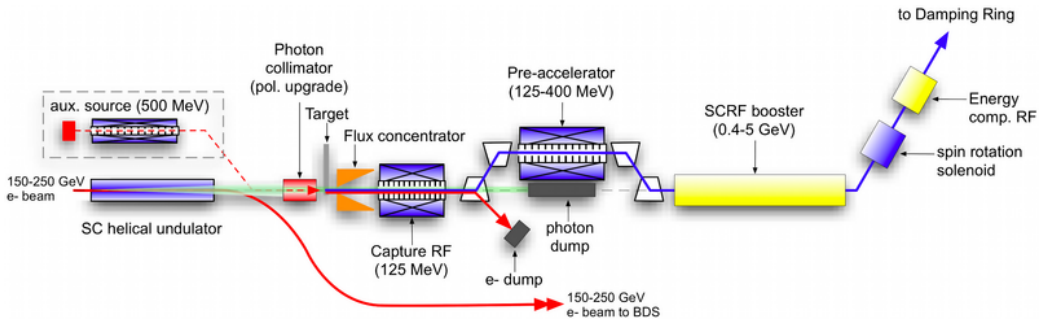

Figure 2.2: Layout of the ILC positron source[4].

The acceleration to the final beam energies happens inside the 11 km long main linacs, using technology based on 1.3 GHz superconducting radio-frequency cavities with an average accelerating gradient of 31.5 MV/m. At the end of the main linacs, the beam-delivery systems (BDS) are located. Inside these 2.2 km long systems, a wide range of beam diagnostic systems is located, including energy spectrometers and the polarimeters. Final focus magnets bring the beams into collision with a crossing angle of 14 mrad at a single interaction point. After the interaction, the spent beams are transported through an extraction line, containing additional energy and polarisation diagnostics, on towards the beam dump.

2.2 Detectors at the ILC

Past colliders have benefited from the complementary operation of two or more independent detectors. Therefore a so-called “push-pull“ system is planned for the ILC interaction region to allow an exchange between two detectors at the interaction point on short times scales. The two detector concepts foreseen are the Silicon Detector (SiD)[11] and the International Large Detector (ILD)[12]. Both concepts have been designed to achieve the requirements for the physics program over the full range of centre-of-mass energies.

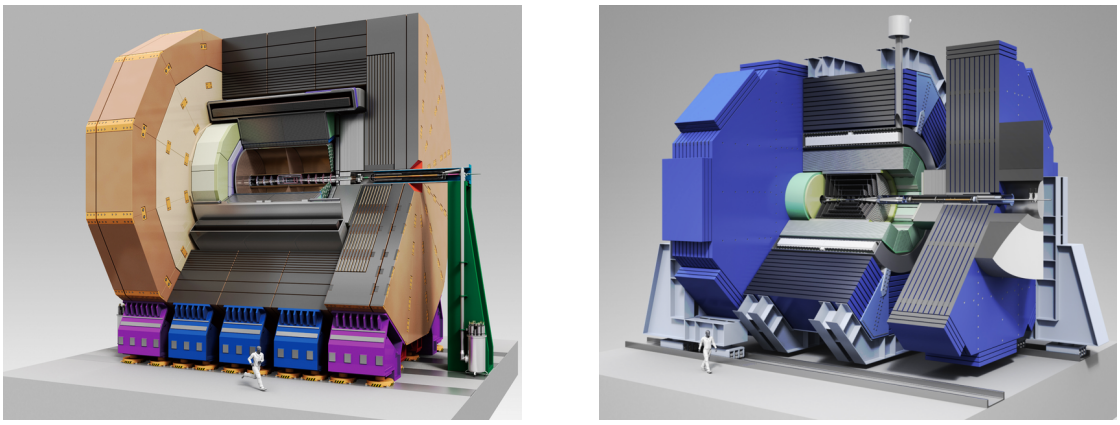

(a) (b)

Figure 2.3: Illustration of the ILC detector concepts (a) ILD and (b) SID [9, 10].

The detector design is driven by the requirements for the planned high precision measurements. For both detectors, the design is based on the particle flow concept, i.e. the combination of tracking information with measurements from calorimeters. To meet the resulting demands on the spatial resolution, highly granular calorimeters are foreseen, located inside a strong magnetic field to help in the separation of adjacent tracks. In addition, the material budget of the inner detector components has to be minimised.

The technology for the tracking is the main difference between the two detector concepts. The main tracker at SiD will be a silicon tracker, while the ILD tracking concept is based on a hybrid system combining a time-projection chamber with silicon tracking layers, resulting in a larger size of the entire detector. An illustration of the two detector systems is shown in figure 2.3. More detail on the design and performance of both detectors can be found in [8].

2.3 Physics program with polarised beams

The ILC physics program comprises a large spectrum, from precision measurements of Standard Model physics and investigations of the Higgs sector to search for / possible study of physics beyond the Standard Model.

A detailed description of the ILC physics case can be found in the volume 2 of the ILC technical design report[5]. In the following the focus is on example cases that stress the role of polarised beams.

The focus of this thesis is on longitudinal beam polarisation, which is a part of the ILC baseline design. For completeness' sake it should be mentioned that physics program at the ILC would benefit also from transversely polarised beams. Transverse polarisation would offer provide new observables, such as azimuthal asymmetries, which are sensitive to non-standard interactions, and offer possibility to detect even small CP-violating phases. More information on this, as well as on the physics case for polarised beams, can be found in [13]. A few examples for the motivation for longitudinally polarised beams are summarised below.

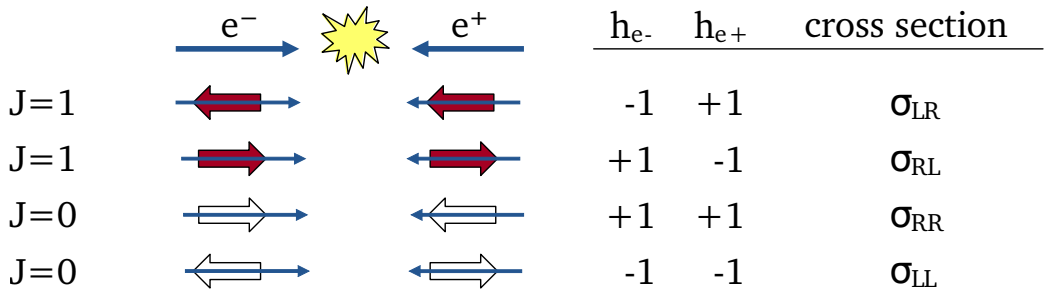

Figure 2.4: The different helicity combinations in e^+e^- collisions and the corresponding cross sections[14]. The long narrow arrows represents the direction of motion of the particles and the shorter thick arrows their spin direction.

The longitudinal polarisation is defined as

$$\mathcal{P}_z = \frac{N_R - N_L}{N_R + N_L}, \tag{2.1}$$

with $N_{R,L}$ the number of right-/left-handed particles in a bunch, i.e. a polarisation of $\mathcal{P}_z = 1$ means that the spins of all particles are oriented parallel to their direction of motion Figure 2.4 shows the various combinations of spin configurations possible in e^+e^- collisions.

Since in the following only the longitudinal polarisation will be discussed, it will from now on simply be referred to as the polarisation $\mathcal{P} \equiv \mathcal{P}_z$.

The benefits of longitudinal polarisation can be seen when one considers the two different production modes possible at the ILC: s-channel annihilation and t/u channel exchange diagrams:

In s-channel annihilation, the helicities of the incoming electron and positron couple directly to each other (figure 2.5(a)). In the Standard Model process of e^+e^- annihilation into a vector boson, an electron annihilates a positron of the opposite helicity ($e_L^- e_R^+$ and $e_R^- e_L^+$). The collision cross section for this annihilation can be enhanced by using polarised beams with opposite signs for electron and positron polarisation.
In return, new physics with scalar particles as propagator in the s-channel searches could appear unsuppressed in the combinations $e_L^- e_R^-$ and $e_R^+ e_L^+$. In searches for such particles the corresponding beam polarisation could be used to suppress Standard Model background.

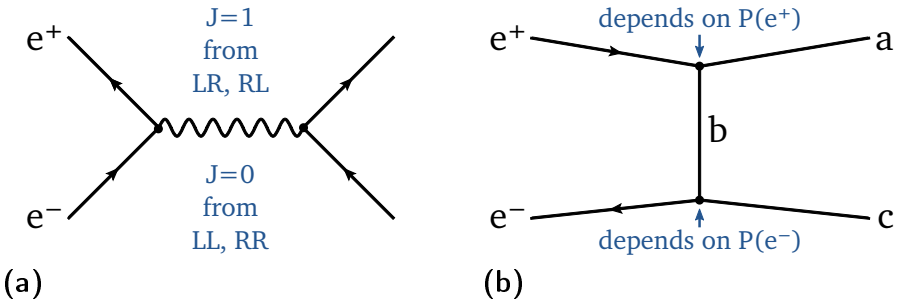

Figure 2.5: (a) In annihilation diagrams, the helicities of the incoming e^+e^- are directly coupled, while in (b) exchange diagrams the helicity of the incoming particle is directly coupled to the final particle (based on [13]).

In t/u-channel scattering, the helicities of the incoming beams are directly coupled to the helicities of the final particles (figure 2.5(b)). In principle, all helicity combinations can contribute to the production cross section of a process, but dependent on the coupling of the final particles to e^+/e^-, specific configurations of beam polarisations may be preferred. The arising asymmetries between the different polarisation configurations can be used to study the properties of the final particles, such as the chiral structure of their couplings.

For these reasons, polarisation an important component of the ILC physics program at all accessibly energies:

Part of the program are precision tests at low energies, i.e. at the Z resonance at 91 GeV and at the $e^+e^- \to W^+W^-$ threshold around 160 GeV. Beam polarisation provides crucial information for the study of the effective weak mixing angle $\sin^2\theta_{eff}$. It can be accessed directly through left-right asymmetry

$$A_{LR} = \frac{1}{\mathcal{P}_{\text{eff}}}\frac{\sigma_{-+} - \sigma_{+-}}{\sigma_{-+} + \sigma_{+-}}, \qquad \text{with } \mathcal{P}_{\text{eff}} = \frac{\mathcal{P}_{e^-} - \mathcal{P}_{e^+}}{1 - \mathcal{P}_{e^-}\mathcal{P}_{e^+}}, \tag{2.2}$$

where $\mathcal{P}_{\text{eff}}$ is the effective polarisation in the collisions and σ_{+-} and σ_{-+} are the cross sections for the configuration with the electron beam predominantly left-handed and the positron beam right-handed and the reversed combination, respectively (c.f. figure 2.4). The direct contribution of $\mathcal{P}_{\text{eff}}$ to equation (2.2) is one example why a precise knowledge of the beam polarisation is important for precision physics at the ILC.

Around 250 GeV the cross section for the Higgs-strahlung $e^+e^- \rightarrow ZH$ peaks. As explained above, opposite polarisation of electrons and positrons $e^-_L e^+_R$ and $e^-_R e^+_L$ enhances the luminosity, aiding in a precision study of the nature and couplings of the Higgs boson.

Near 350 GeV, the threshold for top quark pair production is located. From threshold scans, the mass can be determined to an accuracy of 100 MeV. With increasing energies around 400 GeV, top vector and axial vector couplings can be measured. This requires a study of the left-right asymmetry A_{LR} with high precision, emphasising again the need for polarised beams and precise polarimetry.

From 450 GeV on WW fusion becomes an important contribution to the Higgs production, allowing to study the Higgs coupling HWW. In the Standard Model, this process occurs predominantly from the $e^-_L e^+_R$ polarisation state. Running in this state will therefore greatly enhance the rates and suppresses backgrounds. In combination with branching ratio measurements from 250 GeV data, the total width of the Higgs boson can be determined.

Running at the final baseline energy of 500 GeV will increase power of Standard Model studies mentioned above. The search for new particles also benefits from use of the polarisation to suppress Standard Model background. In searches for dark matter particle pair-production in association with a photon, backgrounds can be reduced two orders of magnitude, leasing to significantly enhanced signature. In case such a dark matter signal is observed, measuring the cross sections with different polarisation configurations will provide additional information, allowing to determine the helicity structure of the interaction between WIMP and fermion[15] or, when an effective operator formalism is used to theoretically describe dark matter signals, to identify the operator type[16]. In addition, polarised cross sections will be important observables to determine the nature of newly discovered particles. Depending on the parameters of the new physics, they could also allow to study mixing parameters, for example between Gaugino and Higgsino in supersymmetric models.

Both in the case of Standard Model physics as well as for new physics beyond the Standard Model, polarisation will be an important tool.

3

ILC Polarimetry

The examples in section 2.3 demonstrate that beam polarisation plays an important role at the ILC, to enhance signal rates and suppress backgrounds by using suitable combinations of the beam polarisations, and to study the properties of the produced particles and their interactions. To benefit from the capability of the ILC to collide polarised electron and positron beams, a precise measurement of the polarisation is essential.

3.1 Polarimetry concept

The event rate of electro-weak processes depends on the luminosity and polarisation at the e^+e^- interaction point. Therefore, the luminosity-weighted average polarisation will be an important quantity for physics analysis at the ILC. It is defined as

$$\langle \mathcal{P} \rangle_{IP} = \frac{\int \mathcal{P}(t)\mathcal{L}(t)dt}{\int \mathcal{L}(t)dt}. \tag{3.1}$$

The luminosity $\mathcal{L}$ is expected to be measured with permille-level precision or better[17]. For polarimetry, a comparable precision is challenging. The design goal for polarimetry at the ILC is 0.25 %.

In order to obtain this goal, it is planned to instrument both the electron and positron beamline with Compton polarimeters before (“upstream“) and after (“downstream“) the e^+e^- interaction point. To relate their measurements to the polarisation at the

e^+e^- interaction point, spin tracking studies are performed. As absolute scale calibration, the long-term average of the polarisation can be determined from e^+e^- collision data. These three components of the polarisation measurements will be outlined in this chapter.

3.2 Polarimeters

3.2.1 Compton polarimetry basics

Compton polarimeters make use of the fact that the Compton cross-section for scattering between photons and electrons[I] is spin-dependent: the energy of recoil electron depends on product of photon and electron polarisation.

The unpolarised cross-section for Compton scattering at tree-level was already derived in 1929[18]. It can be described in terms of the dimensionless variables

$$x = \frac{4E_0\omega_0}{m^2}\cos^2(\theta_0/2), \qquad y = 1 - \frac{E}{E_0}, \qquad r = \frac{y}{x(1-y)} \tag{3.2}$$

where E_o (ω_0) are the initial energies of the electron (photon) before the scattering, E the electron energy after the scattering and m the electron mass. θ_0 is the crossing angle between electron and photon, which is foreseen to be very small at the ILC polarimeters (10 mrad for the upstream- and 15.5 mrad for the downstream-polarimeter), in which case $\cos^2(\theta_0/2) \simeq 1$.

With these variables, the unpolarised cross-section can be written as

$$\left(\frac{d\sigma}{dy}\right)_{\text{unpol}} = \frac{2\pi r_o}{x}\left[\frac{1}{1-y} + 1 - y - 4r(1-r)\right], \tag{3.3}$$

with the electron radius r_0.

[I] In the following, "electron" is used to denote both the electrons and the positrons, since the measurement concept is analogous.

In the polarised case, the cross-section is modified by a spin dependent term[19]:

$$\left(\frac{d\sigma}{dy}\right)_{\text{Compton}} = \left(\frac{d\sigma}{dy}\right)_{\text{unpol}} + \frac{2\pi r_o}{x} \cdot \boldsymbol{\lambda}\mathcal{P} \cdot rx(1-2r)(2-y), \tag{3.4}$$

where $\mathcal{P}$ is the longitudinal polarisation of the electron and λ is the circular polarisation of the photon. Figure 3.1(a) shows the resulting cross-section for the case of different products between laser and beam polarisation $\lambda\mathcal{P}$.

The asymmetry between cross-sections for opposite signs of $\lambda\mathcal{P}$ shown in figure 3.1(b) is defined as

$$\mathcal{A} = \frac{\sigma^-(\lambda,\mathcal{P}) - \sigma^+(\lambda,\mathcal{P})}{\sigma^-(\lambda,\mathcal{P}) + \sigma^+(\lambda,\mathcal{P})}, \tag{3.5}$$

where σ^- and σ^+ denote opposite and like sign helicity configurations of laser and electron beam.

Compton polarimeters use this asymmetry to measure the polarisation: circularly polarised laser light is shot onto the beam and causes a fraction of the beam electrons to undergo Compton scattering. The laser polarisation is flipped from $\lambda = +1$ to $\lambda = -1$ and back. After measuring the energy spectra of the scattered elec-

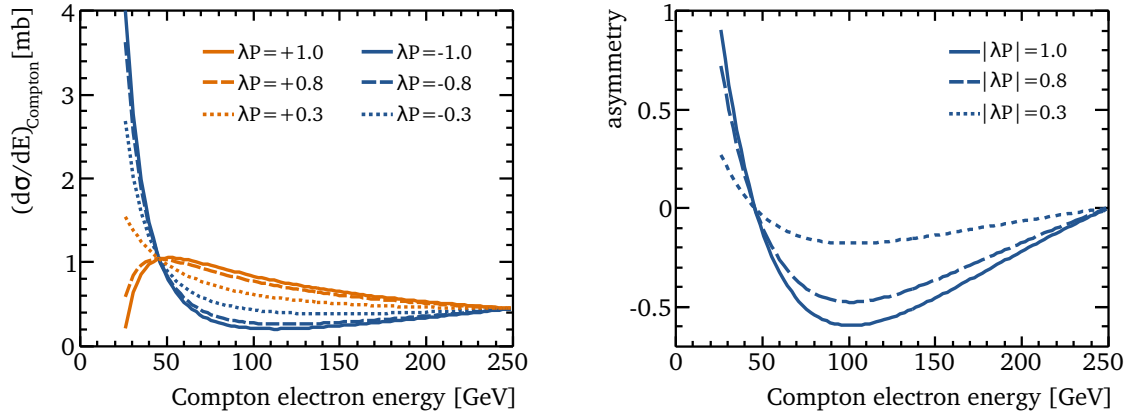

Figure 3.1: Properties of Compton scattering between polarised laser (with photon energy of 2.33 eV and electron beam (energy 250 GeV. (a) Differential cross-section in dependence of the energy of the scattered electron for different products $\lambda\mathcal{P}$ of laser and beam polarisation. (b) Asymmetry between the cross-sections of opposite laser polarisations.

trons for two opposite laser polarisations, the asymmetry between number of electrons N in a certain energy range for right and left circular polarised laser light can be calculated

$$\mathcal{A} = \frac{N^- - N^+}{N^- + N^+} \propto \mathcal{P}. \tag{3.6}$$

This quantity is proportional to the beam polarisation. Comparing the maximal possible asymmetry, the so-called analysing power $\mathrm{AP} = \mathcal{A}(\mathcal{P} = 1)$, to the measured asymmetry gives direct access to the polarisation:

$$\mathcal{P} = \frac{\mathcal{A}}{\mathrm{AP}}. \tag{3.7}$$

The Compton polarimeters at the ILC will be located inside magnetic chicanes, equipped with a laser system that can alternate between left and right circular polarisation configurations on a pulse-by-pulse basis. Inside the magnetic chicane, the energy distribution of the scattered electrons is transformed into a spatial resolution. The goal for the polarisation measurement, to provide measurements with a systematic uncertainty of 0.25 % or better, is a factor two better than the highest precision achieved until now (0.5 % for the SLC polarimeter[3]). That means that the instrumentation to detect the Compton electrons will need to meet challenging requirements (see section 4.1).

The up- and downstream polarimeters will complement each other: the upstream polarimeter is capable of an excellent time resolution, while the downstream polarimeter gives access to collision effects. Measurements in the absence of collisions can be used to cross-calibrate the polarimeters.

The main characteristics of the upstream and downstream polarimeters are briefly introduced in the following sections. More detailed descriptions can be found in [20].

3.2.2 Upstream polarimeter

The planned location for the upstream polarimeters is ≈1.8 km in front of the e^+e^- interaction point.

A conceptual sketch of the upstream polarimeter chicane is shown in figure 3.2. The laser-bunch interaction point will be at the centre of a dedicated chicane (≈75 m long), consisting of four sets of dipole magnets. The laser and beam parameters at the upstream polarimeter are listed in the left column of table 3.1. The clean beam conditions and low background rates allow to measure the polarisation of each bunch in a bunch train. Consequently, the upstream polarimeter can be used to keep track of time-dependent effects on short time scales.

Only a tiny fraction of the full bunch takes part in the Compton scattering, ∼1000 electrons per bunch crossing. The scattering angle is $\lesssim 10\,\mu$rad[19]. The third and fourth dipole of the magnetic chicane separate the scattered electrons from the undisturbed beam. The measurement is considered non-invasive, since the remaining electrons of the bunch continue towards the e^+e^- interaction point. The magnetic chicane also transforms the energy distribution of the scattered electrons into a spatial distribution. Behind the chicane, the horizontal distribution is detected over an area ≈20 cm wide.

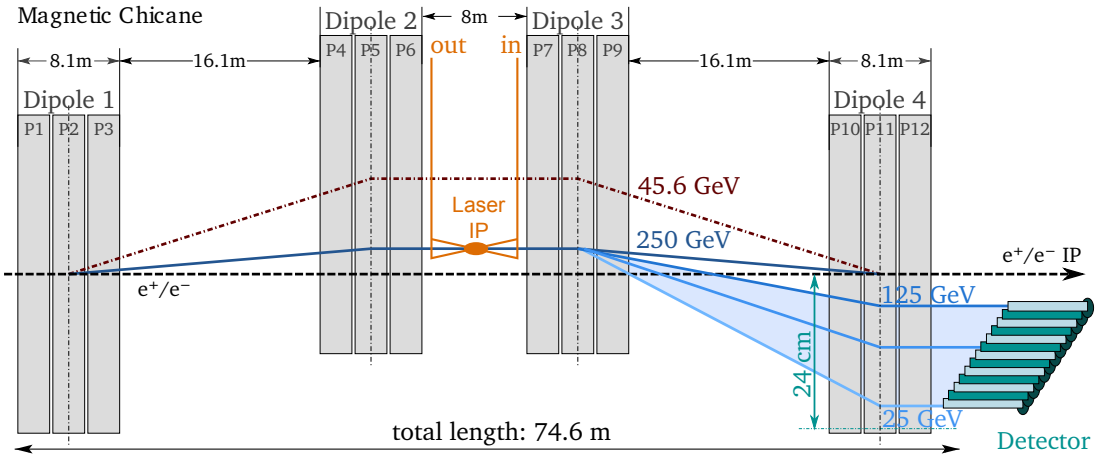

Figure 3.2: Sketch of the upstream polarimeter chicane (after [20]).

	Laser beam		e^+/e^- beam
	Upstream	Downstream	
Energy	2.33 eV	2.33 eV	45.6 - 500 GeV
Bunch charge/energy	35 µJ	100 mJ	$2 \cdot 10^{10}$ e
Bunches per train	1312 - 2625	1	1312 - 2625
Bunch length σ_t	10 ps	2 ns	1.3 ps
Average power	0.2 - 0.5 W	0.5 W	

Table 3.1: Laser and electron beam parameters at the polarimeters[21].

3.2.3 Downstream polarimeter

The downstream polarimeters will be located ≈150 m behind the e^+e^- interaction point. At this location, significant background levels have to be considered.

To avoid the synchrotron radiation from the e^+e^- interaction point, the detectors for the scattered Compton electrons are placed further away from the main beam axis, requiring higher magnetic fields. In total, six dipoles are foreseen for the downstream polarimeter chicane, as illustrated in figure 3.3.

To overcome the larger background levels, a significantly higher laser power per shot is used. While this allows to maintain a suitable signal-to-background ratio, it will also lead to longer pulse duration. A single laser can only shoot at one electron bunch per train. The overall sampling statistics can be increased by employing several lasers instead of one.

Despite the lower sampling rate, the downstream polarimeters complement the upstream polarimeters: depolarisation effects in the collision can be monitored. If the spin transport between the polarimeters is well understood, the polarimeters can be cross-calibrated by measuring in the absence of collisions.

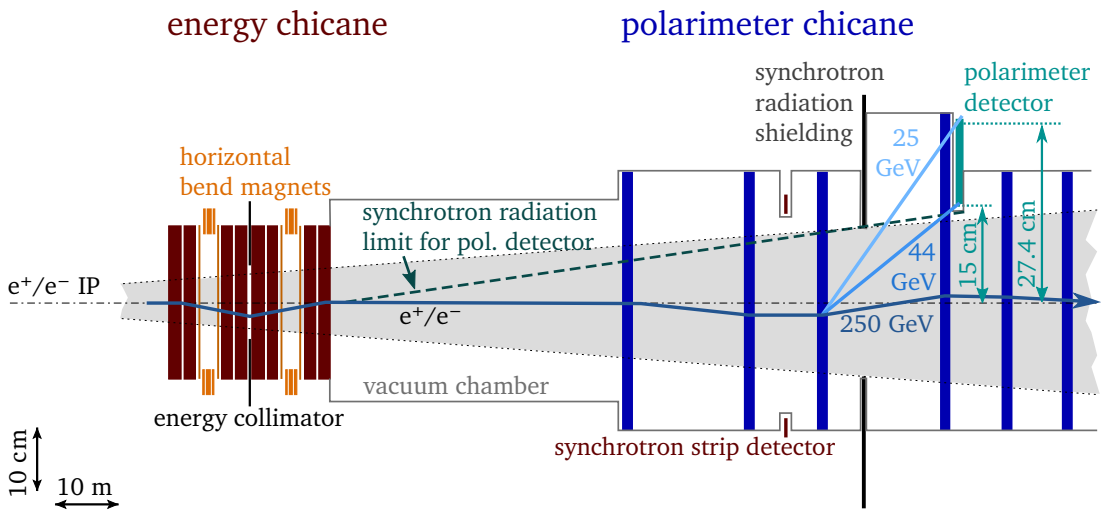

Figure 3.3: Sketch of the downstream polarimeter chicane (after [20]).

3.3 Spin tracking

The quantity of interest for physics analysis is the luminosity-weighted polarisation average at the e^+e^- interaction point. To determine this from the measurements at the polarimeters, a detailed knowledge of how the polarisation evolves along the beam delivery system is necessary, along with an understanding of collision effects.

Important influences on the polarisation are strong beam-beam-effects at the e^+e^- interaction point and misalignments of the lattice elements in the beam delivery system, e.g. induced by ground motion. A dedicated software framework exists to simulate the transport through the beam delivery systems, the collisions and also the measurements at the polarimeters[22], showing that it is possible to cross-calibrate the polarimeters to 0.1 % in the absence of collisions. For the operation with collisions, it was found that a monitoring of the spent beam properties on a level of 10 %, which is possible by combination of all means to monitor the beam parameters, e.g. from energy spectrometers, the monitoring of the instantaneous luminosity, beamstrahlung and pair backgrounds, is required to predict the depolarisation in collisions to about 0.1 %. Then both the upstream and the downstream measurements can be individually extrapolated to the e^+e^- interaction point for a complementary extraction of the luminosity-weighted polarisation[21].

3.4 Collision data

The measurement of a physics process that is sensitive to the polarisation can be used to extract the long-time average value of the luminosity-weighted polarisation.

One possible technique is the so-called “modified Blondel scheme“. While the original Blondel scheme proposed also the collection of unpolarised data[23], the modified method does not require the use of unpolarised beam. It which can be applied to any well-known polarisation dependent process: The absolute value of e^+ and e^- polarisation is obtained by measuring total cross-sections for all four possible polarisation configurations of the electron and positron beam ($++$, $+-$, $-+$ and $--$). Assuming that the absolute beam polarisation stays constant for helicity reversal, it can be calculated from [24]

$$\langle | \mathcal{P}_{e^\pm} | \rangle_{IP} = \sqrt{\frac{(\sigma_{+-} + \sigma_{-+} - \sigma_{--} - \sigma_{++})(\mp\sigma_{-+} \pm \sigma_{+-} + \sigma_{--} - \sigma_{++})}{(\sigma_{-+} + \sigma_{+-} + \sigma_{--} + \sigma_{++})(\mp\sigma_{-+} \mp \sigma_{+-} - \sigma_{--} + \sigma_{++})}} \tag{3.8}$$

where σ_{+-} is total cross-section for $P(e^-, e^+) = (+x\%, -y\%)$, and so on, while $\mathcal{P}_{e^+}$ and $\mathcal{P}_{e^-}$ are the resulting positron and electron beam polarisations respectively. The included assumption that $\mathcal{P}_+(e^-) = -\mathcal{P}_-(e^-)$ and $\mathcal{P}_+(e^+) = -\mathcal{P}_-(e^+)$ necessitates fast helicity reversal to cancel time dependent effects, and continuous monitoring of the polarisation with the polarimeters to apply corrections for slight differences in the absolute value of the polarisation.

One example for a process which has been extensively studied is WW production, which is especially suitable due to the large, highly polarisation-dependent cross-section. For simulated data sets with an integrated luminosity of $500\,\mathrm{fb}^{-1}$, the precision obtained with for an electron polarisation of 80 % and a positron polarisation of 30 % (60 %) was $\sim 0.1\,\%$ ($\sim 0.2\,\%$) for the electron beam and $\sim 0.22\,\%$ ($\sim 0.5\,\%$) for the positron beam[25].

Another method to determine the average luminosity-weighted polarisation from the same process is an angular fit method. Compared to the modified Blondel scheme, an additional information is used, namely the angle of the W^--bosons with respect to the

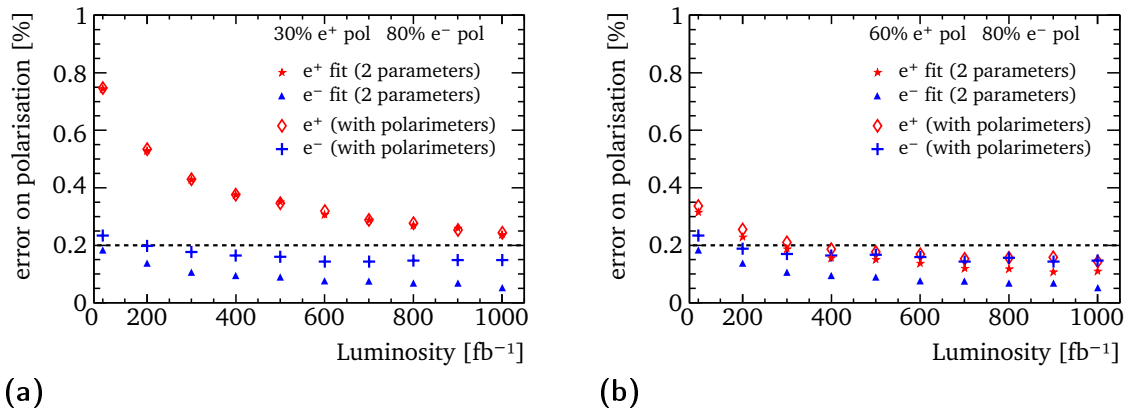

Figure 3.4: Precision achievable for the determination of the beam polarisation from the angular fit method with and without taking into account an 0.25 % polarimeter uncertainty. The distributions are shown for 80 % electron polarisation and (a) 30 % and (b) 60 % positron polarisation (after [25]).

beam axis. This technique uses a template fit of the angular distribution for different simulated sets of beam polarisation to the data. In a study comparing the performance of the angular fit and the modified Blondel scheme, the angular fit appears to be more powerful, yielding a precision of $\sim 0.1\,\%$ for the electron beam and $\sim 0.35\,\%$ for the positron beam for an electron polarisation of 80 % and a positron polarisation of 30 % at $500\,\mathrm{fb}^{-1}$, while for 60 % positron polarisation the desired precision of 0.2 % for both beams could already be obtained at $250\,\mathrm{fb}^{-1}$[25]. Figure 3.4 shows how the results obtained with this method change between the idealistic case, where one assumes that the magnitude of the polarisation stays perfectly constant after helicity reversal, and a more realistic study including a measurement of the polarisation with a polarimeter precision of 0.25 %.

In general, one can say that both techniques offer very good precision for high integrated luminosities. They are not meant as a replacement of the polarimeters, since they require a large enough data sets, i.e. on data taking on the order years, for reaching permille level precision and make some assumptions which need to be checked with the polarimeters. For the precision goal envisaged at for polarimetry at the ILC, a combination of the different components of the polarisation measurement presented in this chapter will be necessary.

4

Polarimeter detectors

In this chapter, the requirements and possible options for the detectors at the ILC polarimeter chicanes are described. Due to the high event rate, the uncertainty of the polarisation measurement becomes completely dominated by systematics within a few seconds. The main sources of systematic uncertainty are discussed in section 4.1. The current baseline detector concept is introduced in section 4.2.1. Finally, the alternative detector concept which will be the focus of this thesis is motivated in section 4.2.2.

4.1 Detector requirements

The polarimeter detectors need to be radiation-hard enough to withstand a radiation exposure of up to 1 MGy per year at the upstream polarimeter. Detectors with such robustness can also be expected to be suitable for use at the downstream polarimeter, despite the presence of the larger beam backgrounds and increased laser power, since only one or a few bunches out of the entire bunch train are hit by the laser.

In contrast, at the upstream polarimeter chicane each bunch in a train will be measured. For the beam parameters foreseen for the ILC, this amounts to 1312 to 2625 bunches during a bunch train duration of 1 ms[4]. Consequently, the polarimeter detectors need to be capable of readout rates $\mathcal{O}$(MHz).

To meet the demands on speed and radiation hardness, Cherenkov detectors are a simple solution: the emission of Cherenkov light is proportional to the number of

source of uncertainty	$\delta\mathcal{P}_z/\mathcal{P}_z$	
	SLC achieved	ILC goals
laser polarisation	0.1 %	0.1 %
detector alignment	0.4 %	0.15 % to 0.2 %
detector linearity	0.2 %	0.1 %
electronic noise and beam jitter	0.2 %	0.05 %
Total	0.5 %	0.25 %

Table 4.1: Breakdown of the budget for different sources of uncertainty for polarisation measurement at the ILC[21]. For comparison, the systematic uncertainties determined for the SLC polarimeter are also given[3].

electrons. At ILC beam energies, the Compton scattered particles are relativistic, and the light emission is independent of their energy. A number of radiation hard Cherenkov materials exist, such as gases and quartz. Cherenkov detectors were already successfully operated at the SLC polarimeter, where a precision of $^{\delta\mathcal{P}}/_{\mathcal{P}} \leq 0.5\,\%$ was achieved (c.f. table 4.1). To reach the higher precision goal for ILC polarimetry, the development of a detector system with improved alignment precision and linearity is necessary.

Due to the high event rate, the statistical uncertainty of the polarisation measurement rapidly becomes negligible compared to the systematic uncertainties, which will dominate the precision of the polarisation measurement already after a few minutes of data taking.

The main sources of uncertainty are the laser polarisation, the alignment of the detector, and non-linearities in the response of the photodetectors used to measure the Cherenkov light. The error budget currently envisioned for the different sources of uncertainty is summarised in table 4.1.

The laser polarisation was already successfully controlled on the level of 0.1 % at the SLC polarimeter[3]. Therefore, it is assumed that obtaining a laser system with the same or even better performance will not pose a problem for polarimetry at the ILC.

However, to fulfil the envisaged precision goal of an uncertainty $^{\delta\mathcal{P}}/_{\mathcal{P}} \leq 0.25\,\%$, the control of detector linearity and alignment remain challenging.

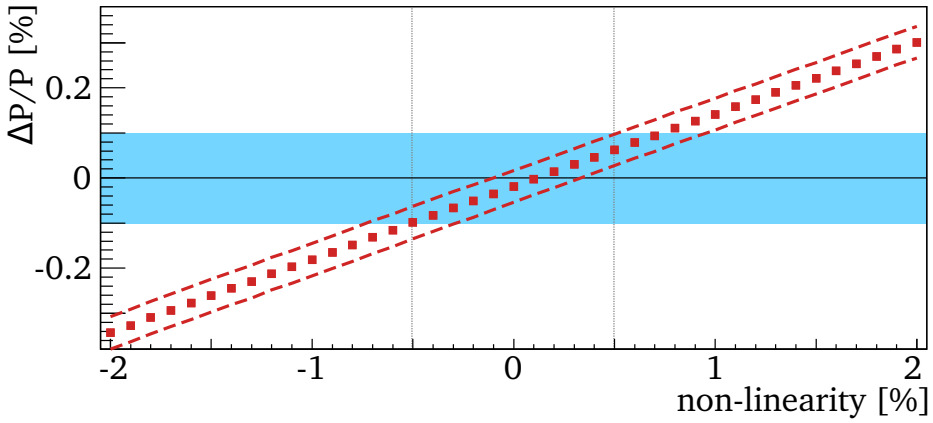

Figure 4.1: Dependence of the polarisation uncertainty on the detector linearity for the existing detector concept (c.f. section 4.2.1). A quadratic non-linearity was added to a linear detector response. To stay below the error budget marked by the blue band, the non-linearity of the detector output has to be controlled to a level better than 0.5 % (after [26]).

The detector signal needs to be very linear over a large dynamic range. Depending on the size of the detector channels, a difference up to factor 100 in the number of electrons for the two helicities can be expected near the Compton edge. For the default detector concept described in section 4.2.1, Monte Carlo studies showed that any non-linearities in the detector signal need to be below 0.5 % to stay within the assigned error budget of 0.1 % contribution to the polarisation measurement (see figure 4.1).

For the calculation of the analysing power, the horizontal position of the Compton edge has to be known with a precision $\mathcal{O}(0.1\,\text{mm})$, while tilts of the detector should be controlled with a precision of 1 mrad[27].

4.2 Cherenkov detector concepts

The basic design concept for the detector at the ILC polarimeters consists of an array of Cherenkov detector channels. The detector channels will be instrumented with photodetectors to measure the amount of Cherenkov light produced in a channel, as a measure for the number of electrons in that detector channel.

The number of Cherenkov photons produced when a particle with charge Ze passes through a Cherenkov detector is given by the Frank-Tamm formula[28, 29] as

$$\frac{d^2N}{dxd\lambda} = \frac{2\pi\alpha Z^2}{\lambda^2}\left(1 - \frac{1}{\beta^2 n^2(\lambda)}\right) \tag{4.1}$$

where α is the fine structure constant, $\beta = {}^{v}/_{c}$, n the refractive index and λ the wavelength of the emitted Cherenkov radiation. From this equation one can see that the amount of light increases for larger refractive indices n. The intensity of the emitted Cherenkov light is larger for smaller wavelengths λ. Sensitivity in the UV-range is therefore important in choosing the photodetector type for use with the Cherenkov detectors. A classic choice for a photodetector is a photomultiplier tube, combined with a charge-to-digital converter (QDC) to digitise the photomultiplier signal.

4.2.1 Conventional concept: gas Cherenkov detector

The baseline concept to detect the Compton-scattered electrons (or positrons) at the ILC polarimeters is an array of about 20 staggered "U-shaped" aluminium channels[20], each equipped with a calibration system on one end and a photodetector on the other, as depicted in figure 4.2(a). The channels are filled with a gas with refractive index $n > 1$, e.g. perfluorobutane, as Cherenkov medium. The choice of perfluorobutane makes the detector robust against background from low energetic particles, since its refractive index of n=1.00137 at 404.7 nm[30] leads to a high threshold of 10 MeV. The light emitted by the Compton-scattered electrons traversing the gas in the horizontal base part of the detector is reflected upwards towards the photodetectors. The U-shape ensures that the photodetectors are kept out of the beam plane. From simulation studies, ≈60 Cherenkov photons are expected to reach the photocathode per Compton electron, which results in an average of 6.5 photoelectrons emitted from the photocathode when the wavelength spectrum of the Cherenkov radiation and the quantum efficiency of a UV-sensitive photomultiplier are taken into account[31].

A two-channel prototype for this detector concept was built and tested. Details on the prototype and its performance during test beam campaigns can be found in [27].

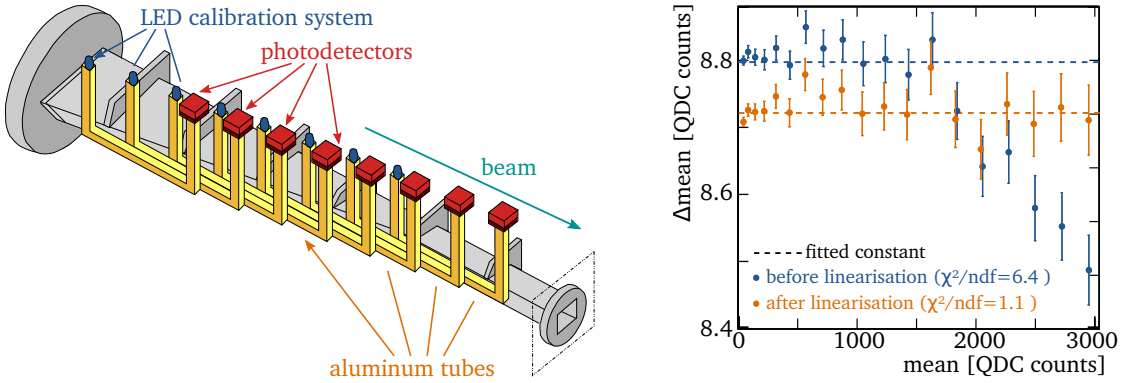

Figure 4.2: Gas detector concept for the ILC polarimeter. (a) Sketch to illustrate a setup with staggered "U-shaped" channels as Cherenkov detector, with an LED calibration system on one end and a photodetector on the other (after [27]). For better visibility, only eight channels are shown. (b) Test of the differential calibration method. The difference in the signal of a base LED pulse with and without a small additional pulse for different base pulses is shown before (blue) and after (orange) application of the correction function derived from an independent data set (after [32]).

To control the detector non-linearities to meet the requirement listed in table 4.1, and to derive a correction function, an LED calibration system has been developed: The differential non-linearity is determined by measuring the difference in the detector output with and without a small secondary pulse in addition to a tune-able base pulse. For perfect linearity, the difference should stay constant for all intensities of the base pulse. The measured non-linearity in the detector response can be used to determine a transfer function to linearise the detector output. In a test setup, the differential non-linearity of one of the photodetectors used with the two-channel gas detector prototype was characterised. After application of the calibration method, a residual non-linearity $<0.2\,\%$ was reached in the expected dynamic range of the polarimeter (see figure 4.2(b)). Monte Carlo studies predict that non-linearities up to $4\,\%$ can be corrected successfully with this calibration system[32].

Apart from the non-linearity of the photodetectors, further non-linearities in the detector response could be introduced by the QDC used to digitise the charge signal from the photomultipliers. The non-linearities of the QDC models used with the prototype detector were measured and a correction function derived[33]. Overall,

shifts in the peak position of the photon spectrum measured in a detector channel were found to be below permille level. Therefore, the contribution of QDC non-linearities can be considered negligible compared to non-linearities from the photodetectors.

Figure 4.3(a) shows a simulated QDC spectrum for a mean of 5 Compton electrons in one detector channel and an average of 7 photoelectrons per Compton electron. The simulation assumes that the photodetector signal is amplified with a gain of $4 \cdot 10^5$ with a fixed noise level of 1 %. The main elements of the signal chain are modelled, including statistical fluctuations in the number of Compton electrons, number of photoelectrons and the amplification process, as sketched in figure 4.4. For the digitisation, a QDC with a resolution of 200 fC is assumed, corresponding to the one used with the gas Cherenkov detector prototype, whose linearity was studied in [33].

The polarisation can be calculated from the peak position in the QDC spectrum. The absolute value of the conversion Q from QDC bins to Compton electrons is not required for the polarisation measurement, since any constant in the calculation of the asymmetry cancels out.

$$\frac{Q_1 \cdot N^+ - Q_2 \cdot N^-}{Q_1 \cdot N^+ + Q_2 \cdot N^-} \overset{Q_1=Q_2}{=} \frac{N^+ - N^-}{N^+ + N^-} \tag{4.2}$$

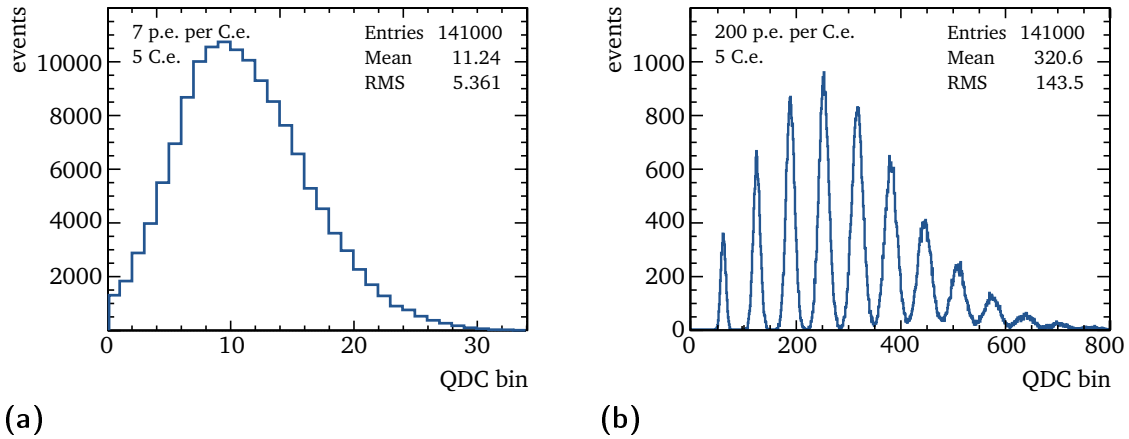

Figure 4.3: Simulated spectra for 5 Compton electrons in the detector with (a) 7 and (b) 200 detected photons per Compton electron.

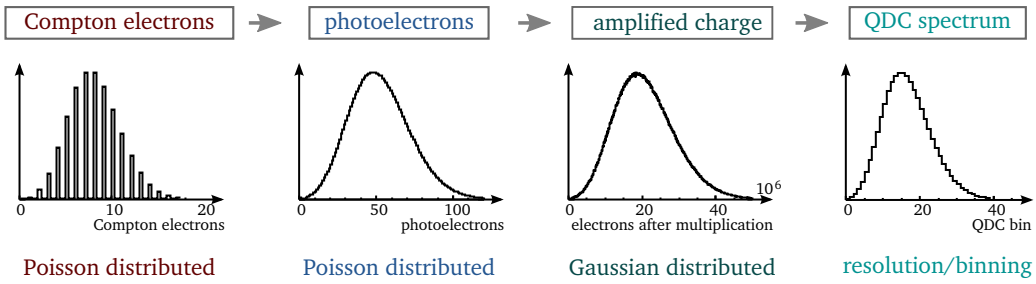

Figure 4.4: Schematic overview of the main components in the Monte Carlo simulation used to generate QDC spectra.

However, when the photodetector gain is not perfectly linear, i.e. $Q_1 \neq Q_2$, this will introduce a shift in the QDC spectrum which does not cancel out. As explained in section 4.1, such non-linearities were one of the major contributions to the uncertainty of the polarisation measurement at SLC. One tool to deal with this is the LED calibration system, which ensures that the condition $Q_1 = Q_2$ is met sufficiently well.

4.2.2 Alternative concept: quartz detector

While the performance of the LED calibration system is very promising, alternative detector concepts are also investigated to meet the demands on the linearity.

The case for single-peak resolution

If it were possible to resolve single peaks for each number of Compton electrons in one detector channel, this would allow to build a "self-calibrating" detector: by determining the distance between these peaks, the gain of the photodetectors could be monitored online, without dedicated calibration beam time.

For the ability to resolve single peaks in the Cherenkov light measurement, two factors are important: the number of Compton electrons $N_{\text{C.e.}}$ per detector channel, and the number of photoelectrons per electron $p := {}^{N_{p.e.}}/_{C.e.}$.

To illustrate this, figure 4.3(b) shows a simulated spectrum for a mean of 5 Compton electrons in one detector channel for a yield of 200 photoelectrons per Compton

electron (with otherwise unchanged parameters compared to the simulated gas detector spectrum in figure 4.3(a), except for the ∼ factor 7 higher number of photoelectrons per Compton electron). For such a configuration with a high number of detected photons in combination with a low number of Compton electrons, single peaks for individual numbers of Compton electrons can be distinguished. Fitting the shape of such a spectrum allows to determine the number of Compton electrons in this channel for the calculation of the asymmetry, without the need to calibrate the photomultiplier gain. A suitable fit procedure and its performance in light of the contribution of detector non-linearities to the polarisation uncertainty will be discussed in chapter 7.

The requirements for a detector system in which individual peaks can be resolved can be parametrised in terms of the number of Compton electrons per channel, the number of photoelectrons created at the photomultiplier cathode per Compton electron, and the resolution of the read out system, especially the noise of the photomultipliers.

Considering a number of photoelectrons per Compton electron following a Poissonian distribution with a mean of p, and $i_{\text{C.e.}}$ Compton electrons in a detector channel, a photoelectron distribution centred around $i_{\text{C.e.}} \cdot p$ with a width of $\sqrt{i_{\text{C.e.}} \cdot p}$ results, as

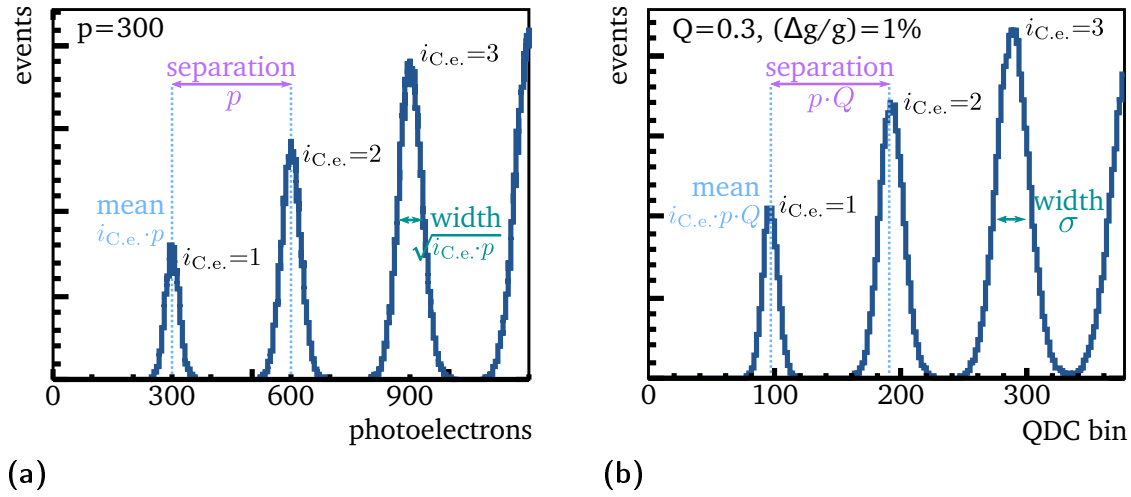

Figure 4.5: Illustration of peak position, width and separation as explained in the text, for the first three peaks in a simulated (a) photoelectron distribution and (b) corresponding QDC spectrum.

illustrated in figure 4.5(a). The separation distance between two neighbouring peaks corresponds to p photoelectrons.

The amplification of the primary photoelectrons in the photomultiplier and the digitisation of the resulting charge by the QDC introduce a conversion factor Q between number the of detected photons and the digitiser signal. The peak separation correspondingly becomes $p \cdot Q$ (as shown in figure 4.5(b)). The combination of photomultiplier gain and QDC resolution should be chosen such that the entire dynamic range of the QDC is used, to ensure that the spectrum is spread out enough that each peak extends over a multiple QDC bins. For example for a maximum of 40 peaks and a 12 bit (4096 bin) QDC, one would chose the gain such that the peak separation $p \cdot Q \lesssim 100$ bins, in which case even the first peak would have a width > 10 bins, leaving sufficient degrees of freedom to fit its mean and width.
While noise contributions from the QDC are negligible[32, 33], statistical fluctuations in the amplification process have to be considered significant (see section 7.1). With the added uncertainty of $\Delta g/g$ on the gain, the width increases to

$$\sigma = Q \cdot \sqrt{i_{\text{C.e.}} \cdot p + (i_{\text{C.e.}} \cdot p \cdot \frac{\Delta g}{g}/Q)^2}. \tag{4.3}$$

To resolve individual peaks, the separation should be larger than the peak width, leading to a requirement of $p \cdot Q > \text{FWHM} = 2.35 \cdot \sigma$. Consequently, for a detector configuration to be considered promising towards achieving "self-calibration" for a detector channel with $N_{\text{C.e.}}$ Compton electrons, the number of detected photons per electron needs to fulfil

$$p > \frac{N_{\text{C.e.}}}{\frac{1}{2.35^2} - (N_{\text{C.e.}} \cdot \frac{\Delta g}{g}/Q)^2}. \tag{4.4}$$

Quartz as detector material

To realise a detector system that fulfils the condition in equation (4.4), there are two possible approaches: reducing the number of Compton electrons by building smaller channels for the polarimeter, or increasing the number of photoelectrons per Compton electron.

The Frank-Tamm formula (equation (4.1)) explains why using quartz as a Cherenkov material promises to achieve the latter: The refractive index of quartz (or, more specifically, its non-crystalline form *fused silica*) is much higher than that of gases used in designs like the gas Cherenkov detector described in section section 4.2.1. This leads to a much higher light yield according to the Frank-Tamm formula: For the detector option using perfluorobutane gas as Cherenkov material, the refractive index is 1.00137 at 404.7 nm[30]. At the same wavelength, the refractive index for fused silica is 1.46961[34]. Using $\beta = 1$ for relativistic particles, this would translate into an approximately 200 times higher light yield when quartz is used instead of perfluorobutane for an otherwise unchanged setup.

Such a considerable increase in light yield looks promising in regard to fulfilling equation (4.4) and thus achieving single-peak resolution.
Further implications of the high refractive index are a Cherenkov angle of ≈47° and a reduced Cherenkov threshold:

$$E_{thr} = \frac{1}{\sqrt{1 - \frac{1}{n^2}}} mc^2 \approx 0.9\,\text{MeV}. \tag{4.5}$$

The low threshold could make the use of quartz as a Cherenkov material challenging in the background conditions at the downstream polarimeter. In the clean environment of the upstream polarimeter, this is not expected to pose a problem.

Therefore, a detailed investigation of a quartz detector as an alternate upstream polarimeter detector is presented in the following chapters. In chapter 5, simulation studies to find a suitable detector geometry are presented. The construction and testbeam operation of a prototype based on these studies is described in chapter 6. Chapter 7 discusses the impact of the results on the applicability of the detector concept at the ILC.

5

Design studies

This chapter describes the simulation studies on which the design of a quartz prototype detector was based. The goal of these studies was to find a configuration with sufficient photon yield, i.e. fulfilling equation (4.4), to meet the requirements outlined in section 4.2.2. For example for a setup with a maximum of 30 Compton electrons per channel and a constant noise level of 1 % (0.1 %) for the gain, at least 330 (170) detected photons per Compton electron would be required.
Another purpose of the developed simulation framework is the comparison to data taken with the prototype detector during a testbeam campaign.

5.1 GEANT4 simulation framework

Different detector layouts were studied using the GEANT4 Monte Carlo framework[35, 36]. The main elements of the simulated setup are:

- quartz blocks with adjustable side lengths,
- surrounded by a thin layer of air and/or aluminium foil,
- a photomultiplier, consisting of the entrance window and the photocathode, which serves as sensitive detector in the simulation,
- a 1 mm thick layer optical grease between one end of the quartz and the photomultiplier window.

Every second quartz block is flipped with respect to its neighbour, to provide more space for readout electronics. This geometry is illustrated in figure 5.1.

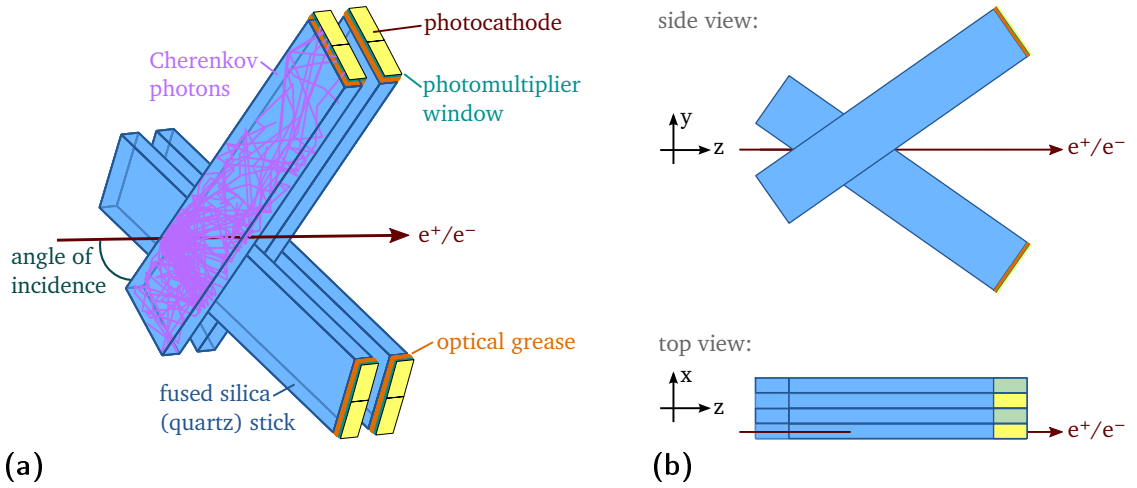

Figure 5.1: Sketch of the simulated geometry. The left side (a) shows some components of the simulation, in addition demonstrating the added space for electronics due to the rotation of every second quartz block. For a better overview, on the right side (b) the same geometry is depicted in side- and top-view.

To evaluate the detector response, electrons are shot through the quartz bars and produce Cherenkov light. Both a pointlike electron beam as well as a beam profile with a Gaussian spread σ_x, σ_y have been implemented. The detector channels can be rotated with respect to the global coordinate system, defined as in figure 5.1, so that the angle between quartz bar and incident electron varies.

5.1.1 Optical photons

Inside GEANT4, the produced Cherenkov photons are treated as “optical“ photons. All the relevant processes to simulate the behaviour of the photons have been switched on: the radiation of Cherenkov light, absorption according to the absorption length of the relevant material, Rayleigh scattering, and boundary processes at the surface between two different media.

To simulate the behaviour inside the detector material and especially at the boundary between two media, their optical properties such as refractive index and attenuation length have to be provided. For the design studies, the refractive index and absorption

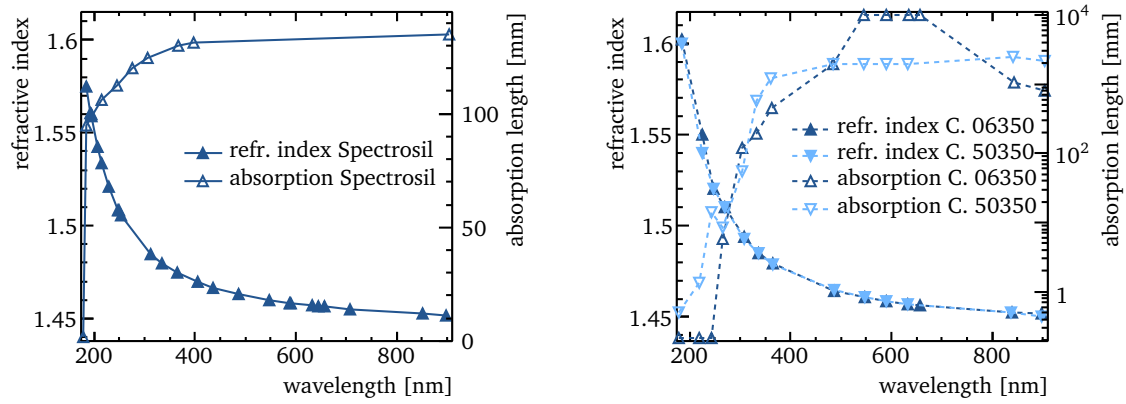

Figure 5.2: Optical properties as implemented in the simulation. The left graphs (a) shows the refractive index (filled markers / left y-axis) and absorption length (open markers / right y-axis) for Spectrosil® 2000, the right graphs (b) for two different Cargille fused silica matching liquids. Between the given values shown by the graph markers, GEANT4 performs a linear interpolation.

length of Spectrosil® 2000[37] have been implemented as detector material. For the optical grease, the refractive index and absorption length of Cargille[I] fused silica matching liquid code 06350[38] and 50350[39] were used. Figure 5.2 shows these optical properties for various photon wavelengths.

To simulate the photon behaviour at the boundaries between the different materials, different options are available in GEANT4. Two cases have to be distinguished: surface boundaries between two dielectric materials, and boundaries between a dielectric material and a metal.

When an optical photon reaches the boundary between dielectric materials, it will be total internally reflected, refracted or reflected, depending on wavelength, angle of incidence, and the refractive indices of the two materials involved. At the boundary between a dielectric material and a metal, the photon is either reflected back into the dielectric or absorbed in the metal.

In addition to the optical properties, the mechanical structure of the surfaces plays a role in the determination of the photons actions at the boundary, especially the surface

[I]Cargille Laboratories, 55 Commerce Rd., Cedar Grove, NJ 07009, USA

roughness. For the simulation of a smooth surface without any surface roughness, providing the refractive index of the two materials on either side of the boundary is enough. GEANT4 uses these to calculate the reflection and refraction probability from Snell's Law.

A more realistic approach is the additional consideration of surface roughness for the materials at the boundary. In the default model of GEANT4, the GLISUR model, a surface can be either *polished* or *ground*. A more detailed description of the surface structure is possible for dielectric-dielectric boundaries if the UNIFIED model[40] of GEANT4 is used. In that case, the surfaces are replaced with surfaces consisting of *microfacets*, as illustrated in figure 5.3(a). When an optical photon reaches the boundary surface, the reflection probability for the photon and the reflection angle are calculated using the angle of incidence of the photon with respect to this microfacet. The distribution of these microfacets is described by an angle α. The microfacet normals around the average surface normal are distributed according to a Gaussian with standard deviation σ_α. Every time a reflection occurs, a microfacet orientation is randomly selected from the distribution, and the direction of the reflected photon

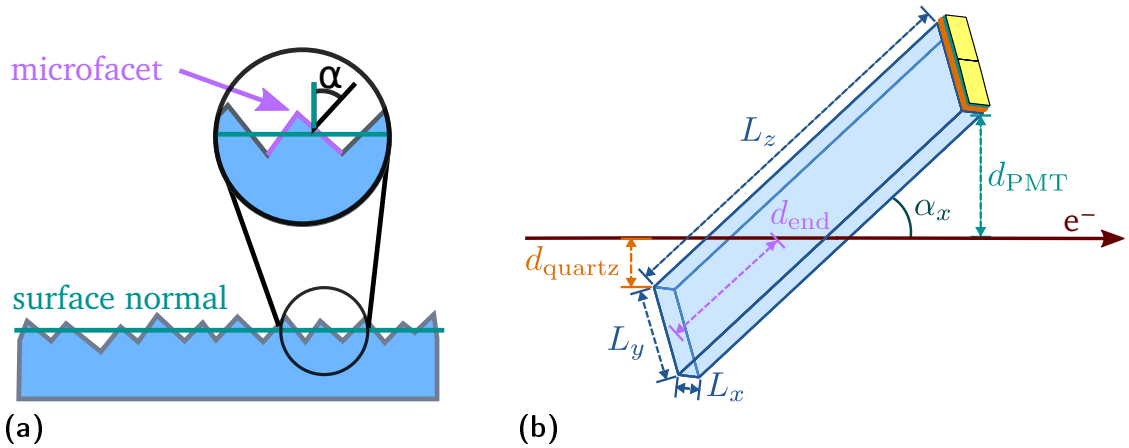

Figure 5.3: (a) A surface made up of microfacets. The zoom-in at the top illustrates the meaning of the microfacet angle. (b) Geometrical parameters varied in the design studies: the channel dimensions width L_x, height L_y, length L_z; the incidence angle α_x; as well as the space between quartz and electrons d_{quartz}, between photomultiplier and electrons and photomultiplier d_{PMT}, and the distance between the end of the channel and the point where the electron crosses the detector axis d_{end}.

calculated based on that microfacets orientation. The effects of different values of surface configurations will be investigated in section 5.3.2.

5.2 Geometry studies

After the basic detector components had been implemented in a simulation framework, various geometrical properties were varied to maximise the photon yield. Once an optimised geometry is found, the predicted light yield can be compared to the requirements for reaching a self-calibrating setup as described in section 4.2.2.

The main impact on the number of photons reaching the photodetector surface (called "photon hits" in the following) is expected from parameters which change the path of the incident electron in the quartz bar, along which the Cherenkov light is produced. These are the height of the quartz bar as well as the angle between the quartz bar and the incident electron (see sections 5.2.2 and 5.2.3). The length and width of the quartz bar does not alter the amount of produced Cherenkov light, but the path the photons travel to the photodetector (sections 5.2.1 and 5.2.4). The distance between one end of the quartz bar and the point where the electron crosses the centre of the quartz can also adjusted. Figure 5.3(b) shows the geometrical parameters discussed in the following sections.

Further effects on the photon yield can be expected from the use of different wrapping or surface options (section 5.3.2). Finally, the fraction of photons that are successfully detected after reaching the photodetector is influenced by to the optical properties of the materials used in the construction of the detector and the efficiency of the employed photodetector types, which will be studied in section 5.3.1.

Unless otherwise stated, all studies below are based on simulations with 10 000 single electron events, for unpolished quartz bars with width $L_x = 5.0\,\text{mm}$, height $L_y = 18.0\,\text{mm}$, length $L_z = 100.0\,\text{mm}$, with 3.0 GeV electrons crossing the detector axis $d_{\text{end}} = 30\,\text{mm}$ from the channel end under an incidence angle of $\alpha_x = 45°$. The simulated quartz bars are wrapped in aluminium foil with a thickness of 0.01 mm,

with a 0.001 mm thin layer of air in between, and coupled to the photocathode with Cargille 50350.

5.2.1 Channel width

The width L_x of the detector channel has no influence on the path length of the electron inside the detector and therefore does not affect the amount of light produced. It does however alter the path of the Cherenkov photons on their way to the photodetector:

In the production of the Cherenkov light, the photons are emitted in a cone around the passing electron. This means that a part of the photons will be emitted such that they are reflected off the channel side walls parallel to the y-z-plane. If the channel width is increased, the number of reflections the photon will have to undergo before reaching the detector is reduced. Every time a photon reaches the channel boundary, there is the probability that it will leave the quartz instead of being reflected back. Therefore, fewer required reflections will lead to a higher probability of the photon arriving at the photodetector.

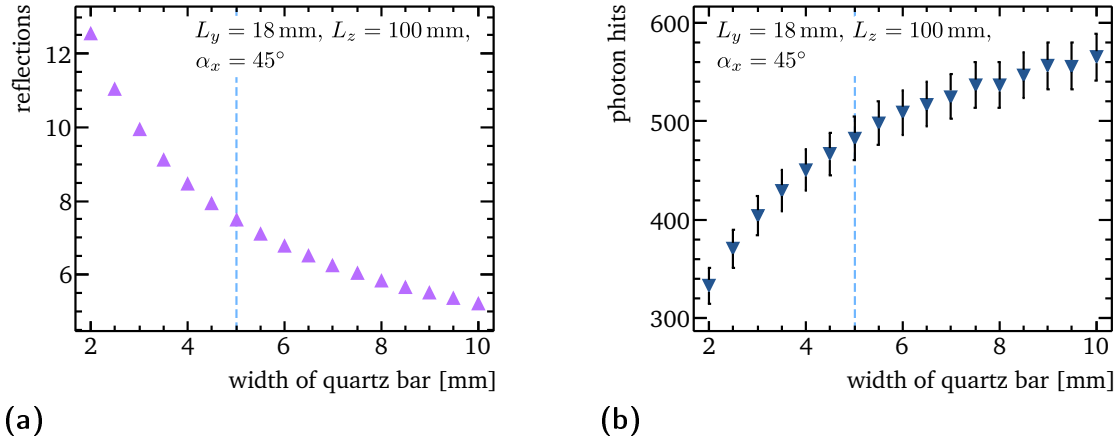

Figure 5.4: Influence of the channel width on (a) the number of reflections a photon undergoes before detection and (b) the measurable light. The dashed blue lines indicate the width used for the prototype detector described in chapter 6.

The mean number of reflections before reaching the photodetector, and the number of photon hits, i.e. the number of photons absorbed on the photodetector mounted on the upper end of the channel are illustrated in figure 5.4 for channel widths in the range 2.0 mm to 10.0 mm.

Even so, the optimal detector configuration is not the one with the largest width, as the photon yield plotted in figure 5.4(b) might suggest. The relevant criterion for reaching the criteria given in section 4.2.2 is the relation between the number of detected photons compared to the number of Compton electrons in a detector channel. Decreasing the channel width by a factor of two from 10.0 mm to 5.0 mm reduces the number of Compton electrons per polarimeter channel by the same order, while the light yield is merely reduced to 85 %. Therefore, a width of 5.0 mm was chosen for the prototype detector discussed in section 6.1.

5.2.2 Channel height

The path length of the electron crossing the quartz channel is proportional to the channel height L_y. The amount of produced light increases accordingly. In addition to this, higher channels also mean fewer reflections of the produced photons along their way, which will also contribute to a higher number of photons reaching the photodetector.

To study the effect of the channel height, it was varied in the range 10.0 mm to 100.0 mm. Figure 5.5 shows the mean number of reflections the photons undertake before reaching the photodetector, as well as the number of photon hits for the different simulated channel heights. The kink at $L_y = 30\,\text{mm}$ is due to the fact that the distance between the end of the channel and the point where the electron crosses the detector axis was set to $d_{\text{end}} = 30\,\text{mm}$. For an angle of $\alpha_x = 45°$, this means that for all heights larger than 30 mm, the electron enters through the base of the detector channel instead of through the side, so that the light production path does not increase as much as for length below 30 mm.

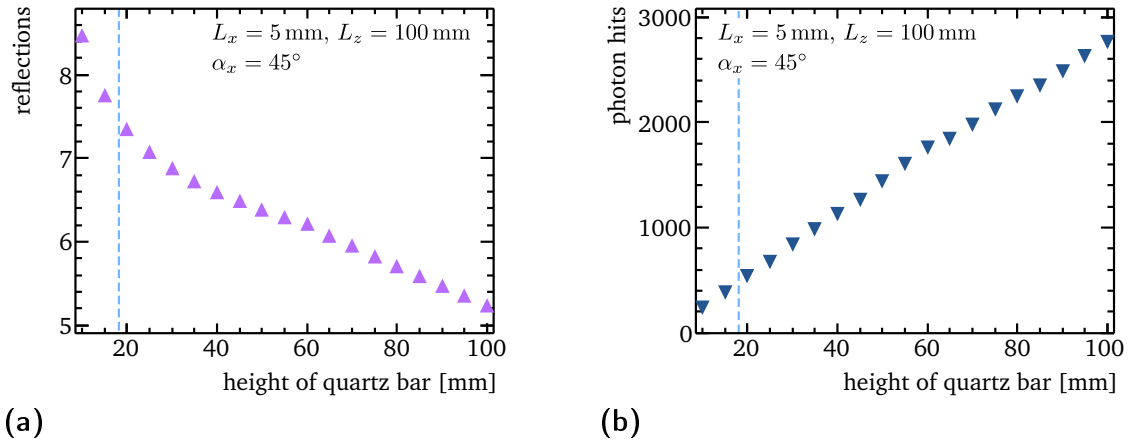

Figure 5.5: Influence of the channel height on (a) the number of reflections a photon undergoes before detection and (b) the measurable light. The dashed blue lines indicate the height used for the prototype detector described in chapter 6.

For the construction of the prototype detector, a height of 18 mm was chosen, mainly with regard to the photodetector options available at the time of construction (see section 6.1.1).

5.2.3 Incidence angle

Like the height of the detector, the incidence angle α_x of the electron also changes the path length of the electron crossing the quartz channel for light production. The path length of the electron and therefore the number of produced photons changes like $1/\sin(\alpha_x)$ with the angle.

An additional impact on the number of photons is due to the fact that for angles close to the Cherenkov angle, a larger fraction of the photons can reach the detector without being reflected on the narrow side faces. This is illustrated in figure 5.6. Since in the simulated configuration with narrow channels of $L_x = 5.0\,\mathrm{mm}$ most of the reflections happen on the other side faces, the effect on the number of reflections before reaching the photodetector is small, but still visible. The resulting impact of the incidence angle α_x on the number of reflections and on the photon hits for angles in the range 30.0° to 60.0° is shown in figure 5.7(b).

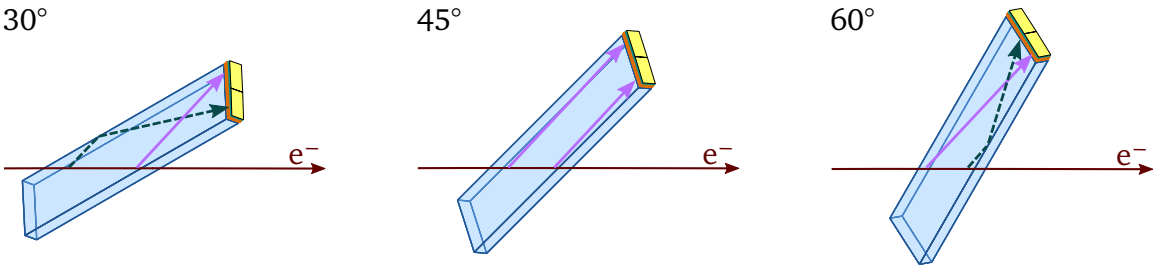

Figure 5.6: Effect of the incidence angle of the electron on the photon path. Two example photons are sketched for $\alpha_x = 30°$, $\alpha_x = 45°$ and $\alpha_x = 60°$ respectively. For angles close to the Cherenkov angle, as depicted in the centre, more photons can reach the photodetector without reflections on the narrow side faces becoming necessary.

As already indicated by figure 5.6, the incidence angle of the electron has an influence on the spatial distribution of the light reaching the photodetector. This is illustrated in figure 5.8. The distribution is the most uniform for angles close to the Cherenkov angle, whereas for other angles certain areas of the photodetector surface are hit by more light than others. This effect could possibly be exploited for angular alignment of the detector by using a photodetector with multiple anodes per quartz channel.

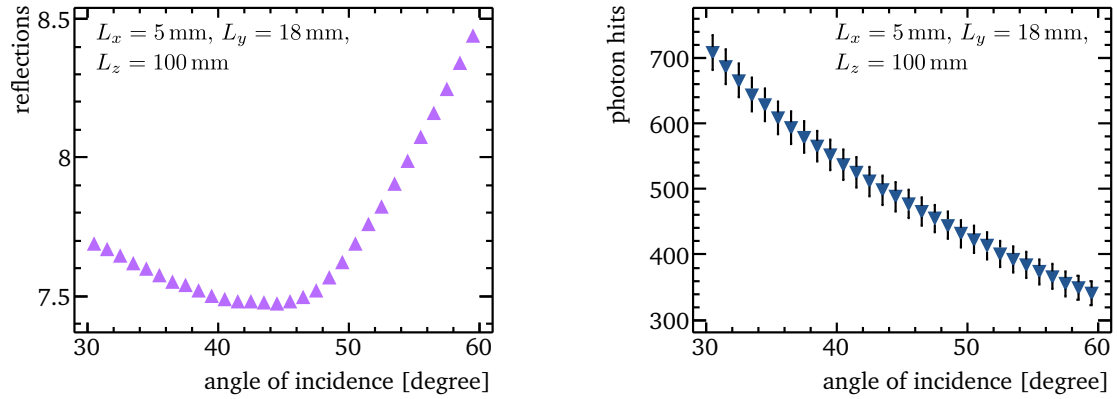

Figure 5.7: Influence of the incidence angle of the electron on (a) the number of reflections a photon undergoes before detection and (b) the measurable light.

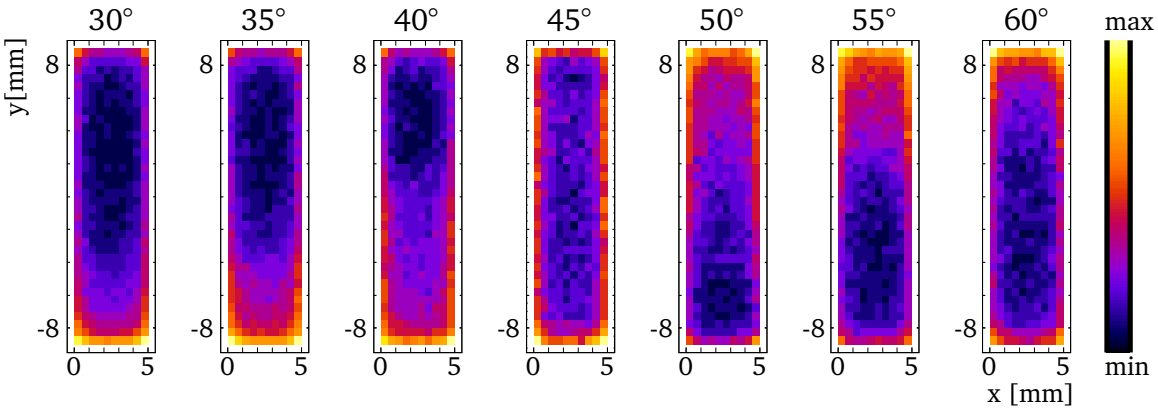

Figure 5.8: Light distribution on the photocathode for different incidence angles of the electron. The position on the photocathode surface is coloured according to the relative light concentration: the regions with most light for each angle are shown in yellow, with a colour gradient to the regions with the least light in dark blue.

5.2.4 Channel length

The channel length L_z has no influence on the path length of the electron inside the quartz. The amount of created light stays the same for longer channels. On the other hand, the distance between the point where the photons are produced and their detection at the end of the quartz bar increases. This means that more reflections are necessary before the photodetector is reached.
The longer light path also causes more photons to be absorbed inside the quartz before reaching the photodetector.

The resulting impact of the channel length on the number of reflections and the number of photons hits is shown in figure 5.9 for different channel lengths in the range 50.0 mm to 300.0 mm.

5.2.5 Combined geometry optimisation

While Figure 5.9(b) indicates that the channel length should be as short as possible, regardless of the other detector dimensions, this changes if another point is considered: Longer channels have the advantage of moving the photomultiplier further from the

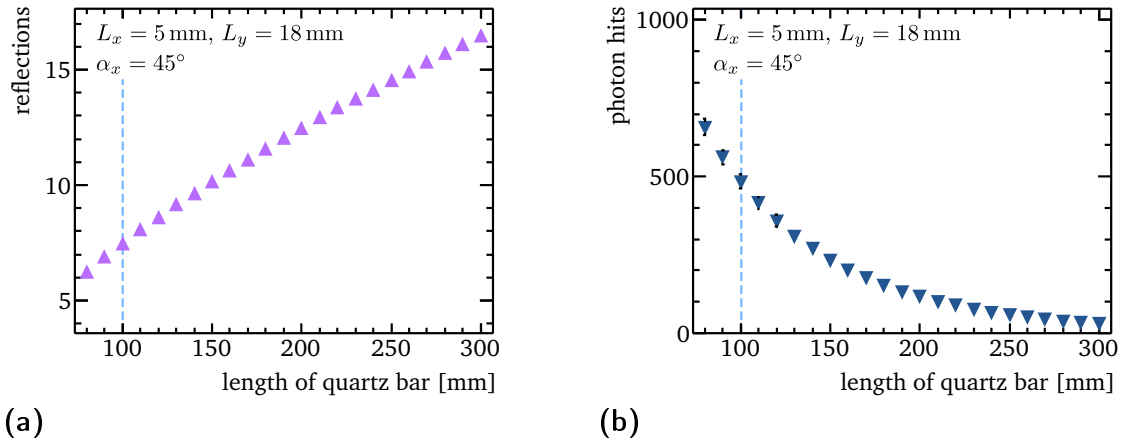

Figure 5.9: Influence of the channel length on (a) the number of reflections a photon undergoes before detection and (b) the measurable light. The dashed blue lines indicate the length used for the prototype detector described in chapter 6.

Compton electrons and thereby protecting the photodetectors from contact with high energetic particles.

To take this into account, another set of geometries was simulated. This time the channel height and electron the entrance point were varied along with the length, such that the space between the lower end of the quartz and the electron plane stayed constant at $d_{\text{quartz}} = 10.0\,\text{mm}$ and the shortest distance between the electrons and the photomultiplier was $d_{\text{PMT}} = 30.0\,\text{mm}$. This translates into a channel height L_y of

$$L_y = \frac{2 \cdot L_z \cdot \sin(\alpha_x) - d_{\text{quartz}} - d_{\text{PMT}}}{2 \cdot \cos(\alpha_x)} \tag{5.1}$$

and a distance d_{end} between the end of the detector channel and the electron crossing of the detector axis of

$$d_{\text{end}} = \frac{d_{\text{quartz}} + L_y \cdot \cos(\alpha_x)}{\sin(\alpha_x)} \tag{5.2}$$

for each simulated channel length L_z and incidence angle α_x. The results for channel lengths in the range 50.0 mm to 300.0 mm and angles in the range 30.0° to 60.0° are displayed in figure 5.10.

While the is a general trend that the geometries fulfilling equations (5.1) and (5.2) favour larger angles and lengths, there is actually a point after which the achievable

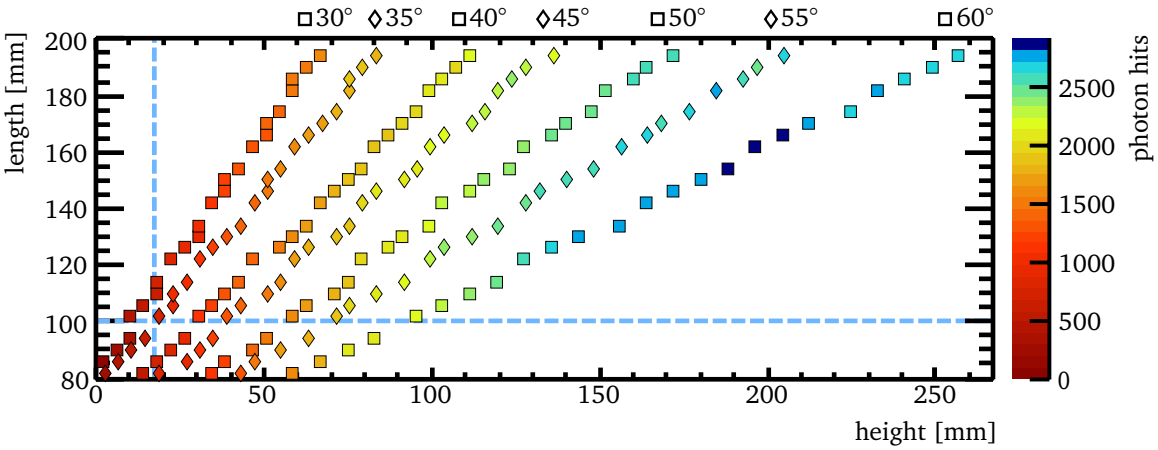

Figure 5.10: Photon hits for different quartz lengths, heights and angles relative to the electron chosen such that equations (5.1) and (5.2) are fulfilled. The dashed blue lines indicate the length and height used for the prototype detector described in chapter 6.

light yield decreases again. The best photon yield of ∼3000 photons is achieved for $\alpha_x = 60.0°$ and $L_z = 160.0\,\text{mm}$, which allows a channel height of $L_y = 197.2\,\text{mm}$ while keeping the chosen safety margin between incoming electrons and readout electronics.

A mechanical setup with such nearly square-shaped channels rather than elongated ones might prove challenging to design. In particular, covering the readout face of high but narrow with conventional photomultiplier tubes to detect the Cherenkov photons does not seem reasonable with the photomultiplier geometries currently available on the market. Silicon photodetectors might be an option to address this.

In any case, other channel dimensions with less extreme aspect ratios also exist that offer a photon yield on the order of ∼1500 to ∼2000 photons and would be more straightforward to implement. Table 5.1 lists some of these geometries, along with the configuration that showed the best light yield, and that chosen for the construction of a prototype detector.

For the prototype detector, smaller dimensions of $L_y = 18.0\,\text{mm}$ and $L_z = 100.0\,\text{mm}$ were chosen, despite the prediction of less (∼600) photon hits. This choice was partly made to match the dimensions of the available photodetectors (see section 6.1.1), but

also to maintain the angular flexibility to scan the full range from 30.0° to 60.0° to confirm the incidence angle's effect on the light distributions found in section 5.2.3.

5.3 Photon detection

To study the maximum achievable photon yield independent of technology choices, the detection efficiency for photons reaching the photodetector was assumed to be 100 % in the previous sections. However, most common photodetectors have a detection efficiency well below 100 %. A more realistic estimate of the photon yield which could be achieved will therefore have to take the characteristics of the photodetector into account.

The amount of measurable light can be further influenced by the choice of the other materials used in the detector, such as the type of optical grease or the surface finish of the quartz bars. These also have to be optimised in addition to the geometrical considerations in the previous sections.

5.3.1 Photodetector efficiency

One option for the photodetector is a photomultiplier tube (PMT) with good sensitivity in the UV range, where the intensity of the produced Cherenkov light is the highest.

photon hits	L_z [mm]	L_y [mm]	α_x	photon hits	L_z [mm]	L_y [mm]	α_x
∼600	100	18.0	45°		90	75.8	60°
	85	51.6	55°	∼2000	100	73.0	55°
∼1500	110	53.4	45°		135	78.4	45°
	125	52.6	40°	∼3000	160	197.2	60°

Table 5.1: Photon hits for selected combinations of quartz lengths, heights and angles relative to the electron chosen such that equations (5.1) and (5.2) are fulfilled. The first entries correspond to the dimensions chosen for the prototype detector.

The quantum efficiency of a photomultiplier, i.e. how well it is suited to detect light of a certain wavelength, depends on the materials used for the entrance window and the photocathode.

Figure 5.11(a) shows the quantum efficiencies for two Hamamatsu[II] photomultipliers with “UV glass“ windows and a bialkali (R7600U-03) or multialkali (R7600U-04) photocathode. How this quantum efficiency affects the number of photons that are actually detected after hitting the photocathode can be seen in figure 5.11(b). For comparison, figure 5.11(b) also shows the effects of absorption inside the different materials used in the detector assembly. Despite the fact that layer of grease is only 1 mm thick, the UV component of the Cherenkov light is severely affected by its short absorption length. This clearly indicates that while the refractive index of the Cargille optical grease matches that of fused silica quite well, it might be useful to investigate other optical greases with higher transmission in the UV range.

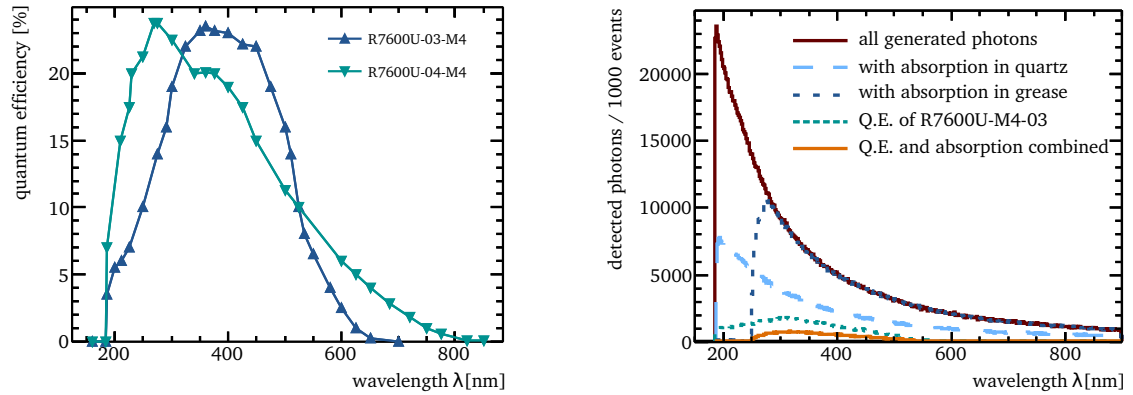

Figure 5.11: Effect of photomultiplier choice: the left plot (a) shows the quantum efficiencies of two UV sensitive photomultiplier tubes[41]. On the right (b), the wavelength spectrum of the Cherenkov photons and the effects of absorption inside the detector and the different quantum efficiencies is shown.

[II]Hamamatsu Photonics K.K. 314-5, Shimokanzo, Iwata City, Shizuoka Pref., 438-0193, Japan

5.3.2 Surface properties

To address the question of what kind of channel surface would be best for reaching a high light yield, different options were studied: an aluminium-coated surface, quartz channels surrounded only by air, and channels wrapped loosely in aluminium foil, implemented as a 0.001 mm thin layer of air surrounded by an aluminium layer of 0.01 mm thickness. In all cases, both rough, e.g. a saw-cut quartz bar, and polished quartz surfaces were simulated. To describe a polished crystal, microfacet angle distribution with a value of $\sigma_\alpha = 1.3°$ was used, for the ground case $\sigma_\alpha = 12°$[42].

Figure 5.12 shows how the detected photon spectrum using the R7600U-03 photomultiplier from figure 5.11(b) changes for these different surface options.

The worst light yield is reached in case of a direct coating with aluminium, when some of the photons are absorbed in the aluminium. While polishing the surface can improve the light yield somewhat, quartz channels surrounded by air would be considerably better. The large difference in refractive index between the quartz and air brings about a critical angle for total internal reflection of $\theta_c \approx 43°$. This means that a large fraction of the photons are reflected at the boundary between quartz and the surrounding air. In case of an unpolished quartz, the microfacets of the surface show a greater variance, and some of photons leave the quartz. In that case, an additional layer of aluminium surrounding the detector can actually offer some improvement,

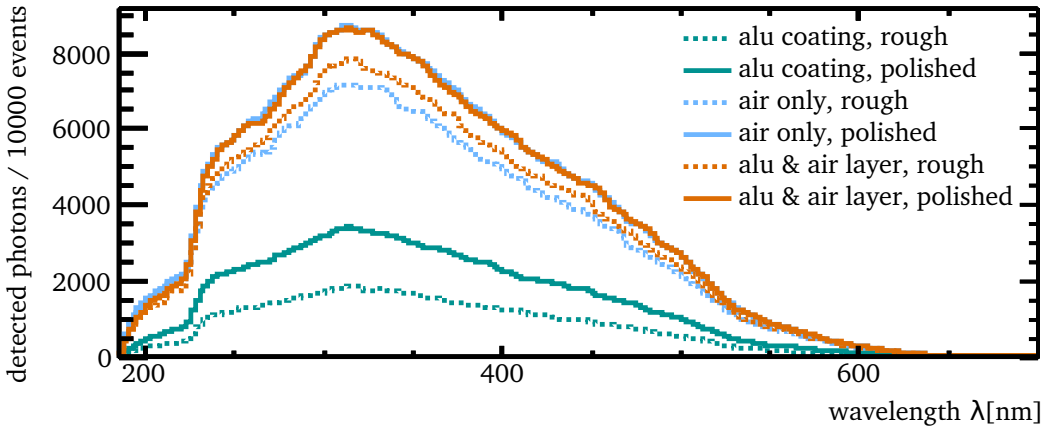

Figure 5.12: Detected photons on the PMT for different surface roughness and wrapping options.

since there is a possibility that these photons will be reflected on the aluminium and re-enter the quartz channel.

5.3.3 Summary of the design studies

The studies discussed in the previous sections show that the amount of produced Cherenkov light is not the only relevant factor for the measurable light yield. The effect of the chosen channel geometry on the path of the photons before detection also has a significant impact.

Considering each parameter on their own, channels with a large height L_y and short length L_z would be preferred, under a shallow angle with respect to the incident electron. However, when further considerations such as a safety distance between electrons and photodetector are taken into account, the maximum number of photons reaching the detector is found for a channel with length $L_z = 160.0\,\text{mm}$ and height $L_y = 197.2\,\text{mm}$, under an incidence angle of $\alpha_x = 60.0°$. For this configuration, more than 3000 photons per Compton electron reaching the photodetector are predicted. Other, potentially more practical geometries with 1500-2000 photons reaching the photodetector per Compton electron were also found (see table 5.1).

In a realistic setup, the quantum efficiency of the photodetectors and absorption in the optical grease used will reduce this number. Table 5.2 lists the predicted light yield for both the geometry with maximum predicted light yield as well as for the prototype

simulated geometry:	optimised		prototype	
	ground	polished	ground	polished
photon hits	3344 ± 58	3876 ± 62	576 ± 24	651 ± 26
detected photons	322 ± 18	373 ± 19	57 ± 7	60 ± 8

Table 5.2: Light yields (with statistical errors) for an optimised geometry and the prototype detector geometry. The values for “photon hits“ refer to the number of photons reaching the readout at the end of the channel, while “detected photons“ are those remaining after absorption in Cargille 50350 optical grease and application of the quantum efficiency of a Hamamatsu R7600U-03 photodetector.

discussed in the next chapter (with a size of 5 mm × 18 mm × 100 mm and for an incidence angle of $\alpha_x = 45.0°$).

There is room for improvement by reconsidering the material choices: The use of photodetectors with higher quantum efficiency, especially in the UV wavelength range, as well as the application of another optical grease with lower absorption in the UV range, would allow to increase the amount of measurable light for a chosen geometry. To a smaller extent, further improvements could be achieved by polishing the quartz surface.

Despite the fact that only $\mathcal{O}(10\,\%)$ of the photons are detected with the material choices considered in this chapter, the predicted yield of ∼60-300 detected photons per incident electron are promising for achieving a single Compton electron resolution as discussed in section 4.2.2. Therefore, the construction of a prototype detector was considered worthwhile and will be discussed in the next chapter.

6

Prototype construction and testbeam operation

The simulation studies in chapter 5 indicate that for a suitable choice of parameters the desired photon yield can be reached. To verify the predictions for the light yield and its angular dependence, a prototype detector with four channels and adjustable incidence angle was built and operated at the DESY II testbeam.

In this chapter, the construction of this prototype, the experimental setup at the testbeam as well as an analysis of the testbeam data are presented.

6.1 Prototype construction

Prior to the construction of the prototype detector, some choices had to be made regarding which photodetectors and which type of quartz to use. The chosen components, the mechanical setup based on these choices, as well as the data acquisition system used with the prototype detector will be discussed in the following.

6.1.1 Photodetectors and materials

Photodetectors

The photodetectors for the quartz prototype were chosen according to two main criteria: high quantum efficiency at short wavelength, where the Cherenkov light intensity

is the highest, and the dimensions of the sensitive area. Combining the wish for narrow channels as discussed in section 4.2.2 with the channel height from section 5.2.5, the ideal photodetector would have a rather long and narrow sensitive area. At the same time, the amount of dead area, e.g. due to the detector's housing, has to be small enough that it does not get interfere with the mounting of the other channels' photodetectors. Multiple anodes per channel would be a further benefit, to test the possibility of alignment using the angular dependence of the light distribution discussed in section 5.2.3.

At the time of the prototype construction, no photomultiplier was readily available on the market that would fit the long and narrow channels, that did not also have a significantly larger housing. For example, Hamamatsu H9530[43] photomultipliers offer eight anodes over an area of 2.5 mm to 21.6 mm, while the full size including the housing is 16 mm to 35 mm. Six of these photomultipliers positioned next to each other could cover the height of 200 mm preferred by the study in section 5.2.5, but only two thirds of the surface would actually be covered by the active area of the photodetectors. In addition, it would not be possible to have channels in close proximity to each other: even using the extra space the rotation of every second quartz

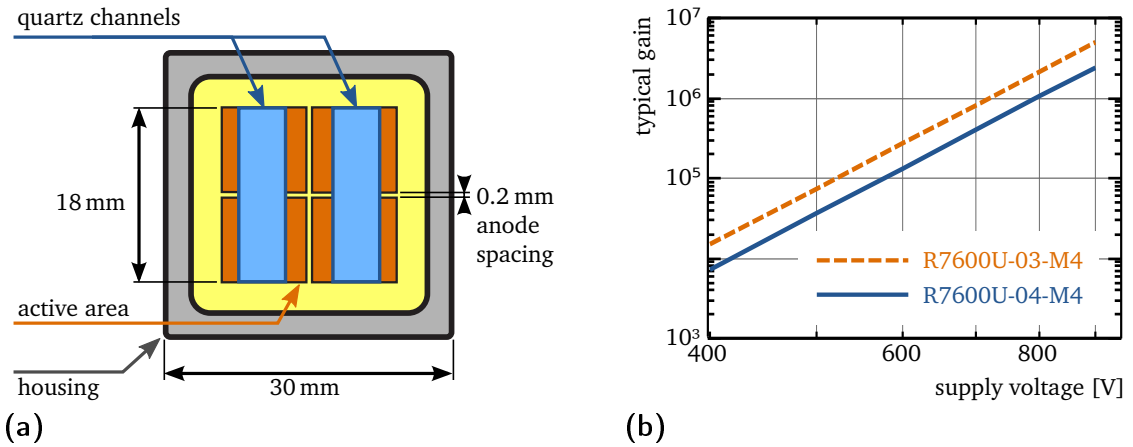

Figure 6.1: Chosen photomultipliers for the quartz prototype. (a) Sketch to illustrate how one photomultiplier with four readout-anodes can be positioned to provide two measurements for two quartz channels each. (b) Typical gain values[41] for the selected photomultipliers.

R7600U type	photo-cathode material	range in nm	peak wavelength in nm	max. dark current in nA	anode crosstalk
03-M4	bialkali	185 to 650	420	5.0	2 %
04-M4	multialkali	185 to 850	400	12.5	2 %

Table 6.1: Characteristics of the photomultipliers R7600U-03-M4 and R7600U-04-M4 used with the quartz prototype[41].

bar provides, the photodetector dimensions would require 5.5 mm spacing between two adjacent channels for 2.5 mm wide channels.

While it would most likely be possible to obtain custom-made photodetectors closer to the desired dimensions, for the prototype detector construction a faster and more cost-effective option was chosen: square photomultipliers with an active area of 18 mm to 18 mm, with a four-anode readout. By placing 5.0 mm wide quartz bars on two anodes each, as illustrated in figure 6.1(a), and staggering this setup with another two rotated channels sharing one multi-anode photomultiplier, a layout with four channels directly side by side becomes feasible.

The prototype detector was operated with two different photomultiplier models with the same dimensions and anode segmentation from Hamamatsu, type R7600U-03-M4 and R7600U-04-M4. Typical values for gain and quantum efficiency are shown in figure 6.1(b) and figure 5.11(a), respectively. Table 6.1 lists some of the main properties of these photomultipliers: While the 03-type photomultipliers use bialkali photocathodes, offering sensitivity from the UV to the visible wavelength range. For the 04-type photomultipliers, multialkali photocathodes are used. A mixture of multiple alkali metals in the cathode material provides a wider sensitive range up to the near infrared. Since the intensity of the emitted Cherenkov light decreases with the wavelength, the contributions from photons in the additionally available range offer only a small advantage compared to the 03-type photomultipliers. On the downside, the dark current for the multialkali cathode type is typically higher than for the bialkali photocathodes. The dark current is the output current that flows in a photomultiplier tube whenever the supply voltage is applied, even when its operated in a completely dark state. It is caused due to several reasons, most prominently leakage currents

between the electrodes inside the photomultiplier or thermionic emission from the cathode. It will show up as a pedestal in the measured QDC signal. To determine the amount of measured light, the QDC output has to be corrected by subtracting the dark current contribution (see section 6.3.1).

Crosstalk between the photomultiplier anodes will blur the distinctions between upper and lower anode of a channel and the second channel sharing the same photomultiplier, and thereby make the observed differences in the light distribution between them somewhat smaller. Both photomultiplier types have the same level of anode crosstalk (2 %). This is small enough that its effect will be neglected in the testbeam data analysis.

Quartz blocks

For the quartz channels, the synthetic fused silica brand Spectrosil® 2000[37] was chosen as the most suitable material. It offers a higher radiation tolerance than other natural or synthetic fused silica brands[44]. The low number of optical impurities and the high transmission in the UV range, where most of the Cherenkov light is produced, are further criteria which were considered. Typical values for these properties are given in tables 6.2 and 6.3.

For a prototype detector, saw-cut quartz blocks were ordered from Heraeus Quarzglas[I]. Instead of a geometry optimised for the maximum light yield, dimensions of

	Al	Ca	Cr	Cu	Fe	K	Li	Mg	Na	Ti	V
in ppb	< 10	< 15	< 1	< 3	< 5	< 10	< 1	< 5	< 10	< 5	< 5

Table 6.2: Upper limits on typical trace element contents in Spectrosil® 2000[45].

λ in nm	193.4	248.4	266
transmission after 10 mm path length	98.5 %	99.5 %	99.9 %

Table 6.3: Internal transmission of Spectrosil® 2000 for UV wavelengths[37, 45], as implemented in the simulation presented in chapter 5.

[I] Heraeus Quarzglas GmbH & Co. KG, Quarzstraße 8, 63450 Hanau, Germany

viscosity in cSt	at 15 °C	at 25 °C	at 35 °C
Cargille 06530	133	80	52
Cargille 50350	31	19	15

Table 6.4: Viscosities of fused silica matching liquids[38, 39].

5 mm × 18 mm × 100 mm were chosen for the quartz blocks to correspond to the active area of the photomultipliers, as explained in section 6.1.1. If the light yield achieved with this setup matches the predictions from the simulation, it will also lend credibility to the simulation's predictions for the other geometries discussed in chapter 5. Figure 6.2(a) shows two of these quartz blocks next to one of the photomultipliers.

Optical grease

The photomultipliers need to be coupled to the quartz bars with some kind of optical grease to limit total reflection at the boundary. As discussed in section 5.3.1, different choices of optical grease should be investigated in the future.

For the first tests with a prototype detector, it was decided to use one of the two fused silica matching liquids used in the simulation studies, mentioned in section 5.1.1. Of these two, Cargille 50350 has a longer mean free path before absorption. However, it also has a lower viscosity than Cargille 06350, as listed in table 6.4. Therefore, Cargille 06350 was chosen for the testbeam campaign. While this will result in a somewhat lower light yield, it also promises more stable conditions when applied on inclined surfaces such as the ends of the quartz channels.

6.1.2 Mechanical setup

A setup with adjustable angle was designed[II] to hold the quartz blocks and photomultipliers in place while at the same time providing the means to test the angular dependence of the light yield. To realise a configuration as described in chapter 5, with every second quartz block flipped with respect to its neighbour, two brackets are

[II]Many thanks to B. Beyer for the technical design and assembly of the setup.

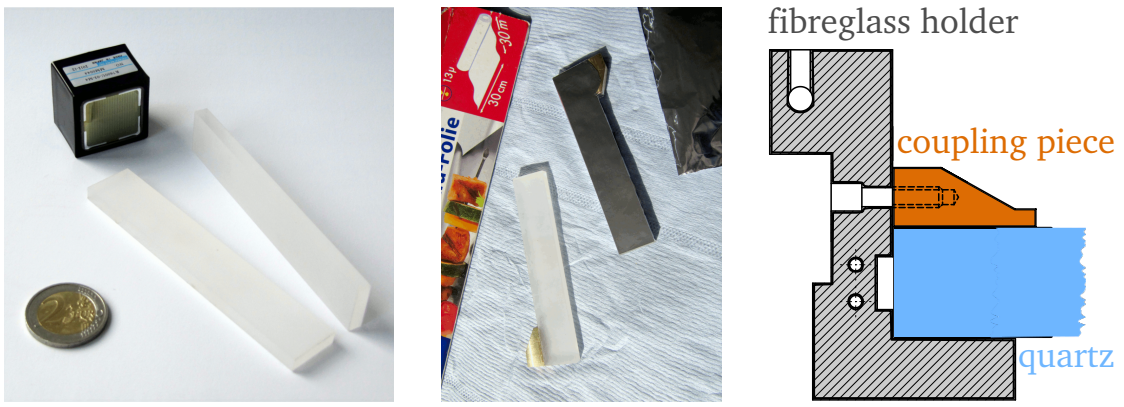

Figure 6.2: Quartz channels for the prototype detector. On the left (a), two quartz blocks and a photomultiplier with a coin for size comparison are displayed. The central photo (b) shows the quartz sticks with the coupling piece glued in place, in the process of being wrapped in aluminium foil. The drawing on the right side (c) illustrates the fixation of the quartz blocks.

connected to a central rotation axis. Each bracket has an upper and a lower cantilever arm - on one bracket, the quartz bars are mounted to the lower cantilever arm, on the other one to the upper arm.

To attach the quartz bars to their cantilever, small brass coupling pieces were glued to the narrow side face at one end of the blocks facing away from the designated beam entry plane. The glue was preferred over other coupling options such as screws to avoid possible cracks or other damages of the quartz blocks. Onto the side facing towards the beam, no brass pieces were glued, to prevent the production of secondary electrons from electromagnetic showers in the metal. The quartz blocks are wrapped in a loose layer of aluminium foil (figure 6.2(b)), then the brass pieces are fixed to fibreglass holders. These are not only connected to the cantilever arm, but also provide additional support for the quartz blocks in the x-y and x-z plane (figure 6.2(c)).

On the bracket's other arm, a mounting is provided for the photomultiplier designated to measure the light produced in the quartz bars of this bracket. The photomultipliers were contacted using the matching socket E7083 by Hamamatsu. The entire setup is fixed onto a base plate, which can be covered by an aluminium housing to shield the

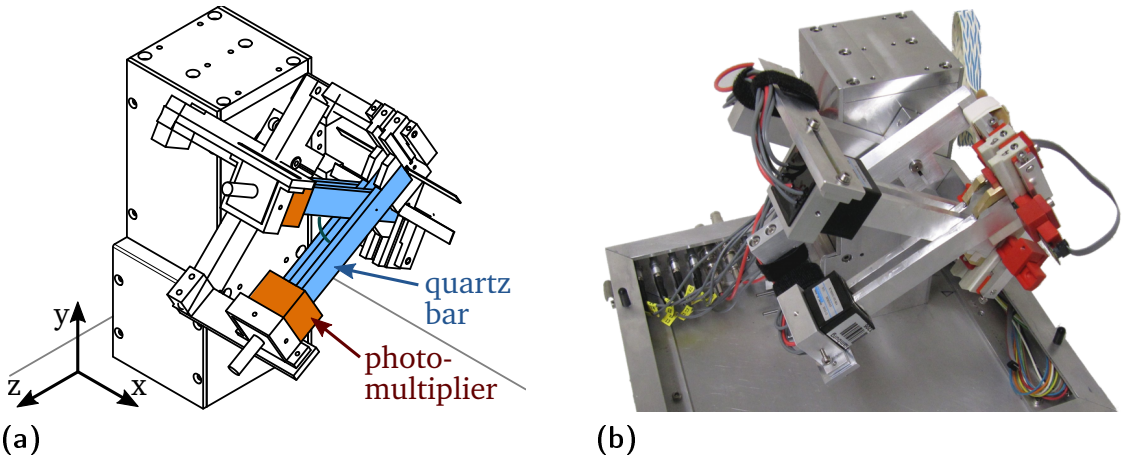

Figure 6.3: Construction of the prototype detector. In the technical drawing (a), the positioning of the four quartz blocks and two photomultipliers used in the prototype setup are marked. (b) Photography of the fully assembled prototype.

detector from ambient light. The full setup (without the aluminium housing) is shown in figure 6.3.

On the channel ends opposite of the photodetector, mountings for circuit boards with UV-LEDs are provided. These LED drivers were developed as the main component for a calibration system for the gas Cherenkov detector[32]. They could be used to test the basic operation of the setup before the testbeam campaign, and possibly also for photodetector calibration in the future.

To control the angle between the two upper and the two lower quartz channels, a Nanotec[III] ST5909 M2608 stepping motor was used. This motor has a base step angle of 0.9°, which was transformed to 0.5° steps by a dedicated gear mechanism contained in the mechanical setup.

6.1.3 Data acquisition and slow control

The movement of the stepping motor is controlled with a Nanotec SMCI33 stepper motor drive with closed loop controller. The connection to the data acquisition (DAQ)

[III]Nanotec Electronic GmbH & Co. KG, Kapellenstr. 6, 85622 Feldkirchen near Munich, Germany

and steering computer is established via a USB cable.

The necessary high voltage for the operation of the photomultiplier is provided by a CAEN[IV] high voltage module V6533 with six channels. The charge signals of the photomultipliers are read out with a 16-channel charge-sensitive analogue-to-digital converter (QDC) of type V965 by CAEN. Both the high voltage module and the QDC communicate via the VME computer bus standard. They are controlled by a CAEN VME controller V2718, which can be connected to the DAQ computer via an optical link.

The digitised photomultiplier signal is available in 12 bit (i.e. 4096 bins) in two resolutions: in the "low range", the QDC has a resolution of 25 fC, resulting in an input range of up to 102.4 pC. For higher charge signals, the "high range" of the QDC has to be used, which has a digitisation resolution of 200 fC and therefore an eight times higher input range up to 819.2 pC.
The digitisation length and cycle are steered by an external gate, which has to be provided to the QDC module.

For the control of the individual components mentioned above, the C++ software framework PolDAQ first mentioned in [46] was used. Based on the work done for [32], it was extended to include the necessary drivers for the stepping motor control and a graphical user interface designed to control and log the settings used throughout the testbeam campaign.

The data from the QDCs is stored in ROOT[47] format. In addition, for each data taking run, an entry with information on the chosen settings and an individual run identification number is stored in an ASCII run list.

6.2 Testbeam operation

The quartz prototype detector was operated in a single electron beam at the DESY testbeam[48], which allowed to test the detector response for single electrons.

[IV] CAEN S.p.A., Via Vetraia 11, 55049 Viareggio (LU), Italy

The main purpose of the testbeam campaign was to test the reliability of the simulation predictions concerning the light yield. In addition, the detector response under different positions and angles should be investigated. As explained in section 4.1, the requirements for the alignment of the polarimeter detector are $\mathcal{O}(0.1\,\text{mm})$ in the horizontal direction, and $\mathcal{O}(1\,\text{mrad})$ on the tilt angle. While the detector alignment at the ILC polarimeter could be monitored by dedicated calibration runs, it would save valuable operation time if alignment information could be extracted from the regular polarimetry data taking. Therefore, the development and test of data-driven alignment methods was another goal of the testbeam campaign.

6.2.1 DESY II

Figure 6.4 shows a schematic overview of the creation of the beam used for the study of the detector prototype: A carbon fibre is inserted into the primary beam of the DESY II synchrotron to produce a bremsstrahlung beam. The photons are then converted to electron/positron pairs by a metal conversion target. A dipole magnet in combination with a collimator allows to pick electrons or positrons with a certain momentum. When the shutter in the beam line is open, the selected particles enter the experimental area through another collimator. The type of conversion target and the magnet current can be specified via controls in the hut next to the experimental area. The testbeam user also has a choice between area collimators with different apertures.

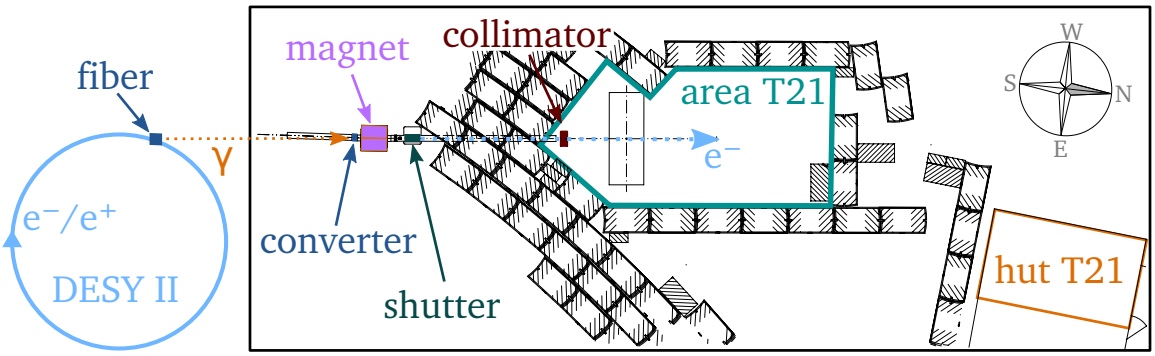

Figure 6.4: Schematic layout of the beam creation and the testbeam area 21.

6.2.2 Experimental setup at the testbeam

The quartz detector prototype was operated for two weeks in testbeam area T21 (22.04. - 05.05.2013). Figure 6.5 shows the area with the main components of the experimental setup. The main components of the setup and the readout chain are also illustrated in figure 6.6.

The quartz detector was placed inside an aluminium box with foam rubber seals to shield it any light not originating from Cherenkov light producing caused by the passage of testbeam electrons through the detector. To ensure a lightproof closure, the joint between box lid and base was additionally covered with back tape. For the second half of the testbeam, a black cloth was added for further background light reduction.

The box with the detector was placed on a base plate movable by two linear precision translation stages, PI[V] M-511 and M-521, which allowed to change the position of the detector in sub-millimetre steps in the horizontal (x) and vertical (y) direction respectively.

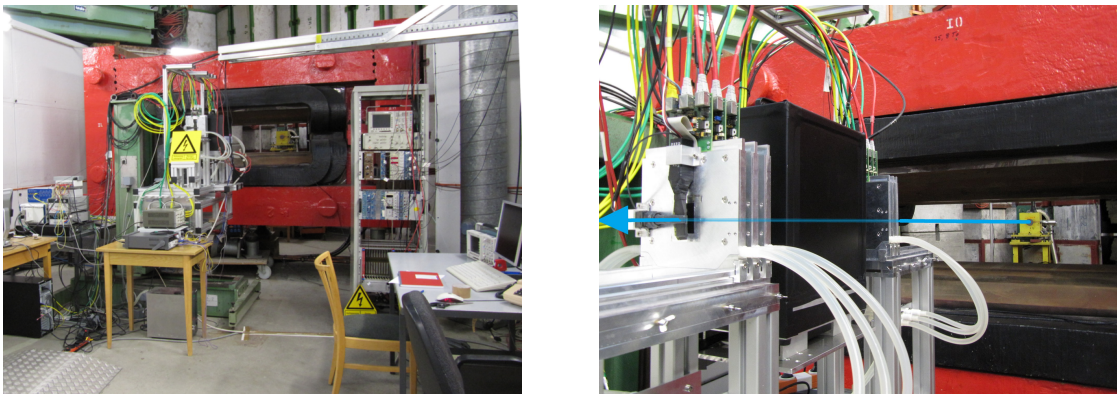

(a) (b)

Figure 6.5: Quartz detector setup at the testbeam. The photo on the left (a) shows the entire testbeam area. On the right(b) a sketch of the beam path is overlaid on a close-up of the light-tight box with the detector inside on the x-y-table and two of the trigger scintillators.

[V]Physik Instrumente (PI) GmbH & Co., Auf der Römerstr. 1, 76228 Karlsruhe, Germany

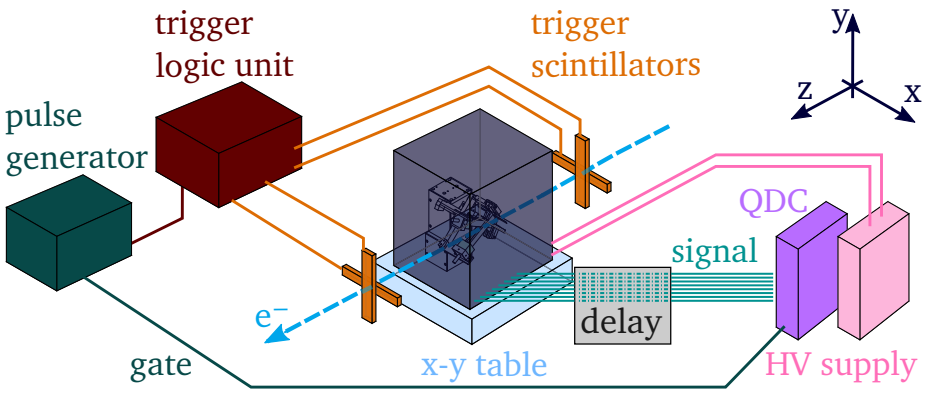

Figure 6.6: Experimental setup at the testbeam. The main components of the setup and the path of the readout signal path are sketched.

To trigger on beam electrons, the trigger scintillators of the EUDET pixel telescope setup[49] were used, requiring signals from both a vertical and horizontal trigger finger before and after the detector box, respectively. The vertical trigger fingers had a width of 20 mm, the horizontal trigger fingers a height of 10 mm, resulting in a 20 cm^2 large trigger window. In case of a four-fold coincidence between the trigger scintillators, the output of the telescope's trigger logic unit[50] was used to start the generation of a gate signal for the QDC.

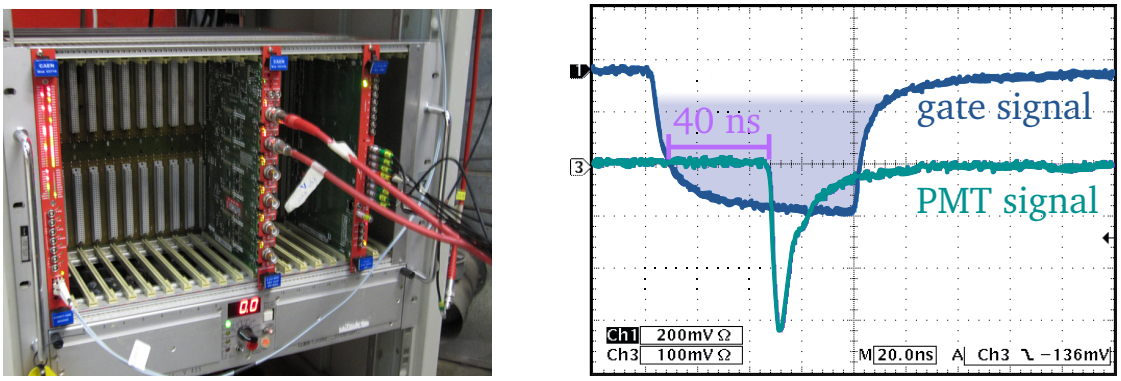

(a) (b)

Figure 6.7: The QDC used to digitise the photomultiplier signals can be seen on the right in (a) next to the high voltage power supply (in the centre of the photo) and their VME controller. The gate signal determining the QDC's measurement cycle and the signal of one of the photomultiplier anodes for one triggered beam event are shown on the right(b).

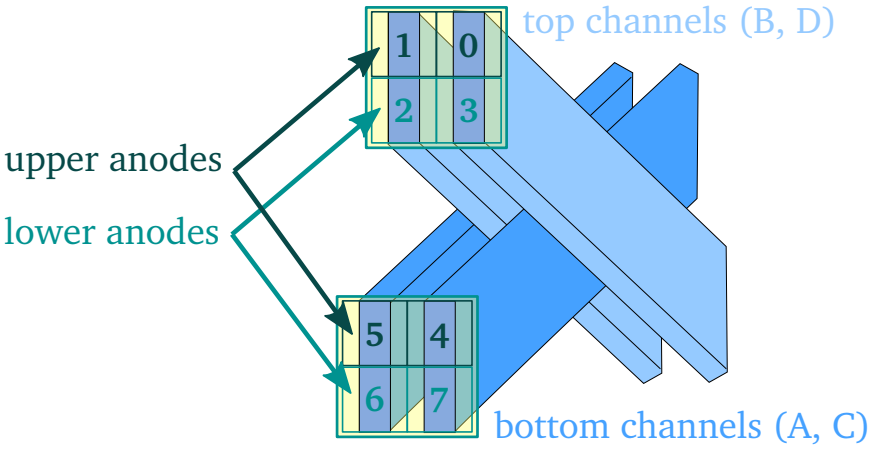

Figure 6.8: Channel names and anode numbering used for the description of the testbeam data.

For the gate generation, during the first two days of data taking, a LeCroy 222 NIM gate generator was used, which was then exchanged against a Hewlett-Packard 8013B pulse generator. A gate width of ≈60 ns was chosen.
The QDC needs some additional time $\mathcal{O}(10\,\text{ns})$ from the begin of the gate signal to the actual start of its measurement cycle. To ensure that the photomultiplier signals arrived inside the gate, a delay of the signal by ≈160 ns was needed. This was realised by using 32 m long readout cables for each channel. The delay was then fine-tuned using the delay settings of the gate generator itself to ensure that the gate signal arrives at the QDC ahead of the photomultiplier signal. The timing of gate signal and a signal from one of the photomultiplier anodes can be seen in figure 6.7(b).

A total number of eight QDC channels was used to digitise the signal from the two four-anode photomultipliers. The conventions for channel naming and anode numbering that will be used in the following sections are illustrated in figure 6.8: The channels are named channel A-D in increasing x-direction. The quartz bars “pointing upwards“ (B, D) are referred to as top channels, the “downwards pointing“ ones (A, C) as bottom channels. The two photomultiplier anodes of each channel are called upper and lower anode respectively, according to their y-position.

During the entire duration of the testbeam campaign, data was taken with 3.75 GeV electrons. As a converter target for the generation of the electrons, a copper foil of 5 mm thickness was chosen. In combination with the area collimator with aperture of

5 mm × 5 mm, which was used for all data taking runs unless stated otherwise, this resulted in a possible data taking frequency of ≈1 kHz to 2 kHz.

6.3 Testbeam data analysis

With the setup described in the previous section, scans of the detector position as well as scans of the incidence angle were performed. At each position, 100 000 events were recorded. In the following, the overall light yield as well as the detector response observed in these scans are discussed.

6.3.1 Pedestal correction

Before the data recorded with the QDC could be analysed, it had to be corrected for the pedestal contribution: an internal device current is constantly present in the QDC, which causes a shift of all entries towards higher bins. Dark current from the photomultipliers leads to a broadening of the pedestal peak.

For each anode, the spectra recorded during the test beam contain events in which the data acquisition was triggered, but no electron entered the respective channel. Therefore, a pedestal peak is present in each channel in addition to the Cherenkov signal. This allows to determine the pedestal position directly from each data set, rather than using separate calibration measurements: For each spectrum, the pedestal peak at the low edge of the spectrum is fitted with a Gaussian to determine the pedestal position. The x-axis of the QDC spectrum is than shifted such that the mean of the fitted Gaussian is at zero QDC bins. Figure 6.9 shows an example for a QDC spectrum before and after pedestal correction.

To exclude events in the analysis of a detector channel where that channel was not hit by the electron beam, a cut threshold was defined based on dedicated dark current measurements (i.e. runs without beam) taken over the course of the testbeam period. It was found that applying a threshold of 15 QDC bins above the QDC pedestal position eliminates at least 99.7 % of the events in any dark current spectrum. For

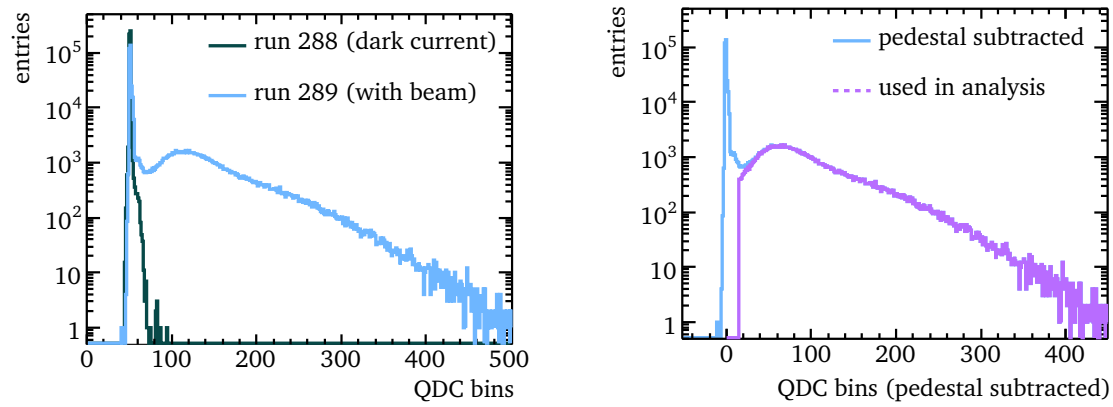

Figure 6.9: Pedestal correction. (a) An example for an uncorrected QDC spectrum is shown in light blue, recorded in anode 5 with the beam centred on channel A and a beam incidence angle of 45°. A dark current spectrum for the same anode is drawn in green. (b) The same QDC spectrum with shifted x-axis to correct for the pedestal contribution. The light blue histogram contains all events, while the violet histogram is made up of only the events used in the analysis, i.e. events in which both anodes of a channel see a signal of at least 15 QDC bins above the pedestal.

the following analyses only events where taken into account in which both anodes of a channel yielded a signal of at least 15 QDC bins above the mean of their respective pedestal.

Another feature visible in the QDC spectra recorded with beam is a small shoulder near the pedestal. The origin of this shoulder is not clear. The same behaviour has been observed by other groups using the same photomultiplier type, who have proposed to explain it by charge multiplication starting at one of the amplification dynodes following the first one[51]. This could occur when an incident UV photon passes the photocathode and is absorbed in one of the dynodes, in which case the preceding dynodes would not contribute to the charge amplification. Additional photoelectrons amplified with a different gain than the photoelectrons from the photocathode would increase fluctuations in the central value of the photomultiplier gain and thus broaden the signal peak. In addition, if the effect from the photons absorbed after the photocathode is not included in the gain and quantum efficiency listed in the datasheet of

the photomultipliers, the observed light yield would be greater than expected from the datasheet values alone.

The part of the spectrum used in the analysis, compared to the spectrum before any cuts, is depicted in figure 6.9(b).

6.3.2 Signal shape

As a first step in comparing the testbeam data to the predictions from the simulation, the shape of the signal is studied. Figure 6.10 shows the QDC signals after pedestal correction for a run where the beam was centred on channel B (anodes 1 and 2) under an angle of 45°. Figure 6.11 shows the number of photon hits per anode for 10 000 events simulation with this configuration.

Two differences strike the eye when comparing these two. The first is the distribution of the signal. While in the simulation the photon hits are nearly exclusively in the channel on which the beam was centred, in the data quite a large number of events show a signal in one of the neighbouring channels, with significantly more light than one would expect from the crosstalk ratio of 2 % between the photodetector anodes.

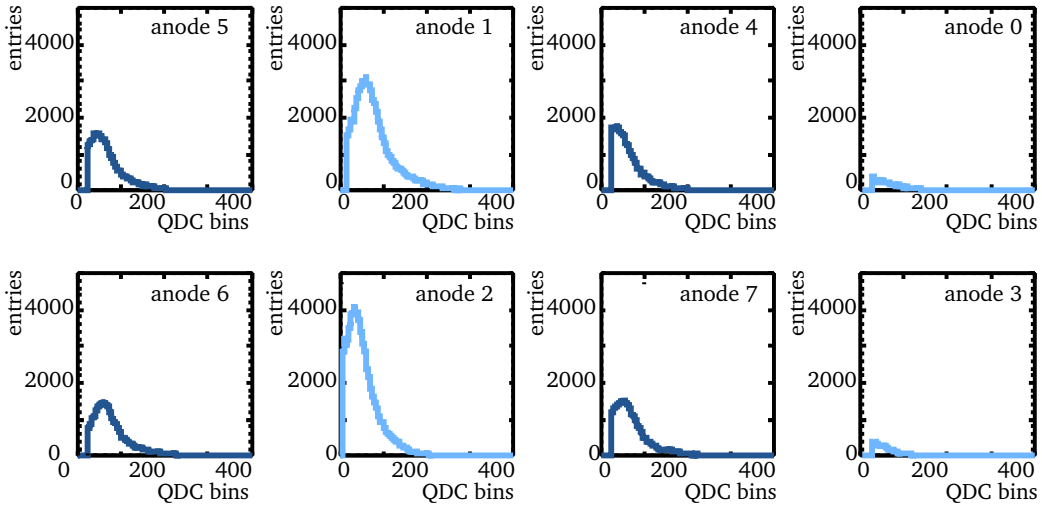

Figure 6.10: Photomultiplier signals of all anodes for a data taking run at 45° with the beam centred on channel B. The cut-off at low QDC bins is due to the pedestal subtraction.

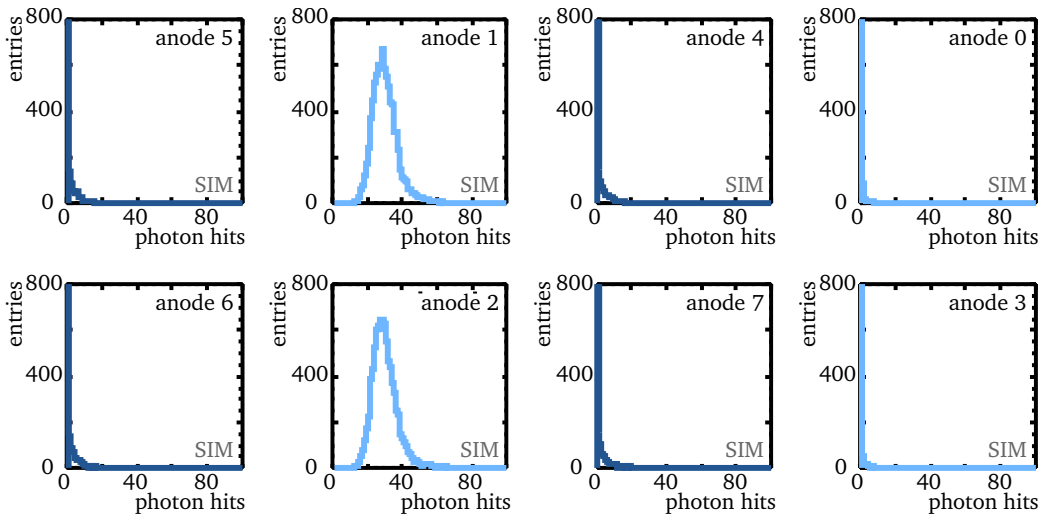

Figure 6.11: Simulated events for the same configuration as in figure 6.10.

This can be explained by the fact that the beam was not pointlike, as assumed for the simulation, but rather featured a beam spot extending over several millimetres. This will be discussed in more detail in section 6.3.4.

The second difference is in the shape of the signal itself. If one uses a Gaussian to describe the shape of the signal, the ratio between the width of that Gaussian and the square root of its mean is $\sigma/\sqrt{mean} \approx 1.3$. In the data, the peak in the QDC signal is a factor $\mathcal{O}(3-4)$ wider than in the simulation ($\sigma/\sqrt{mean} \approx 4.8$) and has a noticeable tail to higher charges, i.e. a larger number of photoelectrons released from the photocathode.

The larger width alone might be explained by unexpectedly high gain fluctuations, e.g. due to the supposed contributions from photoelectrons emitted from one of the dynodes rather than the photocathode, as mentioned in section 6.3.1.
However, an increased gain noise can not account for the large tails. The most likely explanation is the presence of secondary electrons in addition to the main beam electron, which would produce some additional light when they hit one of the quartz channels. It is currently not clear where these stem from. The wall thickness of the light-tight box surrounding the detector is only 4 mm. Implementing this in the simulation does not contribute enough shower electrons to explain the amount of additional light observed. Other possible contributions along the beam line have not been investigated so far. In

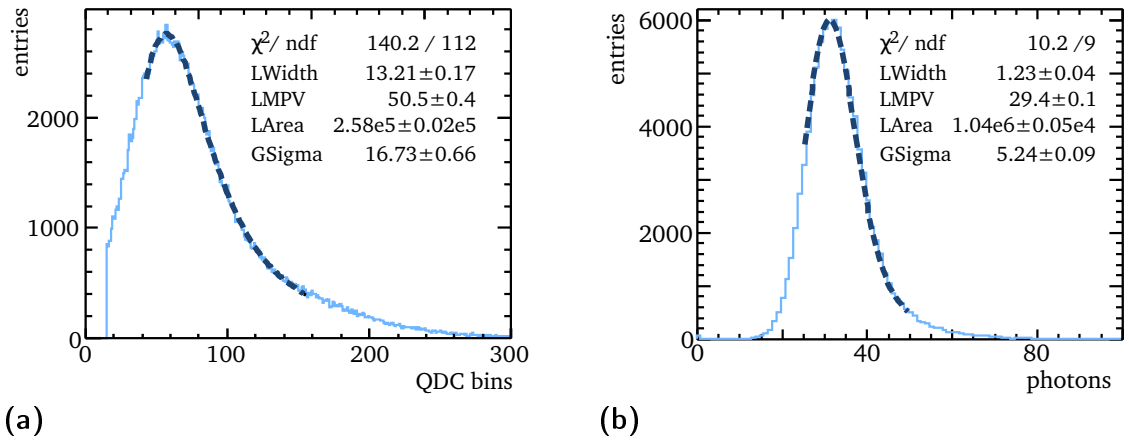

Figure 6.12: Fit of a Landau function convoluted with a Gaussian to the signal for (a) anode 2 in a data taking with the beam centred on channel B, under an incidence angle of 30° and (b) the corresponding simulation.

the future, this should be checked more carefully, possibly with a different electron source.

For now, the effect of the extra electrons, regardless of their origin, was taken into account by fitting the QDC signals with a fit function consisting of a Landau function convoluted with a Gaussian, to account for the tail in the distribution. An example for such a fit can be seen in figure 6.12. The free parameters of the function are the width and most probable value (MPV) of the Landau function, the sigma of the convoluted Gaussian and a normalisation constant for the peak area. Whenever the testbeam data is compared with the simulation, the same fit is applied to the simulation. For the simulation, the width of the Gaussian is dominant, while in the data a comparable width of the Landau part of the fit function is required to describe the large tails.

The most probable value of the fitted Landau function will be used to compare the light yield between data and simulation, while the area parameter is a measure for the number of times a channel was hit by the beam. To illustrate the stability of the fit procedure's outcome, figure 6.13 shows the fitted most probable value for both anodes of a channel for a number of data taking runs at identical beam position over a period of several hours.

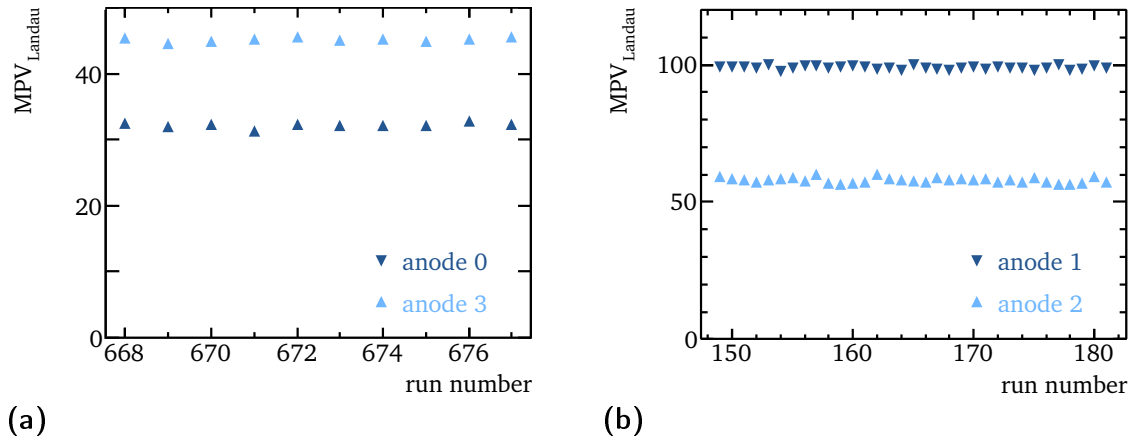

Figure 6.13: Fit results for consecutive measurement runs: (a) anodes 0 and 3 for 10 runs taken over a period of 3.5 hours (beam on channel D, under an angle of 59°) and (b) anodes 1 and 2 for 32 runs taken over a period of 11 hours (beam on channel B, under an angle of 30°). The observed light yield stays constant.

6.3.3 Light yield

Photomultiplier Gain

In order to compare the light yield observed at the testbeam to the predictions from the simulation, the gain of each photomultiplier anode has to be known. The values provided by Hamamatsu are only “typical values“ for the photomultiplier models. According to the datasheets, the gain for the R7600U-03 photomultipliers ($\sim 4.8 \cdot 10^6$) should be twice as high as for the R7600U-04 photomultipliers ($\sim 2.4 \cdot 10^6$). In the data however, no discernible difference between the signal of the two photomultiplier types was found, leading to the suspicion that the datasheet values can not be taken at face value. Therefore, dedicated measurements to determine the actual values were performed. A separate test setup was used: inside a light-tight box, a small amount of UV light was produced with one of the LED drivers described in section 6.1.2. The amount of light was further reduced by a filter mounted in front of the photocathode. A more detailed description of this setup can be found in [32].

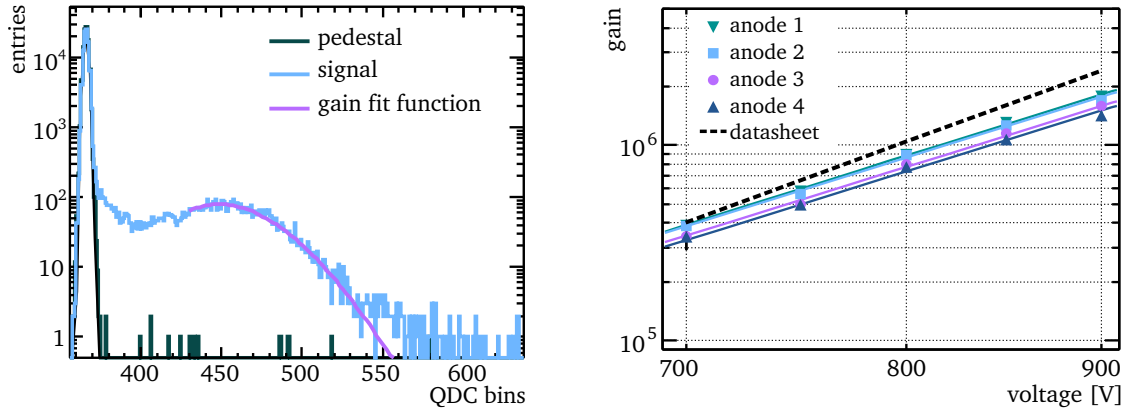

Figure 6.14: (a) QDC signal for a measurement without light (pedestal) and with a small amount of light (signal), as well the fit to the signal used to determine the gain. The graph in (b) shows the fitted gain of one of the R7600U04 photomultipliers for different supply voltages, with the dashed line indicating the typical values provided in the datasheet.

The filter strength and LED voltage were chosen such that in a measurement with 100 000 pulses applied to the LED, only the dark current signal was observed in the QDC spectrum ≈95 % of the time. Assuming that the photons reaching the photomultiplier are Poissonian distributed, and that the quantum efficiency can be modelled by a binomial distribution with 20 % probability for detection, this means that in the ≈90 % of the remaining 5 % of the events, in which a signal was observed, this signal stems from a single photon. Figure 6.14(a) shows one such measurement, in addition to a pedestal-only measurement. After subtracting the pedestal, the remaining one-photon signal was fitted to determine the gain with a Gaussian of mean p_1, width p_2 and normalisation constant p_0:

$$f(x) = p_0 \cdot e^{-(x'-p_1)^2/2\cdot p_2^2}, \qquad \text{with } x' = x \cdot \frac{\text{QDC resolution}}{\text{electron charge}}. \tag{6.1}$$

By converting the x-axis values from QDC bins to electrons, the fitted mean p_1 provides the mean number of electrons measured in the QDC, which corresponds to the gain in the single photon case.

Data was taken at five different supply voltages from 700 V to 900 V. The deter-

gain	anode 0	anode 1	anode 2	anode 3
R7600U-03	$1.17(1)\cdot10^6$	$1.23(1)\cdot10^6$	$1.29(1)\cdot10^6$	$1.21(1)\cdot10^6$
R7600U-04	$1.22(1)\cdot10^6$	$1.26(1)\cdot10^6$	$1.30(1)\cdot10^6$	$1.14(1)\cdot10^6$

gain	anode 5	anode 6	anode 7	anode 8
R7600U-03	$1.79(1)\cdot10^6$	$1.70(2)\cdot10^6$	$1.58(2)\cdot10^6$	$1.41(2)\cdot10^6$
R7600U-04	$1.36(3)\cdot10^6$	$1.32(2)\cdot10^6$	$1.53(1)\cdot10^6$	$1.40(2)\cdot10^6$

Table 6.5: Measured anode gain at 900 V for the photomultipliers R7600U-03-M4 and R7600U-04-M4 used with the quartz prototype. The errors given are purely statistical errors.

mined gain followed a logarithmic behaviour as expected. As an example, the fitted gain for all four anodes of one of the R7600U-04 photomultipliers is shown in figure 6.14(b).

Of main interest is the gain at 900 V, since this is the supply voltage used during the testbeam. All fitted gain values are listed in table 6.5. They are of the same order of magnitude as the typical values provided by Hamamatsu (figure 6.1(b)), but a factor $\approx 2.5-4$ ($\approx 1.5-2.1$) lower in case of the R7600U-03 (R7600U-04) photomultipliers. In contrast to the datasheet values, there is no general difference in the measured gain discernible between the two photomultiplier types, which is in line with the measurements at the testbeam, where also no difference between the photomultipliers was noticed.

Light yield and comparison to the simulation

Once the gain of the photomultipliers is known, the measured QDC signals can be compared to the simulation's predictions for the number of detected photons. The high range of the QDC which was used during the testbeam campaign has a resolution of 200 fC. One QDC bin therefore corresponds to $\approx 1.25\cdot10^6$ electrons.
The highest and lowest values listed in table 6.5 of $(1.79\pm0.01)\cdot10^6$ and $(1.14\pm0.01)\cdot10^6$ for anode 1 and 2 of the R7600U04 photomultiplier means that 1 QDC bin corresponds

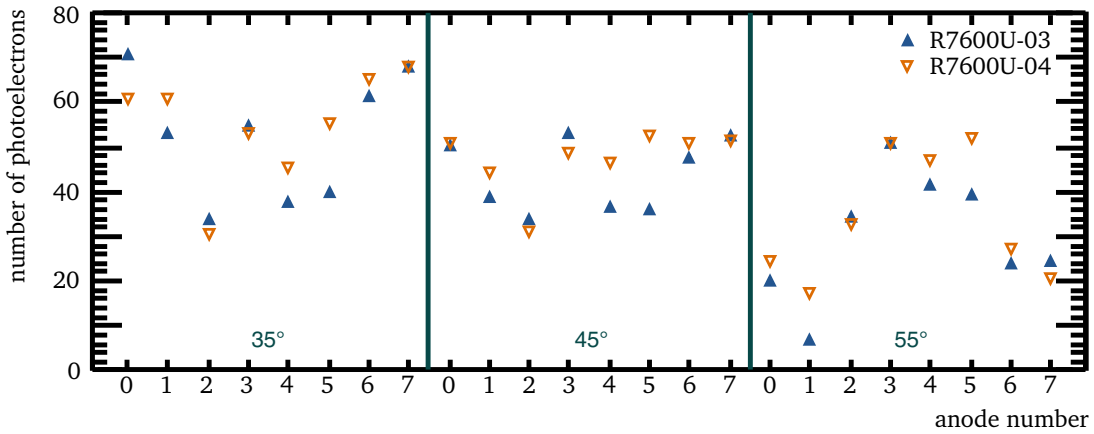

Figure 6.15: Light yield calculated from data taken with both photomultiplier types at three different angles, converted from QDC bins to photoelectrons using the measured photomultiplier gain.

to ≈1.43 QDC bins per photoelectron and ≈0.91 QDC bins per photoelectron respectively. Corresponding calculations can be done for the other anodes.

For each detector channel, data was taken under three different angles (35°, 45°, 55°) with both photomultiplier types. Figure 6.15 shows the number of photoelectrons obtained for these configurations, calculated using the gain conversion factors explained above. Qualitatively, the observations agree with the expectations from the simulation (c.f. section 5.2.3): The amount of light detected in a channel decreases for larger angles. For the measurements at 45°, close to the Cherenkov angle, the light distribution on the photocathode is the most uniform, resulting in similar amounts of light for the inner (2-5) and outer (0,1,6,7) anodes. No systematic difference between the two photomultiplier types can be observed. Quantitatively, there are differences between the light yield between the channels. One possible cause for this could be an uneven application of the optical grease during the mounting of the photodetectors.

For the configuration with the highest light yield, at 35°, summing up the signal for both anodes of a channel yields 107 ± 12 photoelectrons. This number is somewhat higher than the expectation from the simulation, which predicts ≈70 photoelectrons for an incidence angle of 35°. The numbers for all configurations listed above were compared to simulations using the same respective photomultiplier and

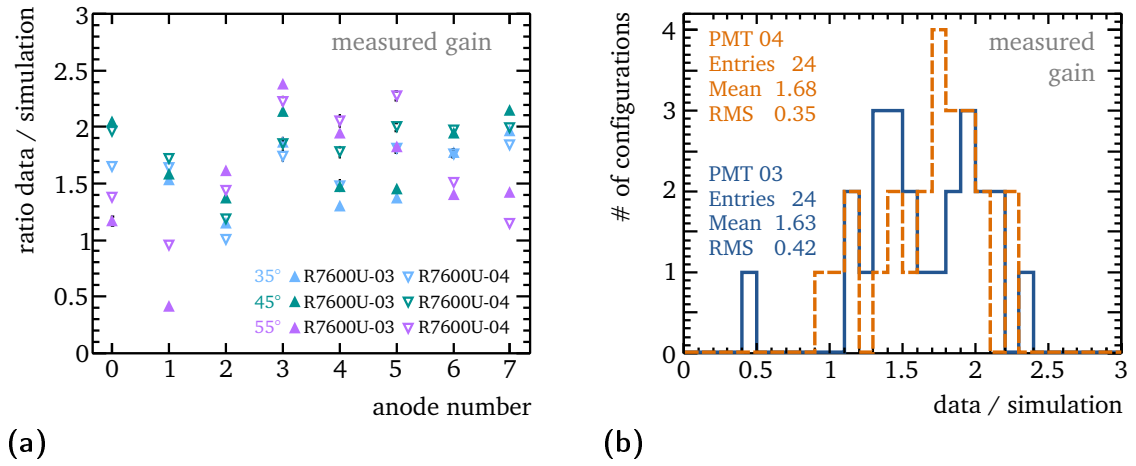

Figure 6.16: Ratio between the light yield calculated from the data (using the measured gain) and the number of detected photons predicted by the simulation. The graph on the left (a) shows the ratio for all anodes of both photomultipliers, for measurements at three different incident angles. The observed relations are summarised in (b).

incidence angle. The ratio between the observed number of detected photons in the data and the predictions from the simulation, i.e. $\frac{\#\text{photoelectrons}_{\text{data}}}{\#\text{detected photons}_{\text{simulation}}}$, for all configurations are shown in figure 6.16(a). On average, the amount of detected light calculated from the data is a factor of 1.7 ± 0.4 higher than expected based on the simulation.

This might be partly an effect of additional light provided by secondary electrons, as discussed in section 6.3.2, or of contributions to the photomultiplier signal from photons absorbed on one of the amplification dynodes instead of the photocathode, as described in section 6.3.1. In addition to this, a number of assumptions where made in the simulation, such as the roughness of the quartz surface, and the thickness of the optical grease layer. Therefore, the agreement between the data and the light yield in the simulation is still quite satisfactory.

It is also possible that the procedure for the gain measurement described in section 6.3.3 above systematically underestimates the gain, as might be concluded from the fact that the measured gain is consistently lower that the value given by the photomultipliers' datasheet. Since the datasheet values are higher, a comparison using those gain values instead of the measured ones would result in the determination of an

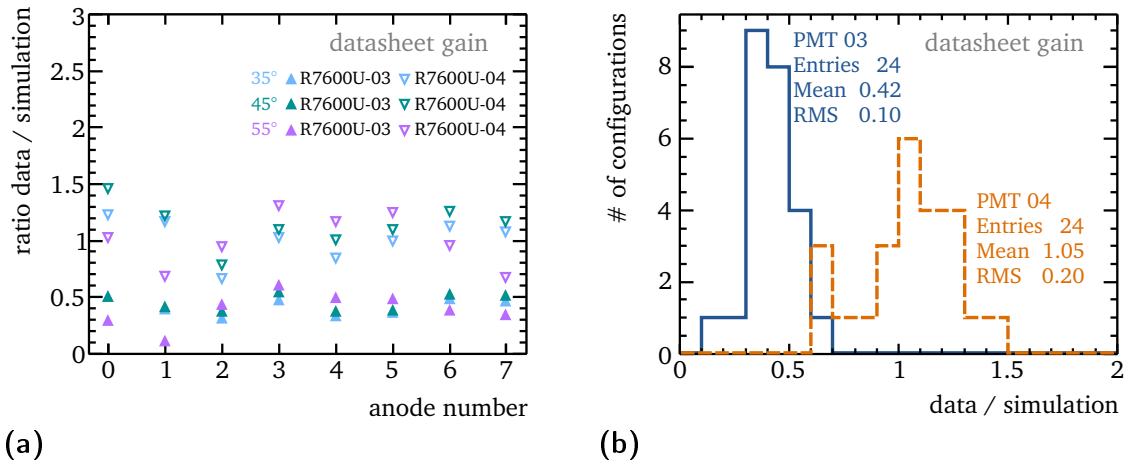

Figure 6.17: Ratio between the light yield calculated from the data (using the datasheet values for the gain) and the number of detected photons predicted by the simulation. The graph on the left (a) shows the ratio for all anodes of both photomultipliers, for measurements at three different incident angles. The observed relations are summarised in (b).

accordingly lower light yield from the data: for the R7600U-03 type photomultipliers, summing up the signal at 35° for both anodes of a channel yields 27 ± 3 photoelectrons, while for the R7600U-04 type photomultiplier a yield of 67 ± 5 photoelectrons per incident electrons results. The ratio between the number of detected photons calculated from the datasheet gain compared to the simulation is shown in figure 6.17, analogous to the plots for the measured gain in figure 6.16). While the light yield calculated from the datasheet values of the R7600U-04 photomultiplier are well in agreement with the simulation, the one for the R7600U-03 is more than a factor of two below the simulation prediction. There is a strong disagreement between the calculations with the datasheet values of the two photomultiplier types. Along with the fact that the gain values given in the datasheet are “typical values“ and not measured individually for the specific photomultipliers used with the prototype detector, it seems reasonable to place at least an equal degree of reliance on the results using the gain measurements in table 6.5.

6.3.4 Horizontal alignment and beam spot size

To determine how well the prototype detector can be aligned from data alone, the detector position was scanned by varying the position of the movable table in x-direction in 1 mm steps. Studying the observed number of events in each detector channel for the different x-positions allows to determine the position of the channel with respect to the beam, as well as derive information on the size and shape of the beam spot. For a pointlike beam and perfect alignment, the channel response would be expected to have a "box-like" shape, whereas a finite beam-size and tilts around the vertical axis will smear out the edges of this step response function.

Channel positions

As a measure for the events per channel, the area of the fitted Landau function is plotted versus the table position in figure 6.18(a). The number of events per channel will be maximal when the beam is aligned with the centre of this channel. To determine the channel centres, the measurements for each anode were fitted with a box function convoluted with a Gaussian. The box function is 1 for all x within ± 2.5 mm of its central value, to describe the prototype channel width of 5 mm, and the Gaussian is

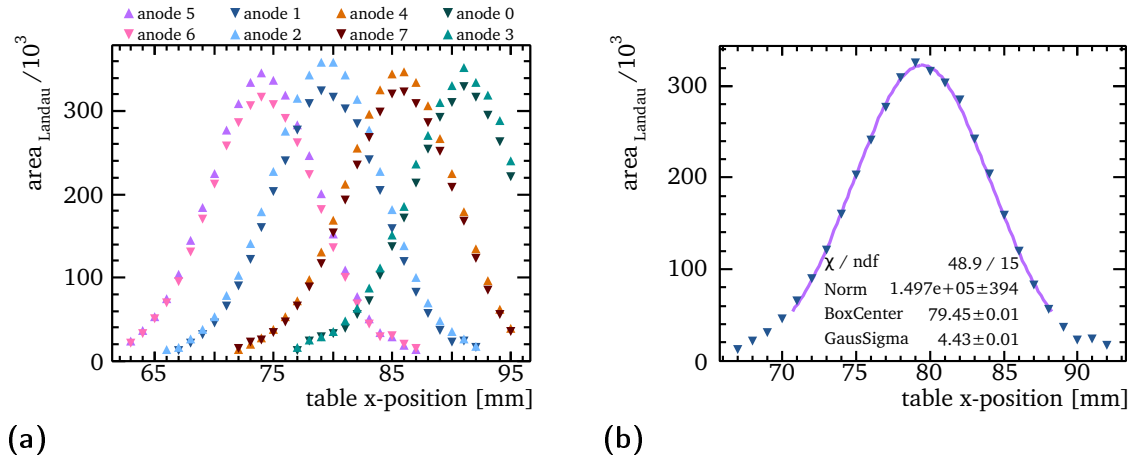

Figure 6.18: (a) Signal observed at different x-positions of the detector. (b) Signal of anode 1, fitted with a box function convoluted with a Gaussian (as in equation (6.2)).

channel	anode	channel centre	anode	channel centre
A	5	(74.12 ± 0.01) mm	6	(74.07 ± 0.01) mm
B	1	(79.45 ± 0.01) mm	2	(79.47 ± 0.01) mm
C	4	(85.54 ± 0.01) mm	7	(85.57 ± 0.01) mm
D	0	(91.10 ± 0.03) mm	3	(91.15 ± 0.02) mm

Table 6.6: Channel positions fitted to x-scan data, with statistical errors from the fit. The central values for the two anodes per channel agree within 0.05 mm or better with each other. The positions are given in the coordinate system of the movable table's control software.

used to account for the smearing. The convolution is implemented as sum within four sigma of the Gaussian, i.e.

$$f(x) = p_0 \cdot \sum_{\tau=p_1-4\cdot p_2}^{p_1+4\cdot p_2} \mathrm{box}(\tau, p_1) \cdot \frac{1}{p_2\sqrt{2\pi}} e^{-(x-\tau)^2/2\cdot p_2^2}, \tag{6.2}$$

where the free parameters are a normalisation factor p_0, the centre position p_1 of the channel box function, and the sigma p_2 of the Gaussian.

The channel centre positions derived from these fits are listed in table 6.6. The fitted centre positions to the data from the upper anodes of each channel all agree within 0.05 mm with the fitted positions for the respective lower anodes, indicating that the detector position can be determined within a precision of the same order, which meets the requirements for the horizontal alignment precision.

Beam profile

In the fit of equation (6.2) to the x-scan data of all eight anodes, the sigma of the convoluted Gaussians were found to be $\sigma = (4.5 \pm 0.1)$ mm (table 6.7).

To verify that a beam profile with this extension would cause the smearing observed in the testbeam data, x-scans with different beam spots were simulated and compared to the measurement in figure 6.18(a). To allow a comparison of the shape of the channel response, the signal strength is normalised to the maximum signal. Again, the best

channel	anode	fitted sigma p_2	anode	fitted sigma p_2
A	5	(4.40 ± 0.01) mm	2	(4.53 ± 0.01) mm
B	1	(4.44 ± 0.01) mm	6	(4.37 ± 0.01) mm
C	4	(4.48 ± 0.01) mm	7	(4.43 ± 0.01) mm
D	0	(4.53 ± 0.02) mm	3	(4.65 ± 0.02) mm

Table 6.7: Width of the Gaussian for the fit of the smeared box function equation (6.2) to x-scan data.

agreement was found for a Gaussian beam profile with $\sigma = 4.5$ mm. Figure 6.19(a) shows the signal strength for the simulation with this beam profile size compared to the data.

In figure 6.19(b), the discolouration caused by the electron beam on a piece of black-and-white photographic film (Agfa APX 400) after an exposure time of 48 hours can be seen. While it is not possible to quantify the σ of the beam profile from looking at this, both the extension as well as the shape of the discoloured spot support the assumption of a circular beam profile with several millimetres diameter. Unless otherwise stated, all comparisons of the testbeam data to simulations are performed for simulations with a beam profile of $\sigma = 4.5$ mm.

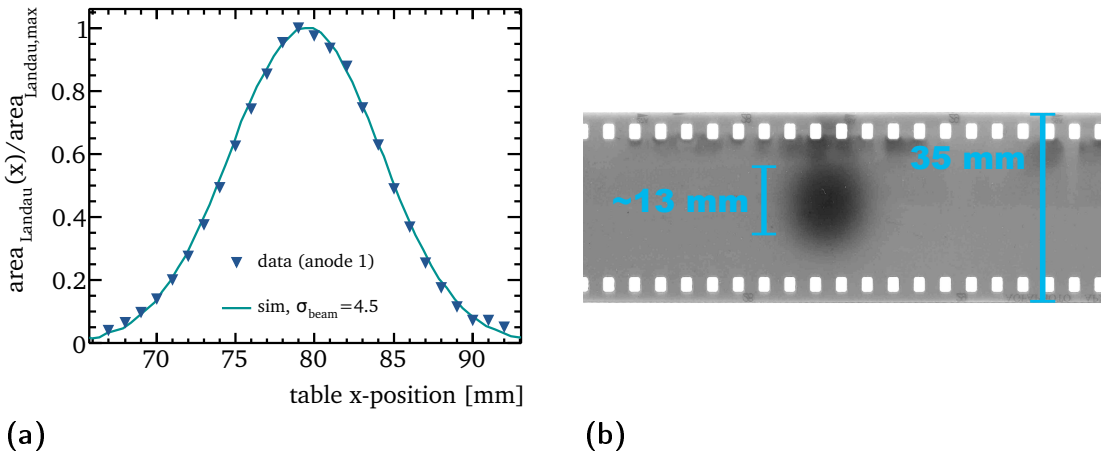

Figure 6.19: (a) Data at different x-positions compared to a simulation with a beam profile size of $\sigma = 4.5$ mm. (b) Discolouring of a photographic film caused by the beam as in indication for the size and shape of the beam spot.

6.3.5 Vertical alignment

At the beginning of the testbeam campaign, the position at which the detector was centred with respect to the beam in vertical direction was determined by eye to be at a table position of $y = 76\,\text{mm}$ (in the coordinate system of the steering software for the movable table).

To test how well this detector alignment in the vertical direction was, data was taken at different y-positions of the movable table over a range of 40 mm, with the beam centred between channel C and D. Once the beam moves far enough down from the vertical centre that it enters channel D through the end face rather than the narrow side face, the path length for light production and thus also the amount of detected light will decrease rapidly. The same is true for channel C when the beam entrance point is moved upwards high enough.

In order to determine the centre in y-direction, this effect was used to compare the data to a simulated y-scan. Two parameters need to be adjusted in this comparison: the first is a scaling constant, to account for the difference in light yield in data and simulation; the second is an offset in the y-position, i.e. how far the y-axis of the

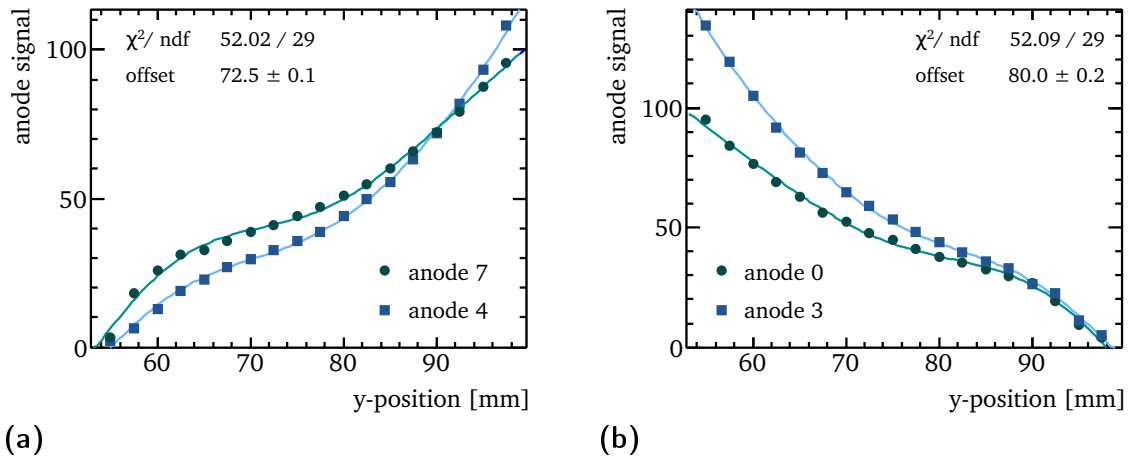

Figure 6.20: Signal observed at different y-positions of the detector for (a) channel C and (b) channel D for both anodes of the channel (markers). The solid lines are the fits of a simulated y-scan to the signal of both anodes per channel, with a shift of the y-axis as a free parameter.

simulation (with the detector centre at position 0 mm) has to be shifted to match the data (with y-positions given in the coordinate system of the table software.
A separate fit was done for both channel C and D. In these fits, both anode of the respective channel were compared to the simulated y-scan, allowing individual scaling factors for each anode in addition to the common offset in y-direction. Figure 6.20 shows the data together with the scaled and shifted simulated y-scans. The fit to the data of channel C returns a vertical centre y-position of (72.5 ± 0.1) mm, the fit to channel D a y-position (80.0 ± 0.2) mm. These results do not agree within their fit errors. This is most likely due to the fact that the kinks in the channel response (at the y-positions where the rapid light yield decrease sets in) are smeared out by the large beam spot size of $\sigma = 4.5$ mm. Therefore the distinct edges of the channel edges, which would be the most discriminating factor in the alignment, are washed out. This can be seen in figure 6.21, where simulated y-scans for both $\sigma = 0.1$ mm and $\sigma = 4.5$ mm are shown.

Another explanation could be if the prototype detector was not perfectly aligned in the x-z-plane. The ground plate on which the detector box was standing was only affixed to the movable table on one side, making it possible that the whole setup was

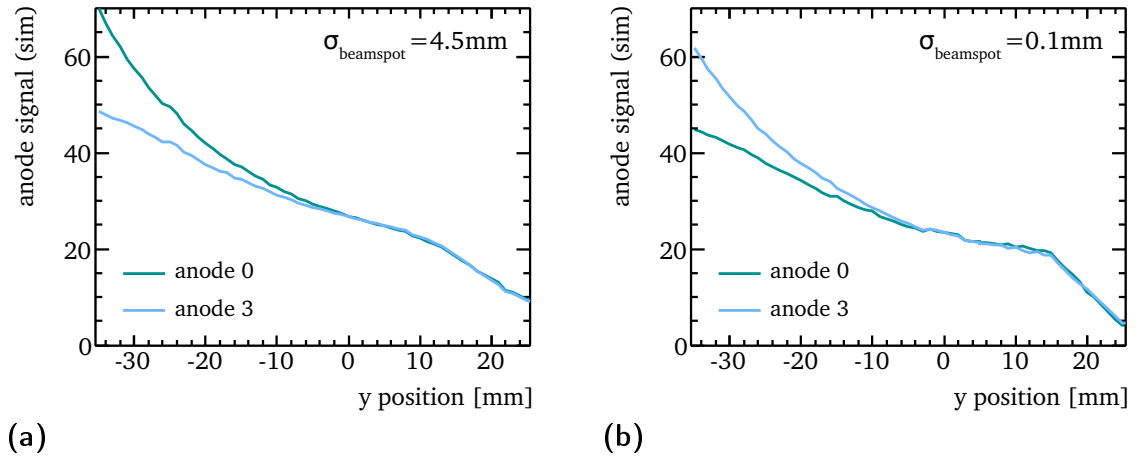

Figure 6.21: Simulated y-scan for two different beam spot sizes. (a) $\sigma = 4.5$ mm corresponds to the beam spot size determined for the testbeam data, while in (b) a much smaller beam profile of $\sigma = 0.1$ mm was simulated. For the small beam profile, the point where the beam begins to enter through the end face (around $y = 15$ mm) is clearly pronounced.

tilted slightly around the z-axis. This would induce correlations between the x- and y-coordinate, which would affect channel C and D differently and lead to different vertical centre positions. While a large tilt would have been visible by eye, a small misalignment in α_z cannot be excluded.

The fit results do however confirm that the first estimate by eye of a centre at $y_{\text{table}} = 76\,\text{mm}$ was accurate within a few millimetres. Under conditions where the vertical spread of the incident particles is smaller, a better alignment precision is expected.

6.3.6 Angular dependence of detector response

The prototype detector was constructed with a mechanical setup allowing to change the angle between the incident electron and the detector channels. This offers the possibility to study the detector response under different alignments in greater detail than for a setup with a fixed angle, to provide additional information of the detector response which can be compared to the expectations from the simulation.

Stability

The angle between the upwards- and downwards-facing channels and thereby the angle between the detector channels and the beam was calculated from the internal step counter of the stepping motor used to change the angle. At the edges of the allowed movement range, a mechanical end-switch was located, which stopped the motor movement when it was pressed. Unfortunately, it seems that the stepping motor sometimes "got stuck" upon leaving this end-switch, causing a disagreement between the angle calculated from the step counter, and the actual angle. This becomes evident by comparing the detector response for individual angle scans taken under otherwise unchanged conditions. Figure 6.22(a) shows the signal for both anodes of channel B for two consecutive angle scans, the first one from 30° to 60°, where the end-switch was reached, immediately followed the second angle scan back from 60° to 30°. The detector response for the second data set shows the same behaviour, albeit shifted somewhat

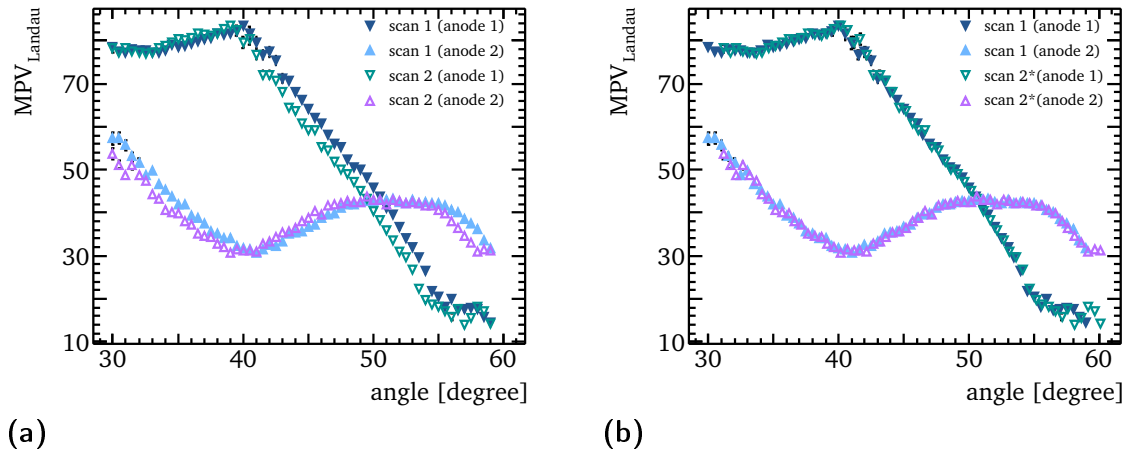

Figure 6.22: (a) Signal for both anodes of channel B for two consecutive angle scans, the first one from 30° to 60° (solid markers), the second one in the opposite direction (open markers). In (b), the second scan is shifted by 1.15°, resulting in an improved agreement between the two data sets.

to lower angles. By correcting the angle coordinate of the second scan by 1.15°, a much better agreement is reached, as shown in figure 6.22(b).

Three such data sets were taken during the testbeam campaign. The angle correction required to obtain the best agreement between the first and second scan were 1.15°, 0.69° and 0.78°. This leads to the conclusion that the given angles for the testbeam data are afflicted with an uncertainty of $\mathcal{O}(1°)$.

Comparison of angular detector response to simulation

In simulation studies, it was found that the shape of the angular response function of the detector depends on the smoothness of the quartz surface. For a more polished surface, i.e. a smaller microfacet distribution parameter σ_α, more directed reflections occur. Consequently, a change in the incidence angle of the beam causes larger changes compared to reflections on a rougher surface, as can be seen in figure 6.23(a).

An offset in the vertical direction moves the central point of the beam crossing by $\Delta y / \sin\alpha$. This means that such an offset mostly affects the detector response at small

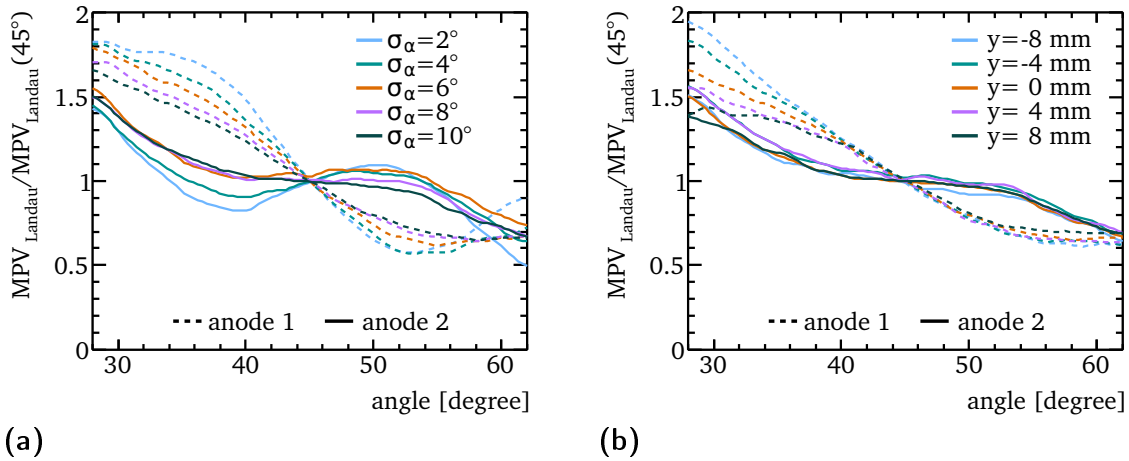

Figure 6.23: Simulated detector response under different angles, normalised to the signal at 45°. (a) Different surface polish levels σ_α and (b) offsets in the vertical directions affect the response function.

angles (figure 6.23(b)). For larger angles, the effect of different offsets is hard to distinguish, reducing the overall sensitivity to vertical offsets.

For the quartz bars used in the prototype detector, the surface smoothness was not known. In addition to this, the vertical alignment could only be done within an uncertainty of several millimetres. Therefore, the possibility to determine σ_α and Δy by comparing the data to simulated angle scans was investigated.

The data of different angle scans taken during the testbeam campaign were each compared to a number of simulated angle scans with different choices for σ_α and Δy. In order to compare the shape of the detector response function independent of the absolute light yield, the response functions for both data and simulation were normalised to their respective signal at 45°. To account for the observed uncertainty in the angle reading for the data discussed above, a fit similar to that for the vertical alignment (c.f. section 6.3.5) was performed to both anodes of a channel simultaneously, in this case with the offset in angle as the single free parameter.

Figure 6.24(a) shows the goodness of fit for the comparison between an angle scan performed at $y_{\text{table}} = 70\,\text{mm}$ and different simulated angle scans. For any given vertical offset, the best agreement is found for either $\sigma_\alpha = 4°$ or $\sigma_\alpha = 6°$. This was the case for all angle scans which were compared to the simulation, leading to the conclusion that

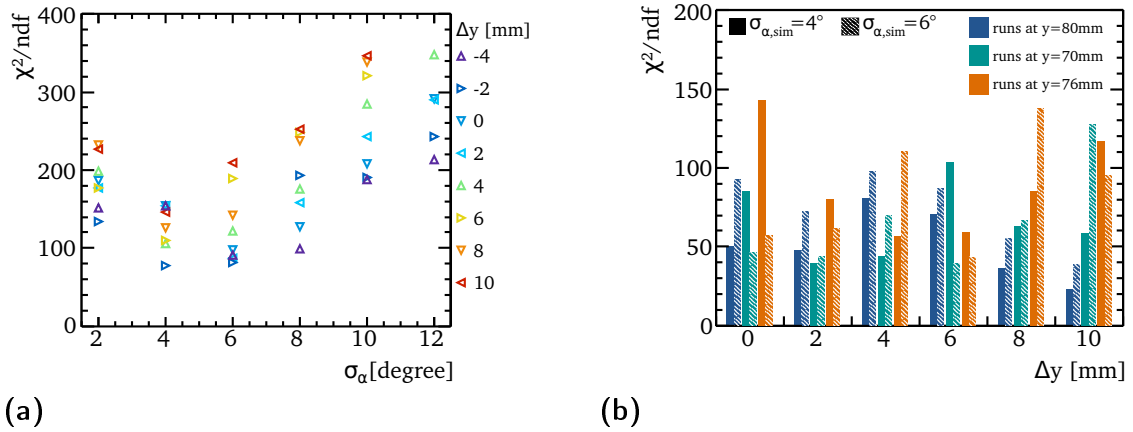

Figure 6.24: Comparison between the angular response function of the detector between data and simulation. (a) shows the goodness of fit between an angle scan at $y_{\text{table}} = 70\,\text{mm}$ and simulations with different settings for vertical misalignment and surface smoothness. (b) Goodness of fit in the comparison of three different angles scans to simulations with $\sigma_\alpha = 4°$ and $\sigma_\alpha = 6°$. The offset Δy is givens with respect to the assumption that the setup was centred at $y_{\text{table}} = 76\,\text{mm}$.

a surface smoothness in this range would be a good description of the quartz bars used in the prototype detector.

For the vertical offset, no definite conclusions could be drawn. For the run shown in figure 6.24(a), the best agreement between data and simulation would be expected for $\Delta y = -6\,\text{mm}$ if the centre of the setup was at 76 mm as assumed during the data taking. In case of this angle scan, the best fit agreement to the simulation was found for $\Delta y = -8\,\text{mm}$. However, other values for Δy showed a comparable goodness of fit. This is further illustrated by figure 6.24(b) for three different angle scans at different y-positions of the table: the goodness of fit to simulations with $\sigma_\alpha = 4°$ and $\sigma_\alpha = 6°$ is shown for six different vertical offsets (compared to the assumption that the vertical centre was located at 76 mm). No single configuration was found to describe the data significantly better than any other.

When comparing the shape of data and simulation, it becomes apparent that the simulation does not describe the angular response satisfactorily for angles $\gtrsim 55°$. To illustrate this, figure 6.24 shows the two simulated angle scans with the best agreement to the data of the angle scan at $y_{\text{table}} = 70\,\text{mm}$. The differences in the shape of

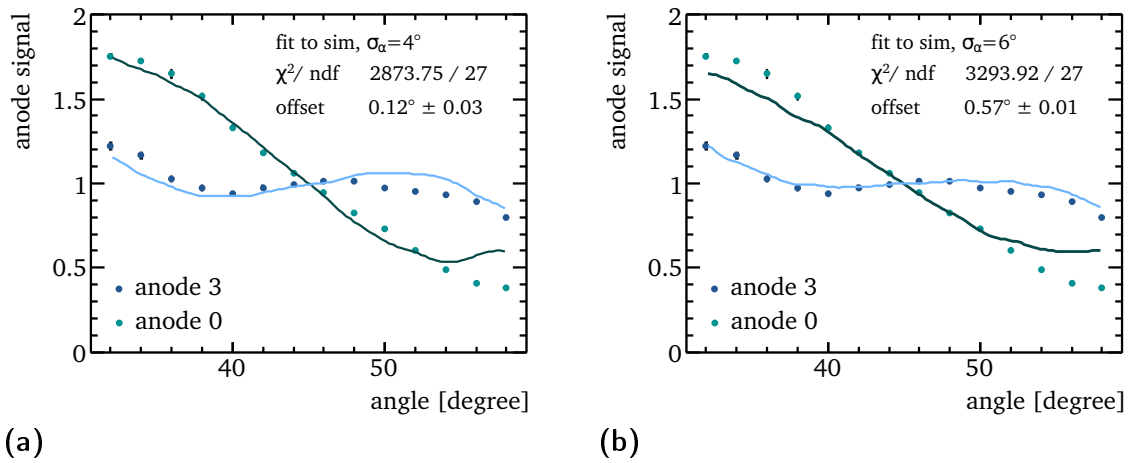

Figure 6.25: Shape of the angular response function for the angle scan at $y_{\text{table}} = 70\,\text{mm}$, compared to the best-matching simulations at (a) $\sigma_\alpha = 4°$ and (b) $\sigma_\alpha = 6°$ respectively.

the response function hint that additional factors must be present which are not well modelled in the current simulation.

6.3.7 Results of the testbeam campaign

In the analysis of the testbeam data, the light yield observed in the data based on the measured gain of the photomultipliers surpassed the simulation predictions of ≈70 detected photons per incident electron by a factor of 1.7 ± 0.4, yielding 107 ± 12 photoelectrons per incident electron. A more detailed modelling of the experimental setup might close the gap between prediction and measurement.
Using the datasheet values for the photomultiplier gain instead of the measured ones leads to diverging yields of 27 ± 3 (67 ± 5) photoelectrons for the R7600U-03 (R7600U-04) type photomultipliers. Without a precise knowledge of the photomultiplier gain, an exact determination of the light yield per electron is not possible. Regardless, the observed light yield agrees with the simulation predictions within a factor of ≈2, leading to the expectation that the predictions for the larger channels optimised for maximum light yield (c.f. chapter 5) would also be reached within the same magnitude. In that case, a detector setup yielding a few hundred detected photons per incident electrons is possible.

Qualitatively, the prototype detector's response under different positions and angles was also described satisfactorily by the simulation. An alignment within $< \mathcal{O}(0.05\,\mathrm{mm})$ in the horizontal direction was achieved.

The surface roughness of the quartz bars used in the construction of the prototype detector could be estimated from the test beam data and is best described by a microfacet distribution between $\sigma_\alpha = 4°$ and $\sigma_\alpha = 6°$.

The vertical and angular alignment require further investigation, preferably under better constrained conditions, i.e. a smaller beam spot size and a more accurate determination of the vertical alignment independent of the data. Further improvements to the experimental setup are conceivable, such as a better solution for the steering motor behaviour at the limits of its motion range.

Since the light yield of the prototype detector proved promising in lights of reaching the required light yield with a quartz based detector discussed in section 4.2.2, the design concept presents an interesting option for the ILC polarimeter, which makes such follow-up studies worthwhile.

7

Application in the ILC polarimeter

The central motivation for investigating a detector concept with quartz as Cherenkov medium was the consideration that the ability to resolve individual Compton electron peaks in the QDC spectrum would increase the tolerance to photodetector non-linearities. Considering the results of the previous chapters, a light yield of 300 photoelectrons per Compton electron seems feasible. It remains to be checked how the polarisation measurement at the ILC could profit from this. In this chapter, a fit procedure for spectra with single-peak resolution will be presented, and its performance in simulated polarisation measurements under different conditions discussed.

7.1 Fit for individual channels

To develop a fit procedure, QDC spectra for multiple electrons in a channel were generated with the Monte Carlo simulation already briefly mentioned in chapter 4, extended by the additional option to add a non-linear component to the amplification of the charge in the photodetector and a more realistic implementation of statistical fluctuations in the gain.

Spectrum generation

A schematic overview of the different parts of the simulation and the inputs for the spectrum generation is shown in figure 4.4.

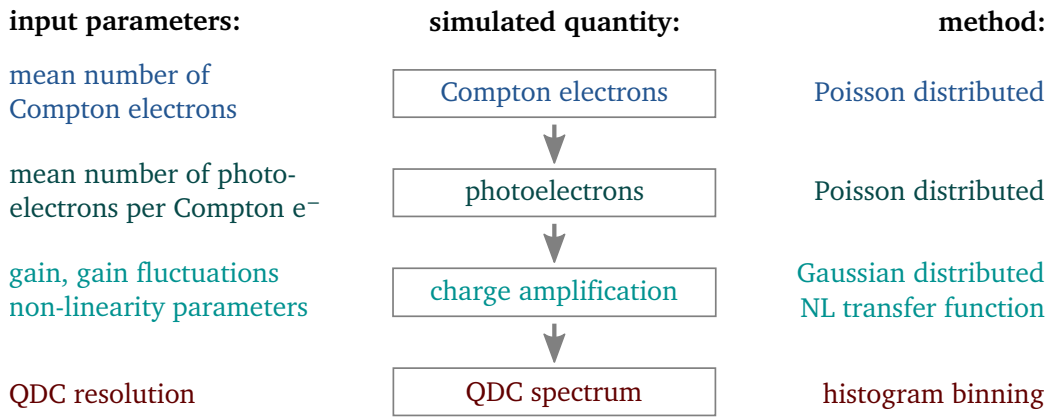

Figure 7.1: Schematic overview of the Monte Carlo simulation used to generate QDC spectra, with the input parameters for each simulated quantity in the left column and the method used to implement the expected statistical effects for each step in the simulation in the right column.

The mean number of Compton electrons $N_{\text{C.e.}}$ is used as the first input parameter. For each simulated event, the actual number of electrons $i_{\text{C.e.}}$ is chosen from a Poissonian distribution generated with the ROOT[47] random generator TRandom3. The mean number of photoelectrons per Compton electron p also has to be specified as input. As a parameter combining the number of photons reaching the photocathode and the quantum efficiency of the photomultiplier, p is effectively Poissonian distributed. Therefore, a number of photoelectrons is randomly chosen according to a Poissonian distribution around p for each of the $i_{\text{C.e.}}$ electrons.

The charge of all photoelectrons is amplified by a specific gain g, including Gaussian distributed gain fluctuations within a width of σ_g. To account for the digitisation of the signal, the charge is filled into a histogram with a binning corresponding to the QDC resolution. For the following discussions, the properties of the QDC used with the prototype detector are implemented, i.e. a resolution of 200 fC and a range of 12 bit (4096 bins).

Modelling of the photomultiplier gain

To model non-linearities in the behaviour of the photomultiplier, a random non-linear transfer function $T(x)$ can be generated. $T(x)$ is a fourth-order polynomial with a

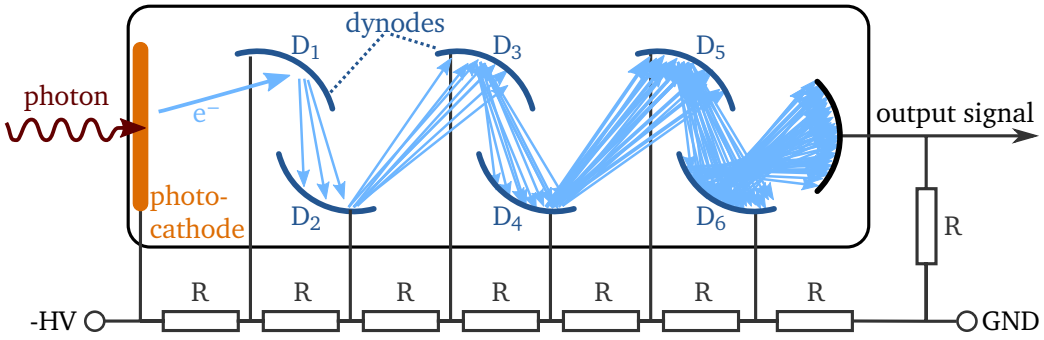

Figure 7.2: Simplified sketch of a photomultiplier tube. The variance in the charge amplification is dominated by the statistics at the first few dynode stages. The signal-to-noise ratio can be enhanced by using a tapered voltage divider circuit which enhances the voltage gradient at the first stages (by using larger resistances) and thereby the secondary emission ratios of the corresponding dynodes.

chosen non-linearity over the dynamic range of the simulated spectra (see appendix C of [32] for details). By applying this transfer function to the central value of the gain, a non-linear detector response is obtained.

For the statistical fluctuations in the amplification process, either a fixed amount of noise can be used or, as a more realistic approach, the gain fluctuations can be calculated from the statistics of the multiplication process in the photomultiplier for the mean number photoelectrons produced at the photocathode for a given number of electrons. The amplification of the primary photoelectrons happens in a cascade from the first to the last dynode of a photomultiplier tube, as sketched in figure 7.2. The statistical fluctuations in each amplification step depend on the secondary emission ratios of the dynodes, i.e. the number of secondary electrons emitted when an electrons strikes the dynode For a photomultiplier with n dynode stages, a single photoelectron gives rise to a charge avalanche with mean $g = \delta_1\delta_2\cdots\delta_n$ and variance

$$\sum_{i=1}^{n}(\delta_1\delta_2\cdots\delta_n)(\delta_{i+1}\cdots\delta_n)^2 \tag{7.1}$$

with δ_i the secondary emission ratio of the i-th dynode[52]. Typical values for δ are in the range 6-12, depending on the dynode material and rising with the voltage gradient accelerating the electrons towards the dynode[53].

The first dynode is the most important in determining σ_g. To simplify the expression, one can consider the case where all secondary emission ratios except for the first dynode are equal, i.e. $\delta_2 = \delta_3 = \cdots = \delta_n = \delta$. In that case, equation (7.1) can be rewritten as

$$(\delta^n)^2 \frac{1}{\delta_1}(1 + \frac{1}{\delta} + \frac{1}{\delta^2} + \cdots + \frac{1}{\delta^{n-1}}) \approx g^2 \frac{1}{\delta_1}\frac{\delta}{\delta - 1}. \tag{7.2}$$

For an event with a charge avalanche starting with $p' = p \cdot i_{\text{C.e.}}$ electrons, the gain uncertainty can consequently be described by

$$\sigma_g = \sqrt{\frac{1}{p'\delta_1}\frac{\delta}{\delta - 1}}. \tag{7.3}$$

For the simulation of the QDC spectra in this chapter where the gain was modelled according to equation (7.3), using the secondary emission ratios $\delta_1 = 10$ and $\delta = 6$ to calculate σ_g. this is expected to be an reasonable description of the setup used with the prototype detector, based on the gain of the photomultipliers and the schematics of the voltage divider circuits used with them.

Fit procedure

For configurations fulfilling equation (4.4), the spectra were obtained by the simulation setup described above feature separate peaks for the different electrons from the distribution in the Compton electron number. To fit spectra and reconstruct the mean number of Compton electrons per channel, a fit procedure was developed.

As a fit function, a sum of Gaussians with mean $par_{2 \cdot i_{\text{peak}}}$ and width $par_{2 \cdot i_{\text{peak}}+1}$ was chosen, where each Gaussian describes one of n_{peaks} peaks in the spectrum. Since the number of electrons in a channel is expected to follow a Poissonian distribution, the height of the peaks is set to the expectation for i_{peak} electrons from a Poissonian distribution of $N_{\text{C.e.}}$ electrons and scaled to the number of events N_{events} in the spectrum:

$$f(x_{QDCbin}) = N_{events} \cdot \sum_{i_{\text{peak}}=0}^{n_{\text{peaks}}} \text{Pois}(i_{\text{peak}}, N_{\text{C.e.}}) \cdot \text{Gaus}(x_{QDCbin}, par_{2 \cdot i_{\text{peak}}}, par_{2 \cdot i_{\text{peak}}+1}). \tag{7.4}$$

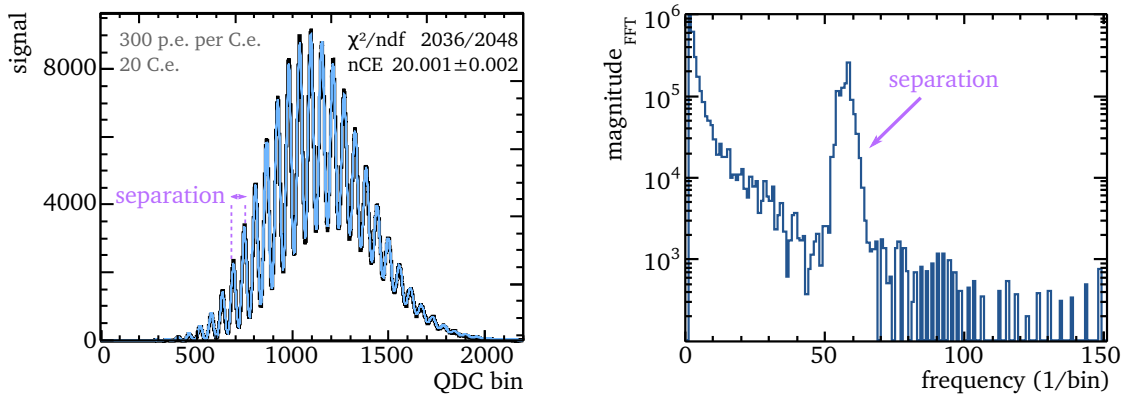

Figure 7.3: Fit procedure for the simulated QDC spectra. (a) shows the spectrum for an average of 20 Compton electrons and 300 photoelectrons per Compton electron (black line) overlaid with the fitted function equation (7.4) (blue line), and (b) the fast Fourier transform of this spectrum to find the peak separation which was used to calculate the start values for the fit parameters.

The free parameters of the fit are the mean and width of all n_{peaks} peaks and the central value $N_{\text{C.e.}}$ of the Poissonian. While studying the distance between the mean values of the individual peaks gives access to the gain linearity, the central value $N_{\text{C.e.}}$ of the Poissonian is the parameter of interest for the polarisation measurement. An example for a fit of equation (7.4) to a spectrum simulated with $N_{\text{C.e.}} = 20$ is shown in figure 7.3(a).

The number of parameters to be fitted grows with the number of electrons per detector channel. For $N_{\text{C.e.}} = 20$, the QDC spectrum is made up of ≈50 peaks and consequently a fit function with ≈100 parameters is required. For such a large number of free parameters, a careful choice of start values for the fit is essential.

The peak separation s between neighbouring peaks is constant for a perfectly linear photomultiplier and changes only gradually for non-linear gain. When a discrete Fourier transform is applied to the spectrum (via the ROOT implementation of the fast Fourier transform library FFTW[54]), this gives rise to a clearly visible peak in the frequency domain (see example in figure 7.3(b)). This can be used to obtain an initial estimate for the peak separation s. From the separation, start values for the

Gaussian parameters can be determined by calculating the expected mean and width as $p_{2\cdot i_{\text{peak}}} = s \cdot i_{\text{peak}}$ and $p_{2\cdot i_{\text{peak}}+1} = \sqrt{2 \cdot i_{\text{peak}}}$. If the peak separation was already known from previous measurements, it could also be provided as in input parameter to the fit program.

Since s corresponds to the scale factor between initial Compton electrons and QDC bins, a start value for $N_{\text{C.e.}}$ can be obtained by fitting a Poissonian $P(x')$ with $x' = {}^{x_{QDC\,bin}}/_{s}$ to the spectrum.

Fit performance

To study the performance of the fit procedure described above, it was applied to simulated QDC spectra for $N_{\text{C.e.}} = 1 - 35$ Compton electrons, gain fluctuations σ_g calculated as described in the previous section, and a mean number of photoelectrons per Compton electron $p = 300$.

How the fit performance changes in the presence of photodetector non-linearities can be seen in figure 7.4(a), which shows the deviation of the fit result from the true value, i.e.

$$\text{deviation} = \frac{\left|N_{\text{C.e.},true} - N_{\text{C.e.},fit}\right|}{N_{\text{C.e.},true}}, \tag{7.5}$$

for fits to spectra with $1 \cdot 10^6$ events with and without an added photodetector non-linearity of 0.5 %. Up to ∼25 Compton electrons, the added non-linearity has little effect. For larger number of electrons, the agreement between fit result and true value starts to degrade. This is most likely a sign that description of the spectrum by the start values calculated for the fit continues does not model the spectrum shape sufficiently well anymore.

The deviations from the true value for small numbers of Compton electrons in a channel are caused by low statistics. Figure 7.4(b) shows the deviation of the fit results from the "true" simulated number of Compton electrons spectra generated from $3.936 \cdot 10^5$ events and $3.936 \cdot 10^6$ events. With the baseline ILC beam parameters of 1312 bunches per bunch train at 5 Hz bunch crossing rate, this would correspond to 1 minute and 10 minutes data taking time at the upstream polarimeter, respectively.

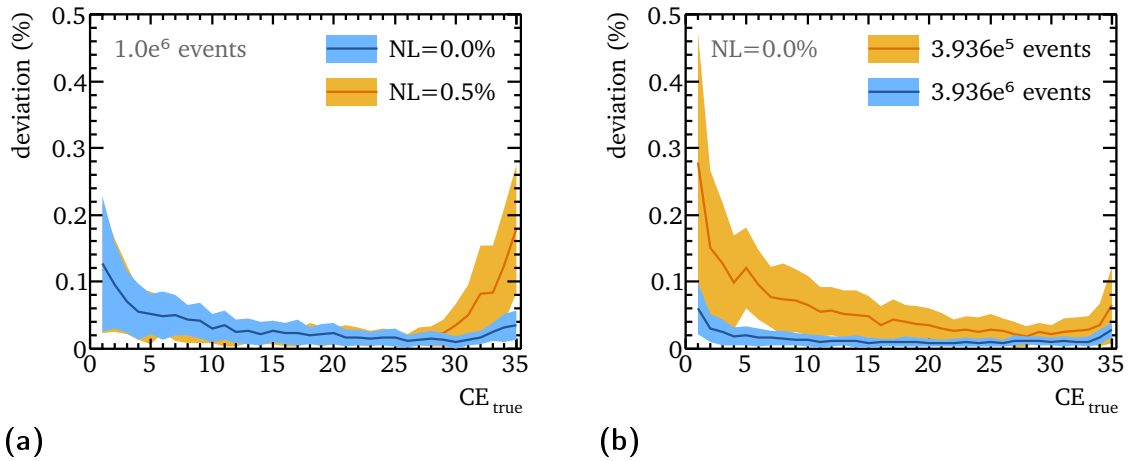

Figure 7.4: Deviation of fit result from true value for simulations with $p = 300$ photoelectrons per Compton electron. The central lines are the mean deviations for 50 simulation runs per number of Compton electrons, the filled bands represent the RMS around the central value. The fit performance is shown for (a) $1 \cdot 10^6$ events with (orange) and without (blue) an added photodetector non-linearity of 0.5 %, and (b) for $3.936 \cdot 10^5$ (orange) and $3.936 \cdot 10^6$ (blue) simulated events without detector non-linearity.

For $3.936 \cdot 10^5$ events, the fit is limited by statistics. The performance profits from a larger data sample. This means that the verification of the photomultiplier response can be repeated on a time scale of 10 minutes. Since the non-linearity is not expected to change rapidly, the actual polarisation measurement can be done on much smaller datasets, with a determination of the peak positions from the data taken in the previous 10 minutes or, in an offline analysis, with a moving average over data taken before and after the individual short-time dataset.

How the deviation between true and fitted number of Compton electrons influences the polarisation measurement will be studied for the conditions expected at the upstream polarimeter chicane in the following.

7.2 Application to polarisation measurement

While the prototype for the quartz detector was built with 5 mm wide channels, no mechanical problems expected in going to somewhat smaller channels. This would

decrease the number of Compton electrons in a channel and thereby increase the ability to fit the number of Compton electrons from measured QDC spectra. The simulated polarisation measurements discussed in this section are based on a detector array consisting of 60 channels with a width of 3 mm. The impact of photodetector non-linearities on the polarisation measurement will be investigated for two scenarios: in the first case $3.936 \cdot 10^6$ events for 80 % beam polarisation are used. As a more challenging case a polarisation of 30 %, with a correspondingly smaller asymmetry in each channel, is combined with a factor of 10 less events.

7.2.1 Upstream polarimeter expectations

The fast Linear Collider Polarimeter Simulation `LCPolMC` was used[21, 26] to generate Compton events for a selected number of bunch crossing for a given set of laser and beam parameters, and subsequently track the Compton electrons through the polarimeter chicane to the detector. An array of 60 channels was considered, with a width of 3.0 mm and 0.33 mm inter-channel spacing. The beam and laser parameters used for the simulation are chosen according to the expectations at the polarimeter locations for the ILC TDR beam parameters, as listed in table 7.1.

Figure 7.5 shows the mean number of Compton electrons in a channel after 393600 bunch crossings, corresponding to 1 minute of data taking at TDR data rates for both laser helicities. For both 30 percent and 80 percent polarisation, the mean number of

	e^+/e^- beam	laser beam
energy	250 GeV	2.33 eV
bunch charge/energy	$2 \cdot 10^{10}$ e	35 µJ
bunches per train	1312	1312
bunch length σ_z	1.3 ps	10 ps
transverse size σ_{xy}	32 µm × 3 µm	50 µm × 50 µm

Table 7.1: Parameters of the electron and laser beam used in the simulation of Compton scattering at the upstream polarimeter.

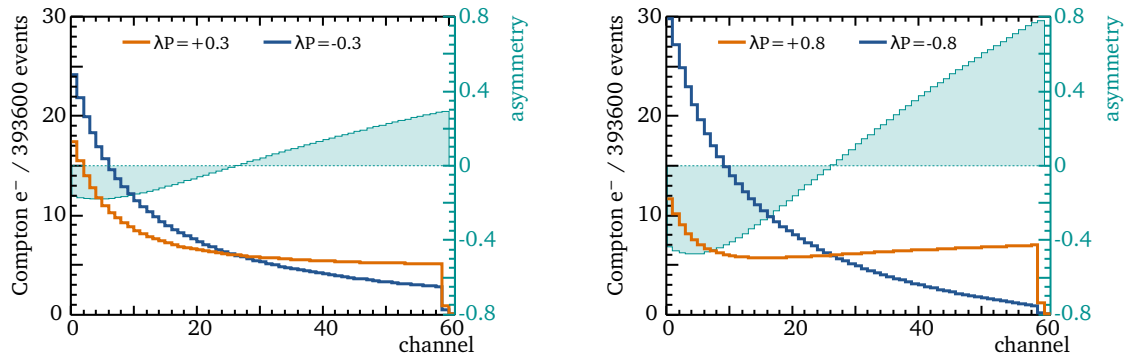

Figure 7.5: Upstream polarimeter simulation for 3 mm wide channels. The mean number of electrons per channel for both laser helicities (thick lines) and the resulting asymmetry (filled area, secondary y-axis) are shown for (a) 30 percent and (b) 80 percent polarisation after 393600 bunch crossings.

Compton electrons per channel is between 0 and 30 and thus in a range where single-peak resolution in the QDC spectra of each channel is considered feasible. The detector array placement is chosen such that Compton edge is located in channel 60, identifiable by the sharp drop-off in the number of electrons in that channel.

The polarisation can be calculated for each detector channel from its analysing power and the asymmetry between the measurements with left and right circular laser polarisation (as described in section 3.2.1). The resulting asymmetry between the measurements with both laser helicities in each channel is also depicted in figure 7.5. To combine the results from the individual channels, a weighted mean is calculated[19]. The detector channels with large absolute values of the asymmetry will have most impact on the polarisation measurement, while the set of channels near the zero crossing of the asymmetry are assigned the smallest statistical weights.

7.2.2 Performance in simulated polarisation measurements

To study the impact of the fit performance on the polarisation measurement, multiple polarisation measurements for 80 % and 30 % beam polarisation were simulated with $3.936 \cdot 10^6$ events and $3.936 \cdot 10^5$ events respectively. The QDC spectra were

simulated and fitted as described in section 7.1, for the number of Compton electrons per detector channel given by the upstream polarimeter prediction shown in figure 7.5. The photodetector non-linearity was varied in steps of 0.2 % from 0 % to 4 %.

Simulation of 80% polarisation

The polarisation determined for the individual channels for two simulated polarisation measurements with 80 % polarisation after $3.936 \cdot 10^6$ events (corresponding to 10 minutes of data taking at TDR beam parameters) can be seen in figure 7.6. The channel in which the Compton edge is located is excluded due to the low average number of Compton electrons expected in this channel. For the remaining 59 channels, the polarisation was determined from the primary Compton electrons, from the mean of the QDC spectra and from the number of Compton electrons determined from the fit of the QDC spectra. The calculation from the mean of the QDC spectra is the only option

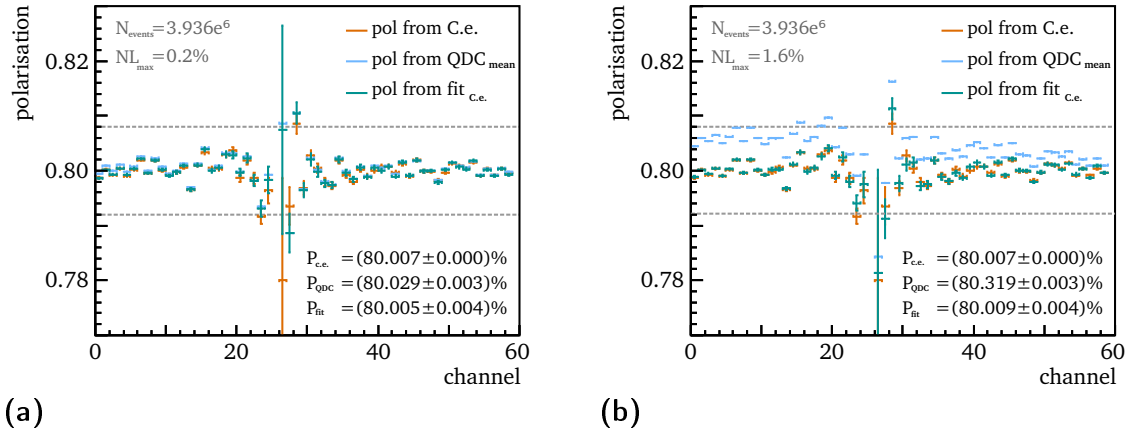

Figure 7.6: Polarisation calculated for each detector channel i for a simulation of 80 % polarisation with (a) 0.2 % and (b) 1.6 % photodetector non-linearity. The orange markers show the polarisation $\mathcal{P}_{\mathrm{C.e.,i}}$ calculated from the primary Compton electrons, the blue markers the calculation $\mathcal{P}_{\mathrm{QDC,i}}$ from the mean of the QDC spectrum, and the green markers the results $\mathcal{P}_{\mathrm{fit,i}}$ for the number of Compton electrons determined from the fit to the QDC spectra. The grey lines mark a band of ±1 % around the weighted mean $\mathcal{P}_{\mathrm{fit}}$ calculated from the individual channel polarisations from the spectrum fit.

for the gas detector concept(c.f. section 4.2.1). For a perfectly linear photodetector, it should correspond to the calculation with the primary Compton electrons, since any constant scale factor cancels out in the calculation of the asymmetries.
While the results from the three different methods exhibit no striking difference for 0.2 % photodetector non-linearity as shown in figure 7.6(a), a larger non-linearity of 1.6 % distorts the QDC mean and therefore the measured polarisation significantly (figure 7.6(b)), while the polarisation calculated from the fit results appears to be unaffected.

For photodetector non-linearities in 0.2 % steps from 0 % to 4 %, 100 different random non-linearity transfer functions were generated and used for the spectrum generation. The mean and RMS of the deviation between the polarisation determined from the mean of the generated QDC with respect to the result for the primary electron calculation is shown in figure 7.7(a). As discussed in section 4.1, the error budget for the detector linearity contribution to the polarisation measurement is 0.1 %. The method using the mean of the QDC surpasses the allocated limit for non-linearities $\gtrsim 0.4\,\%$. The results for the polarisation calculation from the fitted number of Compton electrons is shown in figure 7.7(b). Fitting the QDC spectra instead of using the mean

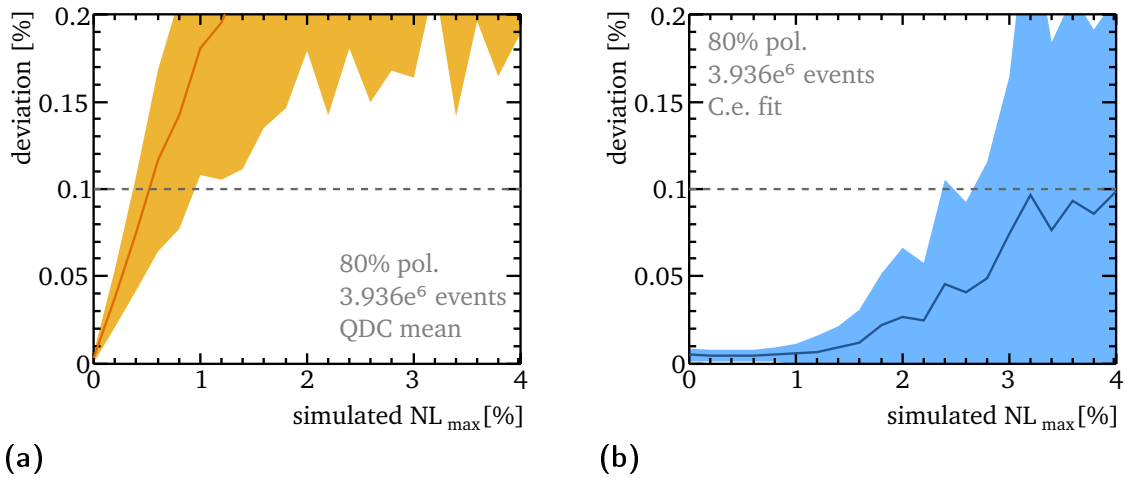

Figure 7.7: Deviation between the result from the polarisation $\mathcal{P}_{\text{C.e.}}$ calculated from the primary Compton electrons and (a) the polarisation $\mathcal{P}_{\text{QDC}}$ determined from the mean of the QDC spectrum, and (b) the polarisation $\mathcal{P}_{\text{fit}}$ calculated with the number of Compton electrons determined from the fit of the QDC spectra.

can compensate the photodetector non-linearity well enough to stay within the error budget for non-linearities up to $\sim 2.2\,\%$.

In a by-eye examination of the fitted polarisation of all individual channels, it becomes apparent that the fit result agrees well with the primary electron input for most channels, failing only in a small number of channels. To address this, a second step in the calculation of the polarisation can be introduced, where the polarisation is recalculated using only the channels which agree within $\pm 1\,\% \cdot \mathcal{P}_{\text{fit}}$ with the polarisation calculated from all channels (i.e. the channel polarisations in the area between the grey lines in figure 7.6). This eliminates the contribution from outlier channels. The fraction of channels consequently used in the calculation is shown in figure 7.8(a). Using less channels will decrease the statistical precision slightly. However, the benefits of this approach in dealing with larger detector non-linearities are clearly visible in figure 7.8(b), where the deviation between the polarisation thus obtained with respect to the result for the primary Compton electrons is shown. Even for photodetector non-linearities of 4 %, this deviation is below 0.03 %, i.e. well within the error budget of 0.1 %, which would be a contribution towards reducing the overall systematic uncertainty on the polarisation measurement.

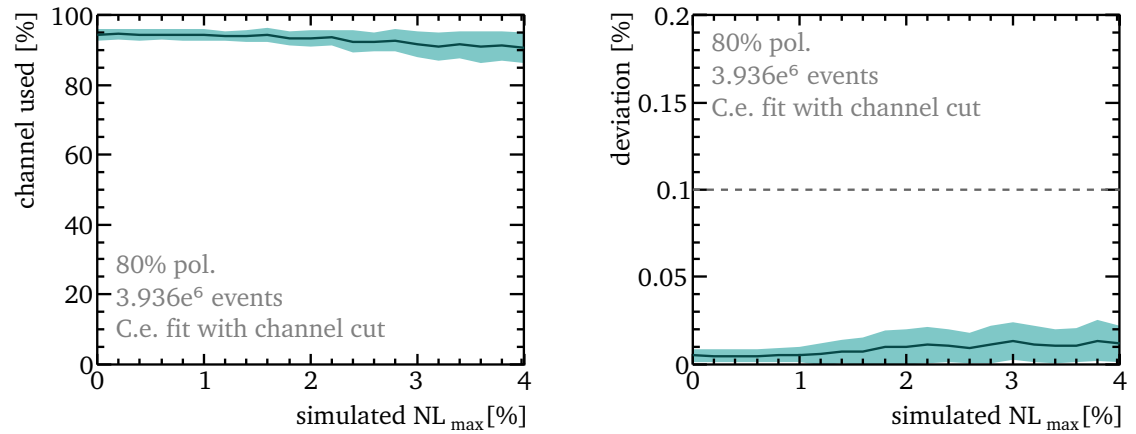

Figure 7.8: (a) Fraction of detector channels i whose polarisations $\mathcal{P}_{\text{fit,i}}$ agree within $\pm 1\,\% \cdot \mathcal{P}_{\text{fit}}$ with the polarisation calculated from all channels. (b) Deviation of the polarisation calculated from the selected channels with respect to $\mathcal{P}_{\text{C.e.}}$.

Simulation of 30% polarisation with less statistics

After the successful outcome the for test with 80 % polarisation, a more challenging scenario was studied to test the performance under extreme conditions: 30 % beam polarisation, which means smaller asymmetries between the measurements, for smaller samples with only $3.936 \cdot 10^5$ events (corresponding to 1 minute of data taking at TDR beam parameters).

The polarisation determined for the individual channels for two simulated polarisation measurements with this configuration and different non-linearities can be seen in figure 7.9. Again, in case of 0.2 % photodetector non-linearity, the QDC mean agrees well with the calculation from the primary Compton electrons, which is not the case anymore for 1.6 %. In addition, the reduced polarisation and statistics lead to larger fluctuations around the mean value, already for the channel polarisation $\mathcal{P}_{C.e.,i}$ calculated from the primary Compton electrons and consequently also for the results

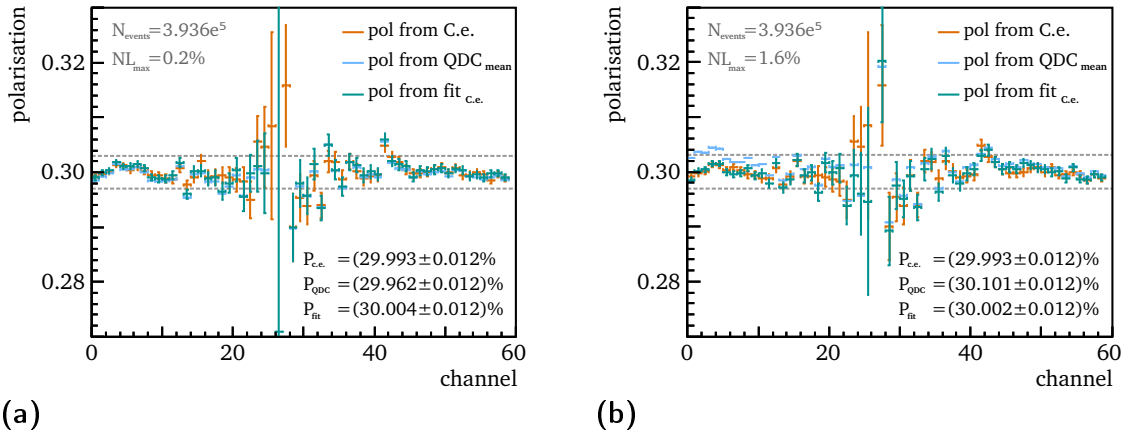

Figure 7.9: Polarisation calculated for each detector channel i for a simulation of 30 % polarisation with (a) 0.2 % and (b) 1.6 % photodetector non-linearity. The orange markers show the polarisation $\mathcal{P}_{\text{C.e.,i}}$ calculated from the primary Compton electrons, the blue markers the calculation $\mathcal{P}_{\text{QDC,i}}$ from the mean of the QDC spectrum, and the green markers the results $\mathcal{P}_{\text{fit,i}}$ for the number of Compton electrons determined from the fit to the QDC spectra. The grey lines mark a band of ±1 % around the weighted mean $\mathcal{P}_{\text{fit}}$ calculated from the individual channel polarisations from the spectrum fit.

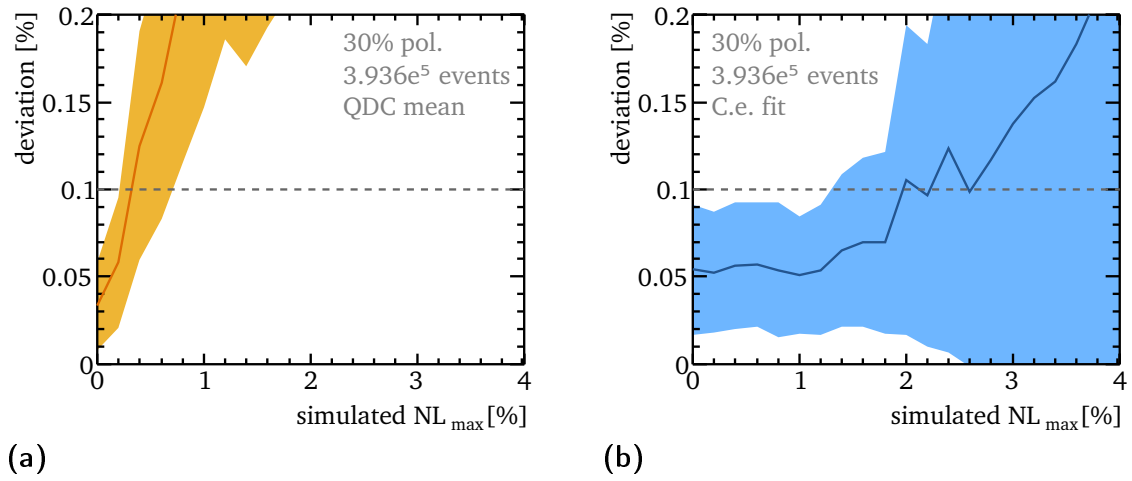

Figure 7.10: Deviation between the result from the polarisation $\mathcal{P}_{\text{C.e.}}$ calculated from the primary Compton electrons and (a) the polarisation $\mathcal{P}_{\text{QDC}}$ determined from the mean of the QDC spectrum, and (b) the polarisation $\mathcal{P}_{\text{fit}}$ calculated with the number of Compton electrons determined from the fit of the QDC spectra.

$\mathcal{P}_{QDC,i}$ from the mean of the QDC spectra and the results $\mathcal{P}_{fit,i}$ from the Compton electron fit.

Analogous to the scenario with 80 % polarisation, the impact of photodetector non-linearities from 0 % to 4 % was studied. The outcome is shown in figure 7.10. For the polarisation measurement using the mean QDC count to calculate the asymmetry in a detector channel, the deviations already exceed the error budget for non-linearities $\gtrsim 0.15\,\%$. The fit method performs somewhat better, passing the limit of 0.1 % deviation for non-linearities $\gtrsim 1.2\,\%$. For the polarisation re-calculated using only the channels which agree within $\pm 1\,\% \cdot \mathcal{P}_{\text{fit}}$ with the polarisation calculated from all channels, the deviation stays below 0.1 % for all simulated non-linearities, as shown in figure 7.11(b). This is only possible by discarding ∼20 % of the detector channels. While the deviation in the results is within the error budget, the fluctuations are quite large depending on the shape of the non-linearity function used to describe the photomultiplier gain. This is not surprising, since it was already seen in section 7.1 (c.f. figure 7.4(b)) that for $3.936 \cdot 10^5$ events the fit procedure is still statistically limited. To reduce the polarisation uncertainty, one would therefore prefer to collect larger data

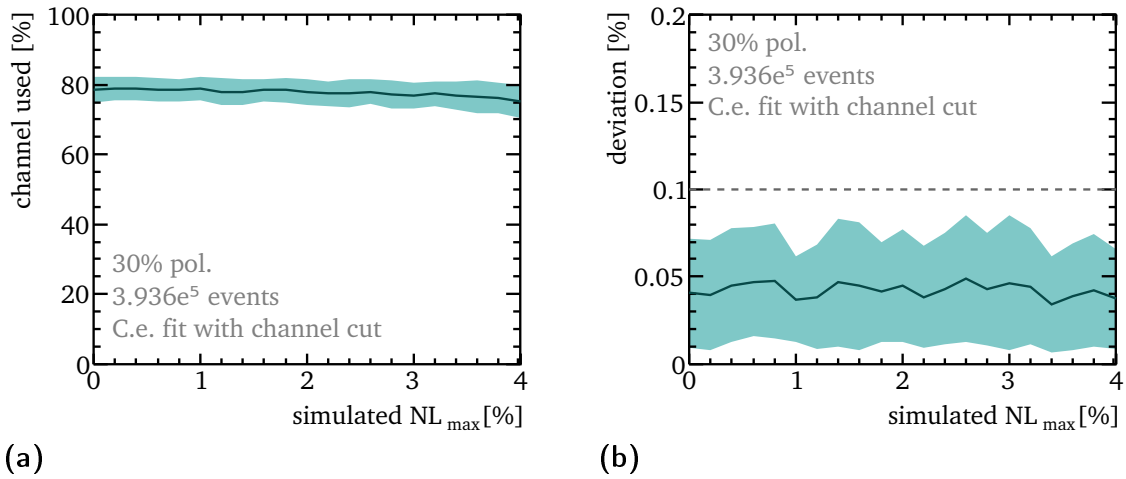

Figure 7.11: (a) Fraction of detector channels i whose polarisations $\mathcal{P}_{\text{fit,i}}$ agree within $\pm 1\,\% \cdot \mathcal{P}_{\text{fit}}$ with the polarisation calculated from all channels. (b) Deviation of the polarisation calculated from the selected channels with respect to $\mathcal{P}_{\text{C.e.}}$.

sets, over a time of several minutes, which will still allow to track the beam polarisation on shorter time scales (as explained at the end of section 7.1).

7.3 Detector alignment

For data samples collected over a time span of several minutes, the non-linearity can be well controlled by fitting the shape of the QDC spectra. Next to detector non-linearities, the detector alignment with respect to the Compton electron fan is the other large contribution to systematic uncertainties on the polarisation measurements that can be addressed by the concept for the polarimeter detectors.

Critical misalignments are any shifts in the detector position that change the analysing power. Movements in the horizontal direction change the part of the Compton fan entering a channel and therefore the integration limits for the calculation of the analysing power. Tilts of the detector setup distort the Compton spectrum on the detector front and thus also change the number of Compton electrons entering a specific channel.

As stated in section 4.1, the alignment goals for the use of the gas detector with a channel width of 10 mm at the ILC polarimeter are a precision of $\mathcal{O}(0.1\,\text{mm})$ on the horizontal position of the Compton edge, and a control of detector tilts with a precision of 1 mrad. No corresponding study has been done for other channel widths yet, but the precision required for smaller channels should be of similar size.

The goals for the horizontal alignment were already achieved for the prototype detector with table position scans in the testbeam campaign. Such table scans do however require dedicated calibration runs. To reduce the beam time spent on calibration, an online monitoring of the horizontal alignment should be considered.

Figure 7.12 shows the `LCPolMC` predictions how the mean number of Compton electrons in the detector channel at the Compton edge changes for horizontal offsets for the Compton scattering, summed over the measurements with both laser helicities, $N_L + N_R$. This sum is independent of the beam polarisation. An change in the horizontal position of 0.1 mm changes the number of Compton electrons in this channel by 1.9 electrons for the beam parameters listed in table 7.1. Monitoring the number of electrons in this channel is therefore sensitive to changes in the horizontal detector position. To take changes in the beam luminosity into account, one would not monitor

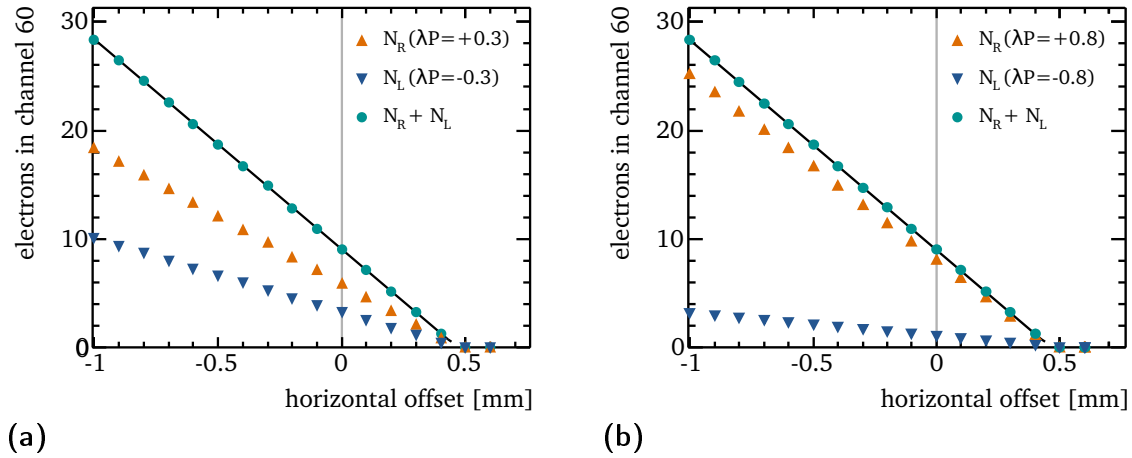

Figure 7.12: Influence of horizontal offsets in the detector position on the mean number of Compton electrons expected in the detector channel at the Compton edge for (a) 30 % and (b) 80 % polarisation, summed over the measurements with both laser helicities.

the absolute number of electrons in the last channel, but rather the fraction of electrons in that channel with respect to the sum over all channels. While changes in the mean of the QDC spectra could also occur due to changes in the photodetector gain, e.g. due to time effects in the non-linearity or ageing effects of the photodetector, fitting the shape of the QDC spectra as described in section 7.1 allows to disentangle such effects from the change in Compton electron number. A change by $\gtrsim$1 electron could be detected, which would allow to control the horizontal alignment to $\mathcal{O}(0.1\,\mathrm{mm})$.

The alignment of the quartz detector with respect to angular tilts still requires more detailed investigation. Along with the exploration of methods for angular alignment, it needs to be studies whether a setup with flipped channels under a movable angle would really be necessary at the ILC polarimeter, or if a simpler configuration with parallel channels under a fixed angle would be sufficient. Apart from this, the studies in this detector have shown that a detector concept which allows single-peak resolution, such as the quartz detector discussed in this thesis, is suitable to address contributions to the systematic uncertainty of the polarisation measurement from the detector alignment. If the results from the simulations hold up in reality, photodetector non-linearities would play no role in the systematic uncertainty of the polarisation measurement.

8

Conclusion

Polarised beams offer great benefits for precision measurements at future collider experiments, such as the International Linear Collider. To exploit the full potential of the ILC, high precision polarimetry is needed. The goal for polarimetry at the ILC is a precision of $\delta\mathcal{P}/\mathcal{P} = 0.25\,\%$, which is a factor two better than the best accuracy achieved for beam polarisation measurements up to this date. The main sources of systematic uncertainty for the polarisation measurement have been identified as uncertainties on the laser polarisation, the alignment of detectors at the polarimeters, and non-linearities in the response of the photodetectors used with the Cherenkov detectors foreseen for the planned ILC Compton polarimeters.

The focus of this thesis was the development of a novel detector concept for the ILC polarimeters using quartz as Cherenkov medium, motivated by the fact that the light yield for quartz is expected to be significantly larger than for conventional gas Cherenkov detectors. A sufficiently large number of detected photons per incident electron could allow to resolve single peaks in the measured Cherenkov light. In that case, the determination of the number of Compton electron per detector channel directly from the shape of the signal would be feasible, without the need for a separate photodetector calibration.

A suitable detector geometry for a quartz Cherenkov detector was developed in simulation studies. A prototype detector was constructed and operated in a single electron beam at the DESY testbeam. Both the light yield predicted from the simulation studies as well as the analysis of the testbeam data indicate that achieving single-peak resolution is possible.

In a subsequent evaluation of the performance of such a detector concept in the conditions at the ILC upstream polarimeter, it was found that the resolution of single Compton electron peaks in the measured Cherenkov light spectra is indeed advantageous: The systematic uncertainty of the polarisation measurement could be improved significantly by compensating non-linearities of the photomultipliers. In addition, determining the fraction of Compton electrons in the last channel with the expected precision could help to control the horizontal alignment of the Cherenkov detector array with respect to the Compton electron fan.

Some open questions remain before a decision on the technology for the polarimeters can be made. The vertical and angular alignment of the quartz detector require further investigation. This should preferably happen in a testbeam campaign with multiple electrons, to validate the expectations for the resolution of individual electron peaks from the Cherenkov light spectrum of more than one electron.

Based on the encouraging findings in this thesis, such additional studies seem worthwhile. The application of quartz Cherenkov detectors at the ILC polarimeters could be an excellent approach to deal with two of the main causes for systematic uncertainties in the polarisation measurement.

Bibliography

[1] ATLAS Collaboration, *Observation of an Excess of Events in the Search for the Standard Model Higgs boson with the ATLAS detector at the LHC*, Tech. Report ATLAS-CONF-2012-093, CERN, Geneva, Jul 2012.

[2] CMS Collaboration, *Observation of a new boson with a mass near 125 GeV*, Tech. Report CMS-PAS-HIG-12-020, CERN, Geneva, 2012.

[3] K. Abe et al., *High-Precision Measurement of the Left-Right Z Boson Cross-Section Asymmetry*, Physical Review Letters **84** (2000), 5945–5949.

[4] T. Behnke et al., *The International Linear Collider Technical Design Report - Volume 1: Executive Summary*, arXiv e-prints (2013), arXiv:1306.6327.

[5] H. Baer et al., *The International Linear Collider Technical Design Report - Volume 2: Physics*, arXiv e-prints (2013), arXiv:1306.6352.

[6] Chris Adolphsen et al., *The International Linear Collider Technical Design Report - Volume 3.I: Accelerator R&D in the Technical Design Phase*, arXiv e-prints (2013), arXiv:1306.6353.

[7] Chris Adolphsen et al., *The International Linear Collider Technical Design Report - Volume 3.II: Accelerator Baseline Design*, arXiv e-prints (2013), arXiv:1306.6328.

[8] Ties Behnke et al., *The International Linear Collider Technical Design Report - Volume 4: Detectors*, arXiv e-prints (2013), arXiv:1306.6329.

[9] Rey.Hori, *ILC / Structural view of ILD detector*, [image], 2011, available online at `http://www.linearcollider.org/images/pid/1000890/gallery/15_ILC_ILD.jpg`; accessed on July 4th 2014.

[10] Rey.Hori, *ILC / general view of SiD detector*, [image], 2012, available online at `http://www.linearcollider.org/images/pid/1000890/gallery/14_ILC_SiD.jpg`; accessed on July 4th 2014.

[11] H. Aihara, P. Burrows, and M. Oreglia, *SiD Letter of Intent*, arXiv e-prints (2009), arXiv:0911.0006.

[12] The ILD Concept Group, *The International Large Detector: Letter of Intent*, arXiv e-prints (2010), arXiv:1006.3396.

[13] G. Moortgat-Pick et al., *The role of polarized positrons and electrons in revealing fundamental interactions at the Linear Collider*, Phys.Rept. **460** (2008), 131–243.

[14] Sabine Riemann, *Physics Applications of Polarized Positrons*, Tech. Report LC-REP-2013-017, Linear Collider Note, 2013, available online at `http://www-flc.desy.de/lcnotes`.

[15] Christoph Bartels, Mikael Berggren, and Jenny List, *Characterising WIMPs at a future e^+e^- Linear Collider*, Eur.Phys.J. **C72** (2012), 2213.

[16] Yoonseok John Chae and Maxim Perelstein, *Dark matter search at a linear collider: effective operator approach*, Journal of High Energy Physics **2013** (2013), no. 5.

[17] I. Božović Jelisavčić et al., *Luminosity measurement at ILC*, Journal of Instrumentation **8** (2013), 8012P, arXiv:1304.4082.

[18] O. Klein and T. Nishina, *Über die Streuung von Strahlung durch freie Elektronen nach der neuen relativistischen Quantendynamik von Dirac*, Zeitschrift fur Physik **52** (1929), 853–868.

[19] V. Gharibyan, N. Meyners, and P. Schuler, *The TESLA Compton polarimeter*, Tech. report, Linear Collider Note, 2001, available online at `http://www-flc.desy.de/lcnotes`.

[20] S. Boogert et al., *Polarimeters and energy spectrometers for the ILC Beam Delivery System*, Journal of Instrumentation **4** (2009), 10015, arXiv:0904.0122.

[21] M. Beckmann et al., *Spin Transport and Polarimetry in the Beam Delivery System of the International Linear Collider*, Journal of Instrumentation **9** (2014), no. 07, P07003, arXiv:1405.2156.

[22] Moritz Beckmann, *Spin Transport at the International Linear Collider and its Impact on the Measurement of Polarization*, Ph.D. thesis, Universität Hamburg, 2013, DESY-THESIS-2013-053.

[23] A. Blondel, *A scheme to measure the polarization asymmetry at the z pole in LEP*, Physics Letters B **202** (1988), 145–148.

[24] Klaus Mönig, *The Use of positron polarization for precision measurements*, 2nd ECFA/DESY Study **LC-PHSM-2000-059** (2000), 1346–1352.

[25] Ivan Marchesini, *Triple gauge couplings and polarization at the ILC and leakage in a highly granular calorimeter*, Ph.D. thesis, Universität Hamburg, 2011, DESY-THESIS-2011-044.

[26] K. O. Eyser et al., *Simulation Studies and Detector Scenarios for an ILC Polarimeter*, arXiv e-prints (2007), arXiv:0709.2859.

[27] C. Bartels et al., *Design and construction of a Cherenkov detector for Compton polarimetry at the ILC*, Journal of Instrumentation **7** (2012), 1019, arXiv:1011.6314.

[28] I. E. Tamm, *General Characteristics of Vavilov-Cherenkov Radiation*, Science **131** (1960), 206–210.

[29] J. Beringer et al., *Review of Particle Physics*, Phys. Rev. D **86** (2012), 010001.

[30] E. Fokitis et al., *The fabry-perot interferometer for the DELPHI ring imaging cherenkov detector*, Nuclear Physics B - Proceedings Supplements **44** (1995), no. 1-3, 246 – 251.

[31] Christoph Bartels, *WIMP search and a Cherenkov detector prototype for ILC polarimetry*, Ph.D. thesis, Universität Hamburg, 2011, DESY-THESIS-2011-034.

[32] Benedikt Vormwald, *From Neutrino Physics to Beam Polarisation - a High Precision Story at the ILC*, Ph.D. thesis, Universität Hamburg, 2014, DESY-THESIS-2014-006.

[33] Christian Helebrant, *In search of new phenomena using polarization: HERA and ILC*, Ph.D. thesis, Universität Hamburg, 2009, DESY-THESIS-2009-049.

[34] I. H. Malitson, *Interspecimen comparison of the refractive index of fused silica*, J. Opt. Soc. Am. **55** (1965), no. 10, 1205–1208.

[35] S. Agostinelli et al., *Geant4 - a simulation toolkit*, Nuclear Instruments and Methods in Physics Research Section A: Accelerators, Spectrometers, Detectors and Associated Equipment **506** (2003), no. 3, 250 – 303.

[36] J. Allison et al., *Geant4 developments and applications*, IEEE Transactions on Nuclear Science **53** (2006), 270–278.

[37] Heraeus Quarzglas GmbH & Co. KG, *Quartz glass for optics: Data and properties*, datasheet, 2013, available online at `http://optik.heraeus-quarzglas.de/media/webmedia_local/downloads/FusedsilicaandQuartzGlassforOpticsDataandProperties.pdf`; accessed on March 12th 2014.

[38] Cargille Laboratories Inc., *Fused silica matchng liquid code 06350*, datasheet, 2002, available online at `http://www.cargille.com/FS06350.pdf`; accessed on March 31st 2014.

[39] Cargille Laboratories Inc., *Fused silica matchng liquid code 50350*, datasheet, 2002, available online at `http://www.cargille.com/FS50350.pdf`; accessed on March 31st 2014.

[40] A. Levin and C. Moisan, *A more physical approach to model the surface treatment of scintillation counters and its implementation into detect*, Tech. report, in 1996 IEEE Nuclear Science Symp. Conf. Rec, 1996.

[41] Hamamatsu Photonics K.K., *Multianode photomultiolier tube R7600U-M4 series*, datasheet, 2010, available online at `http://www.hamamatsu.com/resources/pdf/etd/R7600U-M4_TPMH1318E02.pdf`; accessed on March 17th 2014.

[42] M. Janecek and William W. Moses, *Simulating scintillator light collection using measured optical reflectance*, Nuclear Science, IEEE Transactions on **57** (2010), no. 3, 964–970.

[43] Hamamatsu Photonics K.K., *Linear array multianode PMT assembly and module*, datasheet, 2011, available online at `http://www.hamamatsu.com/resources/pdf/etd/LINEAR_PMT_TPMH1325E01.pdf`; accessed on March 17th 2014.

[44] J. Cohen-Tanugi et al., *Optical properties of the DIRC fused silica Cherenkov radiator*, Nuclear Instruments and Methods in Physics Research A **515** (2003), 680–700.

[45] Heraeus Quarzglas GmbH & Co. KG, *Spectrosil®*, datasheet, 2013, available online at `http://optik.heraeus-quarzglas.de/media/webmedia_local/downloads/Spectrosilsyntheticfusedsilica.pdf`; accessed on March 12th 2014.

[46] Ulrich Velte, *Aufbau eines Teststandes für Photodetektoren und Teststrahlmessungen für die Strahlpolarisationsmessung am ILC*, Diplomarbeit (Master's Thesis), Leibniz Universität Hannover, Germany, January 2008.

[47] R. Brun and F. Rademakers, *ROOT - An object oriented data analysis framework*, Nuclear Instruments and Methods in Physics Research A **389** (1997), 81–86.

[48] Ties Behnke et al., *Test beams at DESY*, Tech. report, EUDET-Memo, 2007-11, available online at `http://www.eudet.org/e26/`. See also `http://testbeam.desy.de`.

[49] Ingrid-Maria Gregor, *EUDET pixel telescope copies*, Tech. report, EUDET-Memo, 2010-33, available online at `http://www.eudet.org/e26/`.

[50] David Cussans, *Description of the JRA1 Trigger Logic Unit (TLU), v0.2c*, Tech. report, EUDET-Memo, 2009-09, available online at `http://www.eudet.org/e26/`.

[51] A Gherardi et al., *Preliminary analysis of the R7600-03-M64 MAPMT response to the nitrogen UV emission wavelength*, Dff 402/5/03, Universita degli Studi di Firenze (XUVLab), 2003.

[52] Silvano Donati, *Photomultipliers*, Wiley Encyclopedia of Biomedical Engineering (M.Akay, ed.), John Wiley & Sons, Inc., 2006, DOI: 10.1002/9780471740360.ebs0924.

[53] Hamamatsu Photonics K.K., Editorial Committee, *PHOTOMULTIPLIER TUBES-Basics and Applications*, 3 ed., Hamamatsu Photonics K.K., Electron Tube Division, 2007, available online at `https://www.hamamatsu.com/resources/pdf/etd/PMT_handbook_v3aE.pdf`.

[54] Matteo Frigo, *A Fast Fourier Transform Compiler*, Proceedings of the ACM SIGPLAN 1999 Conference on Programming Language Design and Implementation (New York, NY, USA), PLDI '99, ACM, 1999, pp. 169–180.

Acknowledgements

I would like to conclude by thanking all the people who made this thesis possible.

Above all, I want to thank Dr. Jenny List for giving me the opportunity to do my PhD in the polarimetry group. The chance to work on a project involving all steps from the first design studies over construction and testbeam operation to an analysis of the testbeam data was something I really enjoyed. I learned a lot along the way, and I'm much obliged for many interesting discussions and valuable suggestions, and for all the support and advice during the last three and a half years.

I also thank Prof. Dr. Erika Garutti and Prof. Dr. Peter Schleper for agreeing to examine my work and act as referees.

The construction of "my" detector would not have been possible without Bernd Beyer, who patiently went through many iterations me until we had a suitable mechanical setup, Dörte David, who designed the power supply circuit for the stepping motor, and Volker Prahl, who organised all the odds and ends in the prototype construction.
I also owe thanks everyone who volunteered to help during the testbeam, especially Benedikt Vormwald, who stayed way past midnight until we got everything running, and Madalina Chera, who kept me company during many late shifts.

A lot of polarimetry-related questions were answered in helpful discussions with Daniela Käfer, Moritz Beckmann and Benedikt Vormwald.

In addition, I would like to thank my colleagues from the entire FLC group. I won't go into detail and mention everyone by name, but I think I owe you all a cake for the friendly work environment as much as for all the nice coffee breaks!

Ralf Diener and Klaus Zenker valiantly endured all my random questions and my design obsession during the years we shared an office. I'm grateful to them as well as to Felix Müller for all the times they made me laugh.

Besides, I would like to thank Claude Dürig and Hale Sert for the fun times we spent together during conference trips, Andrea Schrader for always having an open door when I had an organisational question or wanted to have a nice chat, and Madalina Chera for all of the above.

Finally, a very special thank you goes to my family, who were always there for me - not only during the time I was writing this thesis, but throughout my entire life.